9-2021

Improved Out-of-Plane BRDF Measurement and Modeling

Todd V. Small

IMPROVED OUT-OF-PLANE MEASUREMENT AND MODELING FOR BIDIRECTIONAL REFLECTANCE DISTRIBUTION FUNCTIONS

DISSERTATION

Todd V. Small, Maj, USAF

AFIT-ENP-DS-21-S-035

DEPARTMENT OF THE AIR FORCE
AIR UNIVERSITY

AIR FORCE INSTITUTE OF TECHNOLOGY

Wright-Patterson Air Force Base, Ohio

AFIT-ENP-DS-21-S-035

IMPROVED OUT-OF-PLANE MEASUREMENT AND MODELING FOR BIDIRECTIONAL REFLECTANCE DISTRIBUTION FUNCTIONS

DISSERTATION

Presented to the Faculty

Graduate School of Engineering and Management

Air Force Institute of Technology

Air University

Air Education and Training Command

in Partial Fulfillment of the Requirements for the

Degree of Doctor of Philosophy

Todd V. Small, BS, MS

Maj, USAF

September 2021

AFIT-ENP-DS-21-S-035

IMPROVED OUT-OF-PLANE MEASUREMENT AND MODELING FOR BIDIRECTIONAL REFLECTANCE DISTRIBUTION FUNCTIONS

DISSERTATION

Todd V. Small, BS, MS
Maj, USAF

Committee Membership:

Lt Col Samuel D. Butler, PhD
Chairman

Michael A. Marciniak, PhD
Member

Richard G. Cobb, PhD
Member

ADEDEJI B. BADIRU, PhD
Dean, Graduate School of Engineering and Management

Abstract

The bi-directional reflectance distribution function (BRDF) describes the directional (or spatial) nature of light's reflectance from a material surface. When incident light of a particular wavelength strikes a material surface from a particular direction, portions of that incident light are reflected into various directions in various amounts, depending on the material's surface characteristics. Historically, the vast majority of BRDF measurement and modeling research has focused on reflection within the plane-of-incidence (in-plane) and dealt primarily with simplified isotropic BRDFs. Remote sensing applications, such as satellite light curve analysis, still struggle with disagreements between observations and simulations, but typically rely on closed-form simplified models for efficiency. This work is motivated by the hypothesis that unmeasured and unmodeled reflection outside the plane-of-incidence (out-of-plane) may account for part of such disagreements. A novel system is designed and constructed to successfully measure out-of-plane material BRDFs near the specular peak with high angular resolution. The system is then used to measure several materials, including a commercially available satellite solar cell. The measurements identify several previously unmodeled out-of-plane BRDF components, including a significant diffraction pattern and an offset specular peak. Finally, the measurements are used to inform the creation of a novel closed-form BRDF model for the solar cell which accurately replicates the material's out-of-plane reflection behavior – including the offset peak and diffraction pattern – using traditional BRDF inputs. Ultimately, it is expected that this and other out-of-plane BRDF models may improve the accuracy of light curve analysis and other remote sensing applications.

To my wife and kids,

thank you for joining me on this journey,

and to my parents,

thank you for fostering my childhood curiosity.

Acknowledgements

I am truly grateful for the mentorship I received from my research advisor, Lt Col Samuel Butler. His scholarship, thoughtfulness, and enthusiasm were indispensible to me throughout the entire project. I particularly appreciated his patience during several difficult times, especially within the past year and a half. I would also like to thank my other committee members, Dr. Michael Marciniak and Dr. Richard Cobb, for diligently sharing their insights, expertise, and connections with me. I would also like to thank Mr. Matthew Miller for helping me first learn how to use the CASI® equipment, and Mr. Greg Smith for sharing his laboratory expertise and assistance many times. Finally, I would like to thank Dr. Michael Yakes at the Air Force Office of Scientific Research for funding this research.

Todd V. Small

Table of Contents

Page

Page

Page

List of Figures

List of Tables

List of Abbreviations

Abbreviation		Page
BRDF	bi-directional reflectance distribution function	1
SDA	space domain awareness	3
CASI®	Complete Angle Scatter Instrument	5
CCD	charge-coupled device	5
DHR	directional-hemispherical reflectance	27
HDR	hemispherical-directional reflectance	28
NEFDS	Nonconventional Exploitation Factors Data System	36
NIST	National Institute of Science and Technology	36
GTR	Generalized-Trowbridge-Reitz	37
AFIT	Air Force Institute of Technology	43
USAF	United States Air Force	47
USSF	United States Space Force	47
AFSPC	Air Force Space Command	48
DoD	Department of Defense	49
FPA	focal plane array	59
SNR	signal-to-noise ratio	59
DRR	dual rotating retarder	60
ND	neutral density	63
OD	optical density	66
sDC	scaled digital counts	86

IMPROVED OUT-OF-PLANE MEASUREMENT AND MODELING FOR BIDIRECTIONAL REFLECTANCE DISTRIBUTION FUNCTIONS

I. Introduction

1.1 Research Motivation

Even today, 56 years after the first formal definition of the bi-directional reflectance distribution function (BRDF) [50], many aspects of BRDF measurement and modeling maintain open areas of research. Fundamentally, a BRDF simply describes the directional (or spatial) nature of light's reflectance from a material surface. When incident light of a particular wavelength strikes a material surface from a particular direction, portions of that incident light are reflected into various directions in various amounts, depending on the material's surface characteristics. For instance, the distribution of light reflected from a very smooth (specular) surface tends to cluster very closely near the outbound direction defined by the well-known law of reflection, while the distribution of light reflected from a rough (diffuse) surface tends to spread out much more evenly across all possible outbound directions. Of course, increased surface complexity can lead to increased BRDF complexity.

Models of BRDFs are commonly used in remote sensing applications to predict or interpret observations comprised of light reflected from material surfaces. As one can imagine, it can be far from trivial to physically model the full array of atomic-level interactions between an incident electromagnetic wave and a particular material in order to calculate exactly how and where the incoming wave will reflect. Deriving detailed knowledge of a material's surface composition and then solving Maxwell's

Equations can quickly become too computationally unwieldy for many complex surfaces and applications. Oftentimes instead, material BRDFs are measured directly, and then simplified mathematical models – which can be more easily ingested into computational routines – are used to fit the measurements.

Due to a desire for both computational efficiency and radiometric accuracy, remote sensing applications commonly rely on closed-form microfacet BRDF models [23, 60, 48, 58, 76, 28, 18]. At their core, microfacet models describe material surfaces as comprised of many very small specular microfacets with some distribution of orientations relative to the overall surface normal [70]. However, the simplifying assumptions inherent within the microfacet construct tend to ignore certain physical characteristics and phenomena.

For one, the vast majority of BRDF measurement and modeling research deals primarily with simplified isotropic BRDFs by sampling within the plane of incidence (in-plane) and assuming that a material's surface features are identical in every direction across its surface [26, 47]. On the other hand, anisotropic BRDF measurement and modeling techniques allow for material surface characteristics to vary in different directions. For some materials, the isotropic assumption is likely a valid approximation, but for others it is certainly not, and so isotropic models are typically unable to describe reflection from materials with more complex or anisotropic surface characteristics, including reflection outside the plane-of-incidence (out-of-plane). Existing anisotropic measurement sampling techniques unfortunately often sacrifice spatial resolution, particularly near specular peaks [26, 75, 22], where anisotropic reflectance properties may in fact be most pronounced.

Conventional microfacet model formulations also assume geometric optics, which inherently ignores the wave nature of light. Certain phenomena such as diffraction are rooted in the wave nature of light, but BRDF models which include wave optics, such

as the Modified Beckmann-Kirchhoff [36] or Generalized Harvey-Shack [35, 44] models, are much more computationally intensive and often do not possess closed-form general solutions. As a result, the models common to remote sensing applications are typically unable to describe more complex wavelength-dependent reflection characteristics.

Light curve analysis represents one important remote sensing application within the space domain awareness (SDA) mission set which relies heavily upon material BRDFs to assist in characterizing spacecraft in orbit. Satellite observations in the visible regime are predominantly comprised of reflected light, and for those in high Earth orbits, such as the geosynchronous belt, optical collections are almost exclusively spatially unresolved due to the vast distances between target and observer [15]. In order to correctly predict and interpret light curve observations, though, reflection from satellites must first be understood and modeled with sufficient accuracy, which depends in part upon accurate material BRDF knowledge and modeling.

Unfortunately to date, disagreement often still exists between light curve observations and simulations, specifically in regards to reproducing specular glints, and imperfect material BRDFs remain a well-documented and plausible contributing factor to radiometric prediction inaccuracies [16, 20, 46]. For example, many satellites utilize solar cells, often with large surface areas relative to the satellite's size. Despite complex surface structures involving coverglass, metal conducting bars, and photovoltaic layers, radiometric simulations traditionally incorporate isotropic solar cell BRDFs, which at best include an individual specular term with a general diffuse term [74, 5, 16, 20, 42, 46], but sometimes simply assume purely diffuse (Lambertian) reflectance [17, 39]. In either case, no known solar cell BRDF models are able to incorporate out-of-plane or wavelength-dependent reflectance features.

1.2 Research Objective

In terms of general BRDF research, a current gap exists in the capability to measure out-of-plane BRDF data with high angular resolution, particularly surrounding the specular peaks of materials. The lack of this capability has meant there is a gap in identifying and quantifying the out-of-plane BRDF behavior of materials, particularly those with anisotropic surface features likely to cause significant out-of-plane behavior. In turn, the lack of out-of-plane BRDF measurement data has led to a subsequent gap in BRDF models capable of accounting for out-of-plane behavior. Ultimately, in the face of disagreements between measurement and simulation in remote sensing applications, such as those within light curve analysis, the impacts of including rather than omitting out-of-plane BRDF characteristics are largely unknown and unexplored.

The primary aim of this research is to fill in these BRDF measurement and modeling gaps systemically, with hopes of later leading to improvements in the accuracy of remote sensing analysis, in particular the disparity between satellite light curve observations and simulations. The first objective pertains to out-of-plane BRDF measurement. The goal is to design, construct, and validate a device capable of making out-of-plane specular BRDF measurements with high angular resolution. Once complete, the device can be implemented to collect out-of-plane BRDF measurements for several materials, beginning with an isotropic baseline and then proceeding to several materials with anisotropic surface characteristics pertinent to reflection from satellites. The second objective pertains to out-of-plane BRDF modeling. The goal is to use the new device's out-of-plane measurement data to identify significant out-of-plane behavior from at least one satellite material, and then use the data to inform an updated closed-form BRDF model. As will be shown in Section 5.4, a commercially available solar cell produced very significant out-of-plane behavior, and since solar

cells are also particularly relevant for satellite light curve analysis, focus was placed on producing an updated solar cell model specifically.

1.3 Research Hypothesis

The disparity between observed and simulated light curve glints may be improved by identifying satellite materials with substantial out-of-plane reflectance contributions, and then subsequently updating those material BRDF models to better match specular out-of-plane measurements.

Research Questions.

Answering the following questions will provide evidence to support the hypothesis above.

1. Can a device be built which measures both in-plane and out-of-plane material BRDF measurement data with high angular resolution surrounding the specular peak?

2. Can significant out-of-plane material BRDF attributes be identified and quantified?

3. Can the common microfacet BRDF model formulation be extended to account for previously unmodeled out-of-plane behavior?

Research Methodology.

To answer the first research question, the industry-standard Complete Angle Scatter Instrument (CASI®) is augmented with a charge-coupled device (CCD) array detector, creating a novel system capable of simultaneously measuring several degrees of both in-plane and out-of-plane BRDF data surrounding the specular peak. By

mounting a CCD onto the CASI® detector arm along with an appropriate alignment apparatus, the system shares the CASI®'s high-precision motion stages and laser source conditioning. Now, however, instead of using a single-pixel detector to measure one in-plane scatter direction at a time, each of the over eight million CCD pixels maps to a unique scatter direction simultaneously. Although the augmented system sacrifices dynamic range, it improves angular resolution, and a robust uncertainty analysis shows comparable uncertainty levels to the original system.

To answer the second question, three materials were chosen based on relevance to satellite reflectance and likelihood of exhibiting out-of-plane reflectance behavior. First, a mirror was used as an isotropic baseline, followed by circularly polished aluminum, unwrinkled Kapton®, and a commercially available solar cell. All three demonstrated noticeable out-of-plane asymmetry, but as expected with its complex surface structure, the solar cell easily demonstrated the most compelling behavior, which included a primary specular peak, a second specular peak offset from the first, and a sizeable diffraction pattern in one direction.

The common microfacet model is truly only suited to model the primary specular peak, and so to answer the third question, new terms were devised and formulated to account for both the offset specular peak and the diffraction pattern. In particular, Fourier theory was used to express the diffraction pattern in closed form, but modifications were required to write the inputs in terms of incident and scatter angles. Of course, the diffraction term includes a wavelength dependence as well.

The work toward answering these questions led to two primary novel contributions:

1. A novel BRDF measurement system capable of simultaneous in-plane and out-of-plane collection with high angular resolution, validated by the CASI® detector.

2. A novel solar cell BRDF model which matches each of the measured but previ-

ously unmodeled out-of-plane features.

Next important steps – unfortunately beyond the scope of this work – involve incorporating the updated solar cell BRDF model into appropriate radiometric simulations in an effort to determine its potential impact on light curve generation and interpretation, ideally compared to real-world observational data.

Assumptions and Limitations.

The primary limitation of this work is related to scope. This work presents BRDF measurement results for only one sample of each material from one snapshot in time within a laboratory setting. Thus, the results do not necessarily extend to other samples unless the surface characteristics remain similar enough. For example, aluminum finishes can certainly vary from sample to sample, solar cells can be manufactured differently, and Kapton® often wrinkles in space. Such variations would only compound with other temporal effects such as space weathering which can affect any exposed surface.

Another important limitation for this work is also true of any BRDF measurement system which employs laser sources. Due to their highly directional uniformity and small focused beamwidths, laser sources allow for very precise angular BRDF measurements, but conversely only illuminate relatively small portions of a material surface at a time. Thus, any individual BRDF measurement is really only valid for the illuminated portion of the material surface, unless the surface characteristics are known to be consistent elsewhere. If material characteristics do vary outside the illuminated spot, this fact must be accounted for, or some type of sample rastering or surface averaging process must be included. For the most part, this work presents results from individual illumination spots on a material sample, but does discuss potential impacts of this limitation along with the appropriate results in Chapter V.

It is also important to note that the measurements in this work were all conducted at a specific wavelength (632.8 nm), and so the updated solar cell BRDF model is not yet validated at other wavelengths. Specific polarization states were also ignored.

This work presents measurements with the CCD detector centered on the specular direction, and thus focuses on materials with distinctly noticeable specular peaks. Theoretically, by slewing the CASI® detector arm away from the specular direction, the CCD detector can be used to capture more diffuse reflection data. However, such measurements would require additional dynamic range and spatial stitching considerations, which are left to future work.

Finally, despite presenting a novel BRDF measurement system, specifically measuring a satellite solar cell, and then creating a novel solar cell BRDF model, this model has not yet been incorporated into radiometric simulations to determine its actual impact on light curve analysis. This task is left for future work.

Expected Outcomes and Impacts.

In general, the CCD-augmented CASI® represents a novel system which could be replicated by others to measure specular out-of-plane BRDF data for various materials. Every component, even the CASI® backbone itself, is commercially available. Although the device is used to measure a handful of specific materials for this work, in reality the material applications are essentially endless. Additionally, although light curve analysis provides the motivation for specifically measuring the solar cell's BRDF and updating its particular model using out-of-plane data, many other remote sensing applications could follow the same basic premise to use out-of-plane data with high angular resolution to inform improved models. Even beyond remote sensing, the scene generation and computer graphics communities also heavily utilize BRDFs.

Specifically, it is hoped that the closed-form updated solar cell BRDF model de-

veloped in this work can be successfully incorporated into light curve analysis tools to investigate potential impacts. In particular, due to the relatively wide angular extent of the solar cell's reflected diffraction pattern, it is very plausible that including the updated model will lead simulations to predict more glinting features than before. Hopefully, the updated simulations provide better agreement with observed light curves.

1.4 Document Organization

This document is organized into six chapters and one appendix. Chapter II presents pertinent background discussions of the BRDF, measurement and modeling techniques, and its application within SDA. Chapter III presents the design, setup, calibration, and alignment processes for augmenting the CASI® with a CCD detector to create a new out-of-plane BRDF measurement system. It includes a description of how to convert raw pixel readings and locations into BRDF values and scatter coordinates. Chapter IV walks through a robust uncertainty analysis for the new system, built upon the CASI®'s original uncertainty analysis, but with significant extensions to account for updated system attributes and BRDF calculation requirements. Chapter V consolidates measurement results for each of the four material samples (mirror, polished aluminum, Kapton®, and solar cell). In particular, the solar cell measurements reveal two distinct out-of-plane features which have not been included in previous models. Chapter VI utilizes the solar cell BRDF measurement data to inform the creation of a new solar cell model which includes the observed out-of-plane behavior. Chapter VII provides a conclusion to the work, and relates the results to the research questions posed here in Chapter I. Appendix A contains additional measurements of the mirror, polished aluminum, and Kapton® samples, omitted from Chapter V for conciseness.

II. Background

This chapter presents a review of the theory behind the BRDF, beginning with electromagnetic theory as the fundamental building block for describing the reflection of light.

2.1 Electromagnetism

Maxwell's Equations provide the governing authority for describing light as the propagation of electromagnetic waves through any medium, including light's interaction with any surface or boundary between media. The equations which specify the electric and magnetic fields can be written in terms of free charge density ρ_f and free current density $\vec{\mathbf{J}}_f$ in SI units as [37]

$$\nabla \cdot \vec{\mathbf{D}} = \rho_f \tag{1a}$$

$$\nabla \cdot \vec{\mathbf{B}} = 0 \tag{1b}$$

$$\nabla \times \vec{\mathbf{E}} = -\frac{\partial \vec{\mathbf{B}}}{\partial t} \tag{1c}$$

$$\nabla \times \vec{\mathbf{H}} = \vec{\mathbf{J}}_f + \frac{\partial \vec{\mathbf{D}}}{\partial t} \tag{1d}$$

by incorporating the macroscopic auxiliary fields $\vec{\mathbf{D}}$ and $\vec{\mathbf{H}}$ in addition to the microscopic electric and magnetic fields $\vec{\mathbf{E}}$ and $\vec{\mathbf{B}}$ [31]. In general, the macroscopic field are linked to the microscopic fields according to material polarization $\vec{\mathbf{P}}$ and magnetization $\vec{\mathbf{M}}$ through

$$\vec{\mathbf{D}} \equiv \epsilon_0 \vec{\mathbf{E}} + \vec{\mathbf{P}} \qquad\qquad \vec{\mathbf{H}} \equiv \frac{1}{\mu_0}\vec{\mathbf{B}} - \vec{\mathbf{M}} \tag{2}$$

where ϵ_0 and μ_0 represent the permittivity and permeability of free space, respectively [31]. For many materials, polarization and magnetization scale linearly to typical field strengths, and so the constitutive relationships

$$\vec{\mathbf{D}} = \epsilon\vec{\mathbf{E}} \qquad\qquad \vec{\mathbf{H}} = \frac{1}{\mu}\vec{\mathbf{B}} \tag{3}$$

hold for large classes of linear media. The parameters ϵ and μ, which represent material permittivity and permeability, respectively, are scalar values for isotropic materials in which electromagnetic propagation does not depend on the propagation direction through the material [31]. For conducting materials with free electrons, Ohm's law is the experimentally derived relation which describes internal current due to an electric field as

$$\vec{\mathbf{J}}_f = \sigma\vec{\mathbf{E}}, \tag{4}$$

where σ denotes material conductance [38].

After some mathematical manipulations, namely by taking the curl of both sides of Equations (1c) and (1d), utilizing the vector identity

$$\nabla \times \left(\nabla \times \vec{\mathbf{X}}\right) = \nabla\left(\nabla \cdot \vec{\mathbf{X}}\right) - \nabla^2\vec{\mathbf{X}}, \tag{5}$$

and substituting in Equations (1a), (1b), (3) and (4), Maxwell's Equations can be reduced to a single differential equation each for the electric and magnetic field vectors. For the electric field, the differential equation can be presented generally as

$$\nabla^2\vec{\mathbf{E}} - \mu\epsilon\frac{\partial^2\vec{\mathbf{E}}}{\partial t^2} - \mu\sigma\frac{\partial\vec{\mathbf{E}}}{\partial t} = 0. \tag{6}$$

The differential equation for the magnetic field appears with equivalent form. Maxwell's Equations can also be directly manipulated to form Poynting's Theorem, which when

recognized as an expression of local electromagnetic energy conservation, shows that electromagnetic waves transport energy through the Poynting vector

$$\vec{\mathbf{S}} = \vec{\mathbf{E}} \times \vec{\mathbf{H}}, \tag{7}$$

whose direction is always perpendicular to the already mutually perpendicular electric and magnetic fields. The Poynting vector represents energy flow per unit time per unit area, or energy flux density, which matches the radiometric definition of irradiance. In the optical region, electromagnetic wave frequencies are typically much faster than detector integration times, and so irradiance can be practically defined as the time average of the Poynting vector, which relates to the electric field strength through

$$\langle \vec{\mathbf{S}} \rangle_t = \frac{1}{2}\sqrt{\frac{\epsilon}{\mu}}|E_0|^2, \tag{8}$$

where $|E_0|^2$ is the squared magnitude or modulus of the electric field amplitude, which itself can be a complex quantity [6].

Non-Conducting Materials.

First, when considering the simplified case of a non-conducting material – still limited to the linear constitutive relations – the electric field differential equation reduces to the Helmholtz wave equation

$$\nabla^2 \vec{\mathbf{E}} - \mu\epsilon \frac{\partial^2 \vec{\mathbf{E}}}{\partial t^2} = 0. \tag{9}$$

Sinusoidal plane waves can be assumed as the basis for physical solutions, bearing the form

$$\vec{\mathbf{E}}\left(\vec{\mathbf{r}}, t\right) = \vec{\mathbf{E}}_0 e^{i\left(\vec{\mathbf{k}}\cdot\vec{\mathbf{r}} - \omega t\right)} = \vec{\mathbf{E}}_0 e^{i(k\zeta - \omega t)}. \tag{10}$$

Here, $\vec{\mathbf{k}}$ represents the electromagnetic wave propagation vector, where k is its magnitude and ζ advances specifically in its direction, ω is the wave's frequency, and $\vec{\mathbf{E}}_0$ is the associated electric field amplitude. Due to the linearity of the Helmholtz wave equation, more general solutions can be obtained through Fourier synthesis as the superposition of plane waves with various frequencies [37]. However, for a given frequency, substituting the solution form – Equation (10) – back into the Helmholtz equation – Equation (9) – shows that the dispersion relation

$$k = \omega\sqrt{\mu\epsilon} \tag{11}$$

must hold for light propagating through linear non-conducting media, where k is the magnitude of the propagation vector. Due to the general format of a wave equation, the speed of the wave – or more specifically phase velocity – can be extracted from Equation (9) as

$$v = \frac{1}{\sqrt{\mu\epsilon}}. \tag{12}$$

The speed of light in vacuum is known and given as

$$c = \frac{1}{\sqrt{\mu_0\epsilon_0}}, \tag{13}$$

so index of refraction can be defined as the speed of light through a material compared to the speed of light in vacuum by

$$n \equiv \frac{c}{v} = \sqrt{\frac{\mu\epsilon}{\mu_0\epsilon_0}}, \tag{14}$$

which can also be related back to the wave propagation number by

$$n = \frac{kc}{\omega}. \tag{15}$$

Index of refraction is clearly an inherent material property, and it should be noted that this property does vary as a function of frequency through the process known as dispersion, which is based on atomic-level oscillation and polarization effects.

Conducting Materials.

Next consider the more general case of a conducting material, which requires returning to Equation (6). When sinusoidal plane waves are again assumed as the basis for physical solutions, the dispersion relation for the propagation wave number updates to

$$\tilde{k}^2 = \mu\epsilon\omega^2 + i\mu\sigma\omega, \tag{16}$$

where now a third term containing σ must be included. The tilde atop $\tilde{k}$ simply denotes that the wave propagation number now contains a complex part in addition to the real part, which can be written generally as

$$\tilde{k} = \alpha + i\beta \tag{17a}$$

$$\tilde{k}^2 = \left(\alpha^2 - \beta^2\right) + 2i\alpha\beta. \tag{17b}$$

The spatial portion of the originally assumed plane wave solutions now updates to

$$\vec{\mathbf{E}}_0 e^{i\left(\tilde{k}\zeta - \omega t\right)} = \vec{\mathbf{E}}_0 e^{-\beta\zeta} e^{i(\alpha\zeta - \omega t)} \tag{18}$$

where the complex portion of the wave propagation number imparts an exponentially decaying attenuation term in the direction of spatial propagation. The real and imaginary wave propagation number components α and β can be solved in terms of μ, ϵ, ω, and σ by relating Equations (16) and (17b). The complex index of refraction still relates to wave propagation number through Equation (15), so it now has real

and imaginary components as well, written as

$$\begin{aligned} \tilde{n} &= n + i\kappa \\ &= \frac{\tilde{k}c}{\omega} \\ &= \frac{\alpha c}{\omega} + i\frac{\beta c}{\omega}. \end{aligned} \tag{19}$$

When solved explicitly in terms of μ, ϵ, ω, and σ, the real and imaginary index of refraction components are [6]

$$\begin{pmatrix} n \\ \kappa \end{pmatrix} = \begin{pmatrix} \left(\frac{\mu\epsilon}{\mu_0\epsilon_0}\right)^{\frac{1}{2}} \left[\frac{1}{2}\sqrt{1+\left(\frac{\sigma}{\epsilon\omega}\right)^2} + \frac{1}{2}\right]^{\frac{1}{2}} \\ \left(\frac{\mu\epsilon}{\mu_0\epsilon_0}\right)^{\frac{1}{2}} \left[\frac{1}{2}\sqrt{1+\left(\frac{\sigma}{\epsilon\omega}\right)^2} - \frac{1}{2}\right]^{\frac{1}{2}} \end{pmatrix}. \tag{20}$$

This complex format for index of refraction can be used more generally in subsequent analysis to encapsulate both non-conducting and conducting linear materials, based upon whether κ is zero or non-zero, respectively. As before, the complex index of refraction still depends upon the frequency of the electromagnetic wave through dispersion.

Polarization & Fresnel Reflectance.

When Gauss's Law and Stoke's Theorem are applied to an interface of infinite extent between two materials, boundary conditions can be established for the electric

and magnetic fields at that interface, written

$$\left(\vec{\mathbf{E}}_2 - \vec{\mathbf{E}}_1\right) \times \mathbf{n} = 0 \tag{21a}$$

$$\left(\vec{\mathbf{B}}_2 - \vec{\mathbf{B}}_1\right) \cdot \mathbf{n} = 0 \tag{21b}$$

$$\left(\vec{\mathbf{H}}_2 - \vec{\mathbf{H}}_1\right) \times \mathbf{n} = \vec{\mathbf{K}}_f \tag{21c}$$

$$\left(\vec{\mathbf{D}}_2 - \vec{\mathbf{D}}_1\right) \cdot \mathbf{n} = \sigma_f, \tag{21d}$$

where $\mathbf{n}$ here indicates the surface normal vector which points from the boundary into the second material. In words, the $\vec{\mathbf{E}}$ field components which are tangential to the material interface must always be continuous across the boundary, as must the $\vec{\mathbf{B}}$ field components which are normal to the material interface. Additionally, the difference in the tangential components of $\vec{\mathbf{H}}$ must equal the free surface current density $\vec{\mathbf{K}}_f$, while the difference in the normal components of $\vec{\mathbf{D}}$ must equal free surface charge density σ_f [37]. In the absence of either free surface current or charge, the tangential components of $\vec{\mathbf{H}}$ and the normal components of $\vec{\mathbf{D}}$ also become continuous across the boundary, respectively.

When a propagating electromagnetic plane wave reaches a material boundary, it can result in both a reflected plane wave which travels back into the original material and a transmitted plane wave which travels onward into the second material. When the electromagnetic boundary conditions are applied to the waves' phase components, assuming an incident plane wave impinges upon a boundary at an angle θ_i with respect to the surface normal, the Law of Reflection and Snell's Law are found to govern the directions of reflected and transmitted wave propagation, respectively. The Law of Reflection

$$\theta_i = \theta_r \tag{22}$$

describes the angle θ_r of the reflected plane wave propagation vector relative to the

surface normal, and Snell's Law

$$\tilde{n}_i \sin\theta_i = \tilde{n}_t \sin\theta_t \tag{23}$$

describes the angle θ_t of the transmitted (refracted) plane wave propagation vector relative to the surface normal. All three waves are found to possess the same frequency, and both the reflected and transmitted plane wave propagation vectors remain within the plane of incidence, which is defined as the plane containing the incident plane wave propagation vector and the surface normal.

In order to describe how much of the incident wave's energy is transferred to the reflected and transmitted waves, the electromagnetic boundary conditions must also be applied to the waves' amplitude components. However, the relationship depends upon the orientation of the electric and magnetic field vectors relative to the plane of incidence, or polarization. Since the electric field, magnetic field, and propagation vectors are always mutually perpendicular, and since the energy carried by an electromagnetic wave can be given in terms of electric field amplitude alone (Equation (8)), it is sufficient to consider all possible electric field orientations for the incident electromagnetic wave. It is most convenient to define two basis cases – when the electric field vector is either perpendicular or parallel to the plane of incidence – which results in the commonly known Fresnel Equations. In their most general form, they apply to any linear, isotropic, homogeneous media, and when combined with Snell's Law, they provide amplitude reflection and transmission coefficients as functions of material property constants and incidence angle. This work focuses on reflection rather

than transmission, so the reflection amplitude coefficients can be generally written

$$r_s \equiv \left(\frac{E_{0r}}{E_{0i}}\right)_{\perp} = \frac{\frac{1}{\mu_i}\cos\theta_i - \frac{1}{\mu_t}\sqrt{\left(\frac{\tilde{n}_t}{\tilde{n}_i}\right)^2 - \sin^2\theta_i}}{\frac{1}{\mu_i}\cos\theta_i + \frac{1}{\mu_t}\sqrt{\left(\frac{\tilde{n}_t}{\tilde{n}_i}\right)^2 - \sin^2\theta_i}} \tag{24a}$$

$$r_p \equiv \left(\frac{E_{0r}}{E_{0i}}\right)_{\parallel} = \frac{\frac{1}{\mu_t}\left(\frac{\tilde{n}_t}{\tilde{n}_i}\right)^2\cos\theta_i - \frac{1}{\mu_i}\sqrt{\left(\frac{\tilde{n}_t}{\tilde{n}_i}\right)^2 - \sin^2\theta_i}}{\frac{1}{\mu_t}\left(\frac{\tilde{n}_t}{\tilde{n}_i}\right)^2\cos\theta_i + \frac{1}{\mu_i}\sqrt{\left(\frac{\tilde{n}_t}{\tilde{n}_i}\right)^2 - \sin^2\theta_i}}. \tag{24b}$$

In many practical cases, particularly when the incident material is air and the reflecting material is non-magnetic, then $\mu_i \approx \mu_t \approx \mu_0$ and $\tilde{n}_i \approx 1$, so that the Fresnel Equations reduce to

$$r_s = \frac{\cos\theta_i - \sqrt{\tilde{n}_t^2 - \sin^2\theta_i}}{\cos\theta_i + \sqrt{\tilde{n}_t^2 - \sin^2\theta_i}} \tag{25a}$$

$$r_p = \frac{\tilde{n}_t^2\cos\theta_i - \sqrt{\tilde{n}_t^2 - \sin^2\theta_i}}{\tilde{n}_t^2\cos\theta_i + \sqrt{\tilde{n}_t^2 - \sin^2\theta_i}}. \tag{25b}$$

The r_s and r_p components describe reflection of the electric fields, but can be converted to power reflection coefficients by

$$F_s = |r_s|^2 \tag{26a}$$

$$F_p = |r_p|^2. \tag{26b}$$

If the incident light is completely unpolarized, which implies equal parts perpendicular and parallel polarization components, then the unpolarized power reflection can be calculated by assuming that half of the reflected light is in each polarization state

$$F = \frac{F_s + F_p}{2}. \tag{27}$$

It is important to note that because its derivation is based on polarization directions relative to surface normal direction, Fresnel reflectance remains consistent only over regions of perfectly flat, infinitely large material surfaces. This idealization becomes important to note in the following definitions of microfacet BRDFs.

2.2 Radiometry Definitions

Radiometry at its heart provides a methodology for measuring the energy content of optical radiation fields and describing how this energy flows through optical systems [6]. Fundamentally, radiometry assumes that radiation and its energy propagate along rays according to the laws of geometric optics, and in conjunction, also typically assumes that radiation sources are incoherent. Ultimately, these assumptions do not allow radiometry alone to sufficiently describe scenarios in which interference, diffraction, or other wave-based phenomena dominate, but nonetheless, it provides a powerful set of tools for measuring and describing optical radiation energy content and transport.

Radiometric Quantities.

First, the total energy contained in a radiation field – or the total energy delivered to a receiver by a radiation field – is termed radiant energy (Q). Radiant energy density (u) is thus defined as the amount of radiant energy contained per unit volume, while radiant flux (Φ) – also known as power – is defined as the amount of radiant energy transported per unit time. The definitions of several important radiometric quantities are based directly on the concept of radiant flux. Radiant exitance (M) is the flux per unit area leaving the surface of a radiation source, irradiance (E) is the flux per unit area received by a surface element, and radiance intensity (I) is the flux per unit solid angle emitted by an entire source into a given direction. It is

worth remembering that solid angle is a measure of field of view from a particular point, scaled by the total possible field of view represented by the entire surrounding sphere. Typically, solid angle is expressed in units of steradians (sr), with the full sphere subtending 4π sr. Mathematically, the solid angle subtended by a surface from a particular point is written

$$\Omega = \frac{A}{r^2}, \tag{28}$$

where A is the surface area projected onto a sphere of radius r surrounding the point.

Finally, radiance (L) is defined as the flux per unit projected area per unit solid angle leaving a source. In other words, it can be described as the power radiating away from differential portions of a source into various differential directions. Source and detector surfaces of finite but arbitrary size and shape can be broken into collections of differential surfaces, and the generic geometry for a single pair of differential source and detector surfaces can be defined as in Figure 1. When the square of the distance between a point and a surface is much larger than the projected surface area ($r^2 >> A$), the projection of a surface onto a sphere becomes relatively flat, so that the expression for solid angle can be approximated instead by a linear surface projection. In this way, the expression for differential solid angle becomes

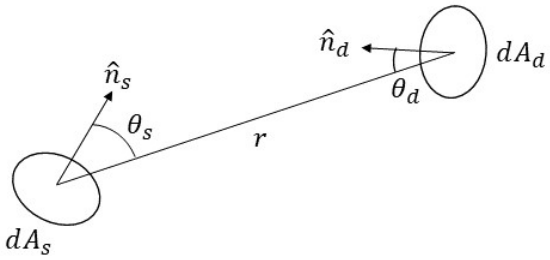

Figure 1. Depiction of geometry between generically oriented radiometric differential source and detector: dA_s is a differential source area, dA_d is a differential detector area, $\hat{n}_s$ is the source normal vector, $\hat{n}_d$ is the detector normal vector, r is the vector from source to detector, $\hat{\theta}_s$ is the angle between $\hat{n}_s$ and r, and $\hat{\theta}_d$ is the angle between $\hat{n}_d$ and r.

$$d\Omega = \frac{dA\cos\theta}{r^2} \tag{29}$$

and thus radiance can be expressed equivalently as

$$\text{Ł} = \frac{d^2\Phi}{\cos\theta_s dA_s d\Omega_d} = \frac{r^2 d^2\Phi}{\cos\theta_s \cos\theta_d dA_s dA_d}. \tag{30}$$

The differential expression for radiance in Equation (30) can be rearranged and integrated over finite arbitrary source and detector areas to solve for total flux as

$$\Phi = \int_{A_d}\int_{A_s} \frac{L\cos\theta_s\cos\theta_d}{r^2}\, dA_s\, dA_d. \tag{31}$$

When the distance between the source and detector is much larger than the area of either, Equation (29) can be used to approximate the solid angle subtended by the source at the detector, as well as the solid angle subtended by the detector at the source, written respectively as

$$d\Omega_s = \frac{dA_s\cos\theta_s}{r^2} \qquad\qquad d\Omega_d = \frac{dA_d\cos\theta_d}{r^2}. \tag{32}$$

Equation (31) can then be rewritten

$$\Phi = \int_{\Omega_d}\int_{A_s} L\cos\theta_s\, dA_s\, d\Omega_d = \int_{\Omega_s}\int_{A_d} L\cos\theta_d\, dA_d\, d\Omega_s. \tag{33}$$

In several ways, radiance can be considered the fundamental radiometric quantity. The radiance theorem states that radiance is conserved during propagation through lossless optical systems, including non-absorptive material boundaries. In addition, within the assumptions of radiometry, radiance characterizes the radiation field independent of source size, detector size, and viewing angle by normalizing radiant flux

by each of those factors. Table 1 summarizes the definitions and units for each radiometric quantity defined above. As evidenced by the form of Equation (30), radiance in general is a function of relative orientation between source and detector. A Lambertian source is one whose radiance by definition remains independent of viewing angle, meaning it radiates equally into all possible directions.

Spectral Quantities.

The radiometric quantities discussed thus far have all referred to the total energy contained within radiation fields across the spectrum of electromagnetic frequencies or wavelengths. However, it is often important to consider how much energy is contained in specific portions of the spectrum. Thus, spectral versions of each radiometric quantity can be used to describe how much of each quantity is contained within differential frequency or wavelength bands. For example, spectral radiance is either radiance per unit frequency (L_ν) or radiance per unit wavelength (L_λ). Total radiometric quantities can then be computed by integrating spectral quantities over desired frequency or wavelength bands. For instance, total flux becomes the integral of spectral flux, written as

$$\Phi = \int \Phi_\nu \, d\nu = \int \Phi_\lambda \, d\lambda. \tag{34}$$

It is important to note that although total radiometric quantities will be equivalent whether they are integrated in terms of frequency or wavelength, the spectral quantities themselves are not necessarily equal even at corresponding frequency-wavelength pairs. Although frequency and wavelength are related through

$$\nu = \frac{v}{\lambda} = \frac{c}{\tilde{n}\lambda} \tag{35}$$

Table 1. Definitions of various radiometric quantities.

Quantity	Symbol	Definition	SI Units
Radiant energy	Q	$\int \Phi dt$	J
Radiant energy density	u	dQ/dV	J/m^3
Radiant flux (power)	Φ or P	dQ/dt	W
Radiant exitance	M	$d\Phi/dA_s$	W/m^2
Irradiance	E	$d\Phi/dA_d$	W/m^2
Radiant intensity	I	$d\Phi/d\Omega$	W/m^{2}sr
Radiance	L	$d^2\Phi/\cos\theta_s dA_s d\Omega_d$	W/sr

where $\tilde{n}$ is the index of refraction for the material through which the radiation is propagating, their differentials are related by

$$d\nu = -\frac{v}{\lambda^2}d\lambda = -\frac{c}{\tilde{n}\lambda^2}d\lambda \tag{36}$$

so that the two forms of spectral radiometric quantities are instead related as

$$\nu\Phi_\nu = \lambda\Phi_\lambda. \tag{37}$$

Blackbody Radiation & Conservation of Energy.

As alluded to in Section 2.1, electromagnetic radiant energy incident on a surface is either reflected, absorbed, or transmitted in some combination. According to the conservation of energy, when each piece is normalized by the incident energy, the sum of total reflectance (ρ), absorption (α), and transmission (T) must equal unity:

$$\rho + \alpha + T = 1. \tag{38}$$

Due to the electromagnetic boundary conditions which require equivalent incident, reflected, absorbed, and transmitted radiation frequencies, Equation (38) holds in terms of either total energy or spectral energy.

In addition, however, materials may also emit their own radiation spontaneously through thermal mechanisms based upon their temperature. According to Kirchhoff's law of thermal radiation, materials in thermal equilibrium absorb exactly as much radiation as they emit at each wavelength. In other words, spectral absorptivity and spectral emissivity are equivalent, which can be written simply

$$\alpha_\lambda = \epsilon_\lambda. \tag{39}$$

Thus, an ideal emitter at thermal equilibrium must also be an ideal absorber. Such an ideal material is known as a blackbody, because per the law of conservation of energy, an object which absorbs all radiation does not reflect any. Derived by applying the quantization of energy within photons, as prescribed in quantum mechanics ($E = h\nu$), the Planck radiation law describes the spectral radiance of blackbodies as a function of temperature. Blackbody spectral radiance can be written either in terms of frequency or wavelength as

$$L_{B_\nu} = \frac{2h\nu^3}{(c/\tilde{n})^2} \frac{1}{e^{\frac{h\nu}{kT}} - 1} \tag{40a}$$

$$L_{B_\lambda} = \frac{2h\,(c/\tilde{n})^2}{\lambda^5} \frac{1}{e^{\frac{h(c/\tilde{n})}{\lambda kT}} - 1}, \tag{40b}$$

where $\tilde{n}$ is the index of refraction for the material in which the radiation is propagating. For many practical applications, including air and free space propagation, this index of refraction is very near unity, so the expressions simplify accordingly.

In situations involving opaque materials in thermal equilibrium, transmittance is zero and emissivity equals absorptivity. Then, Equation (38) can be simplified and rearranged to express reflectance as

$$\rho = 1 - \epsilon. \tag{41}$$

Although this relationship describes how much energy is reflected, it does not practically describe where the energy is reflected spatially, beyond the simple law of reflection.

2.3 Bi-Directional Reflectance Distribution Functions

Definition.

In 1965, Nicodemus formally introduced the concept of a bi-directional reflectance distribution function (BRDF) to the field of radiometry, which he defined as the ratio of exiting radiance to incident irradiance [50]. Mathematically, the BRDF can be broadly defined as

$$f_r(\hat{\boldsymbol{\omega}}_i, \hat{\boldsymbol{\omega}}_s, \lambda) = \frac{dL_s(\hat{\boldsymbol{\omega}}_i, \hat{\boldsymbol{\omega}}_s, \lambda)}{dE_i(\hat{\boldsymbol{\omega}}_i, \lambda)}, \tag{42}$$

where the unit vector $\hat{\boldsymbol{\omega}}_i$ defines the direction of the incident ray of light, and the unit vector $\hat{\boldsymbol{\omega}}_s$ vector defines the direction of reflected (scattered) rays of light [51]. Both $\hat{\boldsymbol{\omega}}_i$ and $\hat{\boldsymbol{\omega}}_s$ are often written in terms of the spherical coordinates (θ_i, ϕ_i) and (θ_s, ϕ_s), respectively, as shown in Figure 2. As a ratio of vector functions in differential form, the BRDF describes the spatial distribution of reflected light, telling us how much of any incident light upon a surface is reflected into each possible direction, and showing that the reflected distribution can vary as a function of both incident direction and wavelength. As a spatial distribution, the BRDF carries units of inverse solid angle, or 1/sr.

In applications, the BRDF is often used within the rendering equation to compute the observed radiance L_s of a source object [41], written generally as

$$L_s(\vec{\boldsymbol{x}}, \hat{\boldsymbol{\omega}}_s, \lambda, t) = L_e(\vec{\boldsymbol{x}}, \hat{\boldsymbol{\omega}}_s, \lambda, t) + \int_\Omega f_r(\vec{\boldsymbol{x}}, \hat{\boldsymbol{\omega}}_i, \hat{\boldsymbol{\omega}}_s, \lambda, t) L_i(\vec{\boldsymbol{x}}, \hat{\boldsymbol{\omega}}_i, \lambda, t) \cos\theta_i d\hat{\boldsymbol{\omega}}_i. \tag{43}$$

The first term L_e describes self-emission, while the second term describes reflection

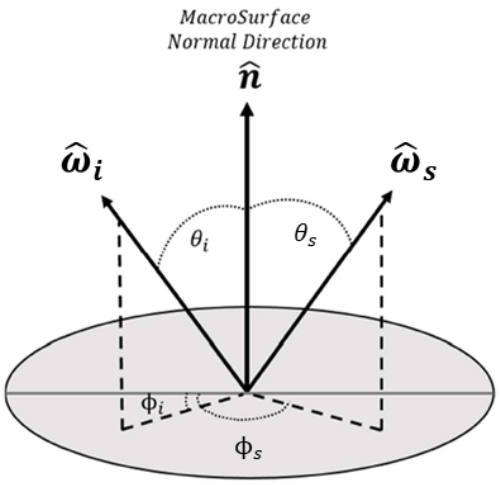

Figure 2. Depiction of the BRDF incident and scatter directions $\hat{\omega}_i$ and $\hat{\omega}_s$ written in terms of spherical coordinates (θ_i, ϕ_i) and (θ_s, ϕ_s), respectively. The material surface is depicted by the gray circle. The zenith angles θ_i and θ_s are measured relative to the overall material surface normal $\hat{n}$, while the azimuth angles ϕ_i and ϕ_s are measured relative to an arbitrary direction along the material surface, as indicated by the solid line.

based on both the incident radiance L_i and the material BRDF. This equation contains two more inputs than Equation (42): $\vec{\boldsymbol{x}}$ for denoting different spots on the material surface, and t for denoting changes over time. However, in this work, material surface illumination spots will be held constant, and time-varying material properties will not be considered, so these particular inputs will be ignored.

Properties.

By applying the radiometric definitions for radiance and irradiance as established in Section 2.2 to the definition in Equation (42), and ignoring the wavelength dependence, the BRDF can also be expressed in terms of experimentally available incremental quantities as

$$f_r(\hat{\boldsymbol{\omega}}_i, \hat{\boldsymbol{\omega}}_s) = \frac{\frac{\delta\Phi_s}{\delta A_s \cos\theta_s \delta\Omega_d}}{\frac{\delta\Phi_i}{\delta A_s}} = \frac{\delta\Phi_s}{\delta\Phi_i \cos\theta_s \delta\Omega_d}, \tag{44}$$

where the quantity $\delta\Phi_i$ is the total incident flux on a small material surface area; $\delta\Phi_s$ is the scattered flux measured by a small detector area which subtends a solid angle $\delta\Omega_d$; and θ_s is the zenith angle between the material surface normal and the scattered direction [48].

Conceptually, the detector solid angle $\delta\Omega_d$ can be exchanged with scattered solid angle $\delta\hat{\boldsymbol{\omega}}_s$ due to a shared geometric interpretation. The quantity $\delta\Phi_s/\delta\Omega_d$ (or $\partial\Phi_s/\partial\hat{\boldsymbol{\omega}}_s$) represents the scattered power spatial distribution, which remains an implicit function of $\hat{\boldsymbol{\omega}}_i$, and requires scaling by the incident power $\delta\Phi_i$ and scatter angle projection $\cos\theta_s$ to form the BRDF. For a single-direction source, the illuminated sample area δA_s would in truth scale to $\delta A_s/\cos(\theta_i)$, effectively reducing the irradiance at higher incident angles. However, the detector would also view the same scaled sample area, so the incremental areas still cancel for any incident geometry. When the source illumination and detector sizes are sufficiently small compared to the distances between them them, the incremental form with δ symbols (which denote smallness of detector and sample illumination spot sizes) can be dropped, so that Equation (44) can be written instead

$$f_r(\hat{\boldsymbol{\omega}}_i, \hat{\boldsymbol{\omega}}_s) = \frac{\Phi_s}{\Phi_i \cos\theta_s \Omega_d}. \tag{45}$$

Equation (45) can be further manipulated to demonstrate several important theoretical BRDF properties. First, due to conservation of energy, for a given incident direction, the integral of the BRDF over the full hemisphere of possible reflected directions – which is also known as directional-hemispherical reflectance (DHR) – must equal the total reflectance at that incident direction. In general, total reflectance is the ratio between total scattered power and total incident power ($\rho = \Phi_s/\Phi_i$). Thus, in terms of both solid angles and spherical coordinates, DHR can be expressed

$$\rho(\hat{\boldsymbol{\omega}}_i) = \int f_r(\hat{\boldsymbol{\omega}}_i, \hat{\boldsymbol{\omega}}_s) \cos\theta_s \, d\hat{\boldsymbol{\omega}}_s = \int_0^{2\pi} \int_0^{\frac{\pi}{2}} f_r(\hat{\boldsymbol{\omega}}_i, \hat{\boldsymbol{\omega}}_s) \cos\theta_s \sin\theta_s \, d\theta_s \, d\phi_s, \tag{46}$$

where $d\hat{\boldsymbol{\omega}} = \sin\theta \, d\theta \, d\phi$ provides the conversion to spherical coordinates.

Secondly, due to the Helmholtz reciprocity of Maxwell's Equations, the incident and reflected directions are interchangeable, so that

$$f_r(\hat{\boldsymbol{\omega}}_i, \hat{\boldsymbol{\omega}}_s) = f_r(\hat{\boldsymbol{\omega}}_s, \hat{\boldsymbol{\omega}}_i). \tag{47}$$

As a consequence, for a given reflected direction, the integral of the BRDF over the full hemisphere of possible incident directions – which is also known as hemispherical-directional reflectance (HDR) – must also equal the total reflectance at that reflected direction, expressed

$$\rho(\hat{\boldsymbol{\omega}}_s) = \int f_r(\hat{\boldsymbol{\omega}}_i, \hat{\boldsymbol{\omega}}_s) \cos\theta_i \, d\hat{\boldsymbol{\omega}}_i = \int_0^{2\pi} \int_0^{\frac{\pi}{2}} f_r(\hat{\boldsymbol{\omega}}_i, \hat{\boldsymbol{\omega}}_s) \cos\theta_i \sin\theta_i \, d\theta_i \, d\phi_i. \tag{48}$$

Although the relationships between DHR, HDR, and BRDF physically hold true for any material surface, BRDF models are not always designed to mathematically maintain these relationships.

Ideal Cases.

Perfectly specular reflection represents the first idealized limiting case. For a perfectly smooth flat surface, with no subsurface scattering features, the BRDF reduces to a perfectly specular model, which can be represented mathematically as

$$f_r(\hat{\boldsymbol{\omega}}_i, \hat{\boldsymbol{\omega}}_s) = \rho\delta(\theta_i - \theta_s)\delta(\phi_i + \pi - \phi_s). \tag{49}$$

Due to the delta function, the BRDF is identically zero for every possible scattered direction except the one satisfying the simple law of reflection. Here, the delta function value is infinite, but integrates to unity, which is then scaled by total reflectance

ρ.

Perfectly diffuse (or Lambertian) reflection represents the opposite limiting case. Such a surface has as constant reflectance spatial distribution, which can be mathematically written

$$f_r = \frac{\rho}{\pi}. \tag{50}$$

The Lambertian BRDF does not depend on either incident or scattered angle, but integrates across the entire hemisphere of possible scattered directions to ρ.

Observationally, light reflected from different material surfaces can display very different spatial distribution patterns, but all material BRDFs fall somewhere between these two limiting cases. As a result, many models utilize some weighted combination of specular and diffuse components.

Microfacet Models.

There are many classes and categories of BRDF models, and like any set of models, they span a broad range of tradeoffs between simplicity and accuracy. This work is primarily interested in models with more physics-based formulations (also known as theoretical models), largely because remote sensing attempts to understand the links between measurement and physical phenomena. Within physics-based BRDF models, this work is most interested in two major classes known as microfacet models and scalar wave optics models, but with emphasis on microfacet models. At a fundamental level, microfacet models describe reflection from surfaces in terms of geometric optics, which tends to sacrifice accuracy by neglecting wave-based phenomena in order to achieve model simplicity and computational efficiency. Scalar wave optics models, on the other hand, account for scalar wave-based effects through increased mathematical rigor, but in general require much more complex calculations, which can become too cumbersome for applications such as remote sensing.

In 1967, Torrance and Sparrow first discussed a mechanism by which to explain and model observed differences in material BRDFs, namely by visualizing a material surface as comprised of many very small microfacets [70]. Each microfacet has its own normal vector, apart from the material macrosurface normal, and each can be treated as an individual reflecting mirror. For any possible combination of incident and reflected directions, only those microfacets whose orientation satisfies the law of reflection contribute specular reflection. Materials can have different microfacet surface distribution characteristics, which in turn affect the full spatial distribution of reflected light. This modeling technique spawned the microfacet class of BRDFs still in use today [12].

In the decades since Torrance and Sparrow introduced the microfacet BRDF, dozens of distinct models have been developed, each with different mathematical terms and formulations designed to handle different material properties and reflection phenomena. Although still based principally on the concept of first-surface specular reflection from microfacets, many current models also contain additional terms for addressing diffuse components. The diffuse terms can generally be split into a semi-diffuse (volumetric) term – often used to capture wide-angle effects such as subsurface impurity scattering – as well as a perfectly diffuse (Lambertian) term – often used as a catch-all scaling factor. The most common general mathematical representation of the microfacet BRDF is

$$f_\mu(\hat{\boldsymbol{\omega}}_i, \hat{\boldsymbol{\omega}}_s) = \rho_s S(\hat{\boldsymbol{\omega}}_i, \hat{\boldsymbol{\omega}}_s) + \rho_v V(\hat{\boldsymbol{\omega}}_i, \hat{\boldsymbol{\omega}}_s) + \frac{\rho_d}{\pi}, \tag{51}$$

where ρ_s, ρ_v, and ρ_d represent weighting coefficients for the specular, volumetric, and Lambertian contributions, respectively [9]. In practice, although many common microfacet models incorporate the Lambertian term, many neglect the volumetric term [9].

Microfacet Coordinates.

The specular portion S of the microfacet model typically contains several different sub-expressions which each capture different physical aspects of specular reflection. The four principal sub-expressions include a Fresnel reflectance term F, a microfacet distribution function D, a geometric attenuation term G, and a cross-section conversion term σ. In many ways, the microfacet distribution term can be considered the heart of the microfacet BRDF model because it provides the probabilistic description for the orientation of a material's microfacets, and serves as a proxy for the roughness or smoothness of a material surface.

In order to properly compute microfacet specular reflection, it is most convenient to introduce microfacet coordinates [57]. As depicted in Figure 3, the unit vector $\hat{\boldsymbol{\omega}}_h$ represents the normal vector of a given microfacet, which differs in general from the macrosurface normal vector $\hat{\boldsymbol{n}}$, with associated spherical coordinates θ_h and ϕ_h. In addition, the unit vector $\hat{\boldsymbol{\omega}}_d$ represents the incident vector $\hat{\boldsymbol{\omega}}_i$ rotated from macrosurface to microfacet coordinates. In order to convert any given macrosurface incident and scattered angle pair into microfacet coordinates, the following conversion applies:

$$\hat{\boldsymbol{\omega}}_h = \frac{\hat{\boldsymbol{\omega}}_i + \hat{\boldsymbol{\omega}}_s}{||\hat{\boldsymbol{\omega}}_i + \hat{\boldsymbol{\omega}}_s||} \qquad\qquad \hat{\boldsymbol{\omega}}_d = \mathbb{R}_y(-\theta_h)\mathbb{R}_z(-\phi_h)\hat{\boldsymbol{\omega}}_i. \tag{52}$$

The notation $\mathbb{R}_a(\alpha)$ represents a rotation about the axis a by the angle α. As can be seen in Equation (52), $\hat{\boldsymbol{\omega}}_h$ equivalently represents the half-angle direction located exactly between an incident and scatter direction pair.

Microfacet coordinates are important because the specular reflection term F in reality depends directly upon microfacet orientation rather than the macrosurface normal. In addition, the microfacet distribution function D is most easily expressed as a function of $\hat{\boldsymbol{\omega}}_h$ directly.

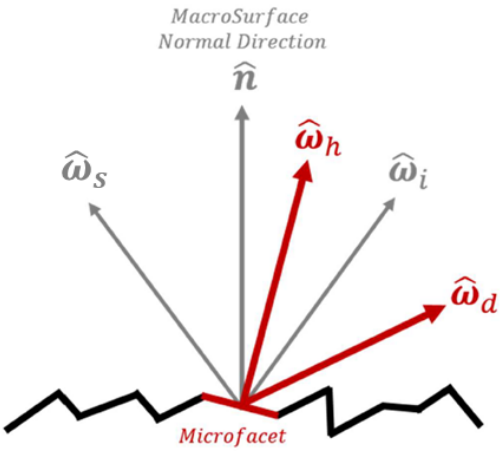

Figure 3. Depiction of the microfacet coordinate vectors where $\hat{\omega}_h$ represents the microfacet normal direction and $\hat{\omega}_d$ represents the incident direction in microfacet rather than macrosurface coordinates.

Geometric attenuation terms commonly denoted G can vary in formulation, but exist mainly to account for shadowing and obscuration. For certain geometries, some microfacet orientations may block the light from reaching other microfacets, similar to how a mountain may block sunlight from reaching the valley surface when the Sun is low enough. Conversely, for some geometries, incident light may reach microfacets in a valley, but other microfacets still block light reflected in certain directions, similar to how an aircraft flying relatively low over the mountains may not be able to see down into every valley. Along with the cross-section conversion term σ which exists to convert planar scattering cross-section into BRDF, geometric attenuation terms G are most often expressed best in macrosurface coordinates.

Together, the specular portion of a microfacet BRDF may be generally written

$$S(\hat{\boldsymbol{\omega}}_i, \hat{\boldsymbol{\omega}}_s) = D(\hat{\boldsymbol{\omega}}_h)F(\hat{\boldsymbol{\omega}}_d)G(\hat{\boldsymbol{\omega}}_i, \hat{\boldsymbol{\omega}}_s)\sigma(\theta_i, \theta_s). \tag{53}$$

To summarize in words, the specular microfacet calculation begins by first taking a

desired incident and scattered angle pair $(\hat{\boldsymbol{\omega}}_i, \hat{\boldsymbol{\omega}}_s)$, calculating the microfacet orientation $\hat{\boldsymbol{\omega}}_h$ which satisfies the law of reflection for that geometry, determining relatively how many microfacets are oriented in that specular direction based on the distribution, and then determining the magnitude of the reflection according to Fresnel reflection. The geometric attentuation accounts for shadowing and obscuration, and the cross-section conversion terms scales from a planar surface to a hemispherical reflectance distribution.

Microfacet Distribution Functions.

In the absence of volumetric terms, the microfacet distribution function is the key component governing how much light gets reflected into different directions for a microfacet model. When the distribution function dictates higher probabilities for microfacet orientations near the macrosurface normal – representing a smoother surface – the reflectance distribution will cluster tightly near the specular direction. In contrast, when the microfacet orientations are more evenly distributed away from the macrosurface normal – representing a rougher surface – the modeled reflection becomes more diffuse.

In general, there are two types of distribution functions: isotropic and anisotropic. Isotropic distribution functions assume that microfacet orientation statistics for a material surface are independent of the azimuthal direction ϕ. In other words, the distribution assumes azimuthal symmetry of microfacet orientation statistics about the macrosurface normal, so that all cross sections of microfacet orientation statistics along any azimuthal plane on the material surface are equivalent. In contrast, anisotropic distribution functions do not assume azimuthal symmetry, but instead allow for different microfacet orientation statistics along different azimuthal planes.

Ideally, since they are probability distribution functions, all microfacet distribution

functions should be integrable, non-negative, and normalized to integrate to unity over a full hemisphere [71]. The normalization condition can be written

$$\int_0^{2\pi} \int_0^{\frac{\pi}{2}} D(\theta_h, \phi_h) \cos\theta_h \sin\theta_h \, d\theta_h \, d\phi_h = 1. \tag{54}$$

However, in practice, not all distribution functions utilized in microfacet models are normalized, which means that care must be taken when comparing or evaluating different functions, especially when implementing flexible BRDFs as described in the next section.

There are numerous microfacet BRDF models in existence, some sharing common distribution functions, but varying in other terms. The following paragraphs attempt to summarize commonly used microfacet distribution functions, particularly in the remote sensing field, but also delving somewhat into the computer graphics community.

The Beard-Maxwell microfacet BRDF model has historically been one of the most widely adopted models for SDA applications [45, 46]. The Beard-Maxwell model was originally developed in a research effort funded by the Air Force Research Laboratory in 1972 [48]. It introduced the volumetric term, as well as incorporated spectral and polarization characteristics, in order to better model semi-diffuse reflections prevalent in matte or semi-gloss paints, particularly such as those found on targets like ballistic missiles [19]. The Beard-Maxwell model has been described as an empirical microfacet model, because historically it has utilized empirically measured reflectance values to generate material-specific microfacet distribution functions. The original form of the Beard-Maxwell microfacet distribution function has the form

$$D_{bm,u}(\hat{\boldsymbol{\omega}}_h) = \frac{4\rho_{fs}(\hat{\boldsymbol{\omega}}_h)\cos^2\theta_h}{F(0)}, \tag{55}$$

where the quantity ρ_{fs} comes directly from laboratory BRDF measurements known as bi-static scans. In such scans, the source and detector locations are placed as closely together as practical, and reflectance measurements are taken at various orientations relative to the sample. By co-locating source and detector, only those microfacets whose normals point back toward the source and detector will theoretically contribute to the reflectance measurement. Thus, the orientation of the sample macrosurface normal relative to the source and detector direction corresponds directly to a certain microfacet orientation $\hat{\boldsymbol{\omega}}_h$, and the incident angle for contributing microfacets $\hat{\boldsymbol{\omega}}_d$ is held to zero. This distribution can be isotropic when measurements are taken by varying θ_h in one azimuthal plane only and assuming other planes are equivalent, or it can be anisotropic by conducting measurements through other azimuthal planes by also varying ϕ_h.

The term $F(0)$ in the denominator scales the measured quantity by normal incidence Fresnel reflection. As a result of their empirical nature, Beard-Maxwell distribution functions typically apply only to the specific materials for which they were measured, but they are able to capture a wide range of spatial distribution shapes, unlike those which rely on single functional forms – such as Gaussians, Lorentzians, etc. – to fit data. It is important to note that Beard-Maxwell distribution functions are not generally normalized; the subscript includes u to denote un-normalized.

Due to the flexibility offered by the empirical nature of the Beard-Maxwell model, coupled with its particular success modeling semi-gloss paints in visible and infrared wavelengths, Crockett described the Beard-Maxwell model in 2003 as the "first, most important, and only one that should seriously be used for accurately modeling target radiometry" [19]. Even today, it maintains particular prominence within the Air Force's material database, which contains models for over 300 space object materials for radiometric analysis purposes [45, 46], and also serves as the baseline BRDF model

for the Nonconventional Exploitation Factors Data System (NEFDS) managed by the National Institute of Science and Technology (NIST) [1, 28].

As opposed to the original formulation, the Modified Beard-Maxwell BRDF model utilizes a modified Cauchy (or Lorentzian) distribution function. In the literature [28], it can be found written without normalization as

$$D_{mbm,u}(\theta_h) = \frac{B}{\cos\theta_h \left(s^2 + \tan^2\theta_h\right)}. \tag{56}$$

Since it is a function of θ_h but not ϕ_h, it is an isotropic distribution.

The Blinn-Phong model, related to Phong's original algorithm, but with enhanced capabilities for modeling asymmetric specular reflection patterns, utilizes a normalized isotropic cosine lobe distribution with the form

$$D_c(\theta_h) = \frac{k+2}{2\pi}(\cos\theta_h)^k, \tag{57}$$

where the fraction in front provides the normalization factor for the exponentiated cosine [53]. Ashikhman and Shirley modified the cosine lobe distribution to form the following normalized anisotropic version, written by Butler [9] as

$$D_{c,a}(\hat{\boldsymbol{\omega}}_h) = \frac{\sqrt{k_x+2}\sqrt{k_y+2}}{2\pi}(\cos\theta_h)^{k_x\cos^2\phi_h + k_y\sin^2\phi_h}, \tag{58}$$

where the subscript a denotes anisotropic. In this formulation, the lone fit parameter k, which was responsible for modulating the width of the cosine lobe distribution in the isotropic form, has now been substituted by the expression $k_x\cos^2\phi_h + k_y\sin^2\phi_h$, so that the distribution's width varies elliptically between the value k_x in one azimuthal plane and the value k_y in its orthogonal azimuthal plane. When $k_x = k_y$, the expression reduces to the normalized isotropic distribution. Although often less

physics-based in their derivation and validation [19], models with cosine lobe distribution functions are also frequently utilized in SDA applications [16, 46].

The Sandford-Robertson model is one of the other few microfacet BRDF models to include a volumetric term for semi-diffuse scattering, and has also been utilized in SDA modeling efforts [46]. It was originally developed to model aircraft paints, and was derived specifically to conserve energy via Kirchhoff's Law, while also maintaining a purely analytical form [58, 9]. The Sandford-Robertson model employs an isotropic elliptical microfacet distribution function, which was originally derived by Trowbridge and Reitz [71]. The model presented in the literature does contain a normalization factor, but it does not simply normalize the microfacet distribution function alone, and is expressed in terms of θ_i rather than θ_h [58, 18]. The un-normalized distribution function can be written

$$D_{e,u}(\theta_h) = \frac{1}{\left(c^2 \cos^2 \theta_h + \sin^2 \theta_h\right)^2}, \tag{59}$$

where the parameter c is constrained to $0 \leq c \leq 1$.

While working on physically-based shading at Disney Animation Studios, Burley modified the isotropic elliptical distribution function by adding an arbitrary exponent to the denominator in an effort to better match experimental data in the tails of the distribution [8]. He named the modified function the Generalized-Trowbridge-Reitz (GTR) distribution, which can be written with an analytical normalization factor:

$$D_{gtr}(\theta_h) = \frac{(\gamma - 1)\left(c^2 - 1\right)}{\pi\left(1 - c^{2-2\gamma}\right)} \frac{1}{\left(c^2 \cos^2 \theta_h + \sin^2 \theta_h\right)^\gamma}. \tag{60}$$

In this form, though, there is a singularity in the normalization expression when

$\gamma = 1$. For that specific case, the normalization can be re-written

$$D_{gtr}(\theta_h)|_{\gamma=1} = \frac{(c^2-1)}{\pi \ln c^2} \frac{1}{\left(c^2 \cos^2 \theta_h + \sin^2 \theta_h\right)}. \tag{61}$$

Burley also presented an anisotropic formulation for the GTR distribution function by allowing the parameter c^2 to vary with azimuthal plane ϕ_h by substituting the expression $\frac{c_x^2 c_y^2}{c_x^2 \sin^2 \phi_h + c_y^2 \cos^2 \phi_h}$. When $\gamma = 2$ as in the original Trowbridge-Reitz elliptical formulation, the normalized anisotropic distribution becomes

$$D_{gtr,a}(\hat{\boldsymbol{\omega}}_h)|_{\gamma=2} = \frac{1}{\pi c_x c_y} \frac{1}{\left(\cos^2 \theta_h + \sin^2 \theta_h \left(\frac{\cos^2 \phi_h}{c_x^2} + \frac{\sin^2 \phi_h}{c_y^2}\right)\right)^2}. \tag{62}$$

However, for any other arbitray γ, the anisotropic GTR distribution does not have a closed form [8].

More recently, SDA modeling efforts have incorporated a model which incorporates the Hyper-Cauchy microfacet distribution function introduced by Wellems [45]. With normalization included, the isotropic distribution can be written

$$D_{hc}(\theta_h) = \frac{\gamma - 1}{\pi \sigma^2} \frac{\sigma^\gamma}{\cos^4 \theta_h \left(\sigma^2 + \tan^2 \theta_h\right)^\gamma} = \frac{(\gamma - 1)\, \sigma^{2\gamma - 2}}{\pi \cos^4 \theta_h \left(\sigma^2 + \tan^2 \theta_h\right)^\gamma} \tag{63}$$

where $\gamma > 1$ is required. The first expression on the left shows the normalization factor separated from the distribution, and the second shows the more common combined expression found in literature [76, 9]. Although not published, an anisotropic version would simply require substituting at least one of the fit parameters (σ or γ) with an expression that varies with ϕ_h.

The Cook-Torrance microfacet model is commonly implemented by a broad range of communities, ranging from remote sensing to computer graphics. It employs the Beckmann distribution, which is based upon the Gaussian function. Although slight

variations exist, in its basic form, the normalized isotropic form has been presented as

$$D_b(\theta_h) = \frac{1}{\pi m^2} \frac{1}{\cos^4 \theta_h} \exp\left[-\frac{\tan^2 \theta_h}{m^2}\right]. \tag{64}$$

The anisotropic form substitutes m^2 for $\frac{m_x^2}{\cos^2 \phi_h} + \frac{m_y^2}{\sin^2 \phi_h}$, which can be re-normalized to form

$$D_{b,a}(\hat{\boldsymbol{\omega}}_h) = \frac{1}{\pi m_x m_y} \frac{1}{\cos^4 \theta_h} \exp\left[-\tan^2 \theta_h \left(\frac{m_x^2}{\cos^2 \phi_h} + \frac{m_y^2}{\sin^2 \phi_h}\right)\right]. \tag{65}$$

Finally, Ribardiere describes the class of normalized isotropic microfacet distribution functions which encapsulates many of the functions already presented, written with the general form

$$D_r(\theta_h) = \frac{(C-1)B}{\pi \cos^4 \theta_h (1 + B \tan^2 \theta_h)^C}, \tag{66}$$

with several notable cases [55]. First, when $B = \frac{1}{\sigma^2}$ and $C = 2$, this distribution corresponds with the isotropic elliptical distribution, also known as the original Trowbridge-Reitz distribution, given in Equation (61) when $\gamma = 2$. Second, when $C \to \infty$, the product BC tends to $\frac{1}{\sigma^2}$, and the distribution tends to the Beckmann distribution [55]. Third, when $B = \frac{1}{\sigma^2}$ and $C = \gamma$, this distribution corresponds to the Hyper-Cauchy distribution [55]. Ribardiere then goes on to propose utilizing $B = \frac{1}{\sigma^2(\gamma-1)}$ and $C = \gamma$, which reduces to what he calls the normalized Student's t-Distribution given by

$$D_{std}(\theta_h) = \frac{(\gamma-1)^\gamma \sigma^{2\gamma-2}}{\pi \cos^4 \theta_h \left((\gamma-1)\sigma^2 + \tan^2 \theta_h\right)^\gamma}, \tag{67}$$

where $\gamma > 1$ is required just like for the Hyper-Cauchy distribution. This distribution is interesting because unlike the Hyper-Cauchy, the Student's t-distribution tends to

the elliptical original Trowbridge-Reitz when $\gamma = 2$ but also tends to the Beckmann when $\gamma \to \infty$ [55]. Ribardiere also provides an anisotropic formulation written

$$D_{std,a}(\theta_h) = \frac{1}{\pi\sigma_x\sigma_y \cos^4\theta_h \left(1 + \frac{\tan^2\theta_h}{\gamma - 1}\left(\frac{\cos^2\phi_h}{\sigma_x^2} + \frac{\sin^2\phi_h}{\sigma_y^2}\right)\right)^{\gamma}}, \tag{68}$$

although it is not explicitly described whether or not this anisotropic formulation is properly normalized.

Despite the multitude of microfacet BRDF models and microfacet distribution functions, coupled with the widespread proliferation and application of microfacet BRDF models to a multitude of problems in the last several decades, Crockett offers the following important words of caution:

"It is important to remember that all BRDF equations, while constructed using physics-backed theories like geometric optics, are not derived physical equations of light like Maxwell's equations. BRDFs are informed, gross mathematical approximations to describe the observed nature of light's reflective properties. The best, most realistic BRDF equations are only accurate for describing light as it behaves within one narrow frequency band, for one type of material. Those who create new BRDFs often ignore light's complicated diffractive properties and maintain simplified assumptions...The method for deriving the BRDF at a wavelength at which the BRDF parameters have not been explicitly measured is very much open to interpretation and personal inclination" [19] .

Thus, choosing the right BRDF model or microfacet distribution function for a specific material application, including SDA, can be very challenging, and certainly depends on matching quality measurements with quality models [46].

Flexible and Wave Optics Improvements.

In the past several years, Butler and Marciniak identified a handful of methods for overcoming several weaknesses of parametric BRDF models. A primary drawback with traditional parametric microfacet BRDF models is a formulation which insists on fitting every material reflectance pattern to a single microfacet distribution shape. However, Butler and Marciniak showed that parametric BRDFs could be tailored to specific materials by interchanging individual terms among of BRDF models, such as the microfacet distribution function [9]. For instance, the specular peak of one material might never fit well to a normalized Beckmann distribution, no matter how the fit parameters are varied, but may fit very well to a Hyper-Cauchy distribution, even without changing any other aspects of the underlying BRDF model. This technique for interchanging individual parametric BRDF components to provide better material-specific properties was termed "adaptive BRDFs" [9] or "flexible BRDFs" [46].

Unlike microfacet models, wave optics (or physical optics) models do not ignore the wave nature of light. Instead, models such as the Modified Beckmann-Kirchhoff [36] model and Generalized Harvey-Shack [35, 44] model base their formulations on Fourier diffraction theory and describe how light propagates after reflection from surfaces with various statistical roughness distributions. Although they are able to handle wavelength-dependent phenomena such as diffraction, they are much more computationally intensive and often do not possess closed-form general solutions, and therefore less attractive to remote sensing applications.

However, based on work comparing microfacet and wave optics formulations, the

Q polarization factor

$$Q_{ss} = \left| \frac{(\tilde{n}^2 - 1)\cos(\phi_s - \pi)}{(\cos\theta_i + \sqrt{\tilde{n}^2 - \sin^2\theta_i})(\cos\theta_s + \sqrt{\tilde{n}^2 - \sin^2\theta_s})} \right|^2 \tag{69a}$$

$$Q_{sp} = \left| \frac{(\tilde{n}^2 - 1)\sqrt{\tilde{n}^2 - \sin^2\theta_s}\sin(\phi_s - \pi)}{(\cos\theta_i + \sqrt{\tilde{n}^2 - \sin^2\theta_i})(\tilde{n}^2\cos\theta_s + \sqrt{\tilde{n}^2 - \sin^2\theta_s})} \right|^2 \tag{69b}$$

$$Q_{ps} = \left| \frac{(\tilde{n}^2 - 1)\sqrt{\tilde{n}^2 - \sin^2\theta_i}\sin(\phi_s - \pi)}{(\tilde{n}^2\cos\theta_i + \sqrt{\tilde{n}^2 - \sin^2\theta_i})(\cos\theta_s + \sqrt{\tilde{n}^2 - \sin^2\theta_s})} \right|^2 \tag{69c}$$

$$Q_{pp} = \left| \frac{(\tilde{n}^2 - 1)\left(\sqrt{\tilde{n}^2 - \sin^2\theta_i}\sqrt{\tilde{n}^2 - \sin^2\theta_s}\cos(\phi_s - \pi) - \tilde{n}^2\sin\theta_i\sin\theta_s\right)}{(\tilde{n}^2\cos\theta_i + \sqrt{\tilde{n}^2 - \sin^2\theta_i})(\tilde{n}^2\cos\theta_s + \sqrt{\tilde{n}^2 - \sin^2\theta_s})} \right|^2 \tag{69d}$$

$$Q = Q_{ss} + Q_{sp} + Q_{ps} + Q_{pp} \tag{69e}$$

can be used to replace F, G, and σ within Equation (54) [10]. The modification

$$f_r(\hat{\boldsymbol{\omega}}_{\boldsymbol{i}}, \hat{\boldsymbol{\omega}}_{\boldsymbol{s}}) = \rho_s D(\hat{\boldsymbol{\omega}}_{\boldsymbol{h}}) \frac{Q(n, \hat{\boldsymbol{\omega}}_{\boldsymbol{i}}, \hat{\boldsymbol{\omega}}_{\boldsymbol{s}})}{2(\cos\theta_i + \cos\theta_s)^2} + \frac{\rho_d}{\pi} \tag{70}$$

improves microfacet model performance at larger scatter angles, even when ignoring the volumetric term, while still leaving flexibility in the choice of D [25].

BRDF Measurement.

There are many methods by which to measure material BRDFs, but the fundamental required components include a light source, material sample, detector, and some method by which to change their relative orientations and sample the hemisphere for incident and scattered directions. Equation (45) provides the basic framework for calculating BRDF from measurable quantities. Incident flux Φ_i can be calculated by measuring the unimpeded incident beam power, scatter angle θ_s can be measured from the relative orientation between illuminated sample spots and detector location, solid angle Ω_d can be calculated based on detector size and distance from the sam-

ple, and scatter flux Φ_s is the detector's power reading as a function of orientation. In particular, when incident flux is measured using the same detector used to measure scatter flux, which is the method employed by the CASI®, then the calculation produces absolute BRDF values, rather than relative [13].

Due to the multi-dimensional functionality of the BRDF, high-resolution samples of material BRDFs throughout the entire space are difficult and time-consuming to obtain. In fact, the vast majority of BRDF measurement research deals only with isotropic measurements [26], and by extension, corresponding modeling efforts also assume isotropic distributions. One common measurement technique involves placing some combination of the light source, sample, and detector onto goniometers which provide motion with high angular resolution.

For example, the CASI® in use at the Air Force Institute of Technology (AFIT), originally designed and produced by John Stover and his team [56], utilizes interchangeable laser sources from a fixed direction, but varies incident and scatter directions relative to the material by rotating the sample and detector positions about a single common rotational axis. Figure 4 shows an image and schematic of a typical system. The incident direction $\hat{\boldsymbol{\omega}}_{\boldsymbol{i}}$ is precisely adjusted by rotating a material sample stage, and the scatter direction $\hat{\boldsymbol{\omega}}_{\boldsymbol{s}}$ is adjusted by precisely rotating the detector arm. When the material surface plane is orthogonal to the plane of rotation, the CASI® collects in-plane measurements only; the material rotation stage sets θ_i, and the detector arm sweeps to various θ_s values. In this case, the detector remains within one azimuthal plane, which includes the material surface normal, and where either $\phi_s = \phi_i$ or $\phi_s = \phi_i + \pi$. If the material surface plane is not orthogonal to the plane of rotation, the detector arm becomes capable of traveling out-of-plane, but the combinations of possible (θ_s, ϕ_s) are still constrained to an individual plane, but which but no longer includes the material surface normal.

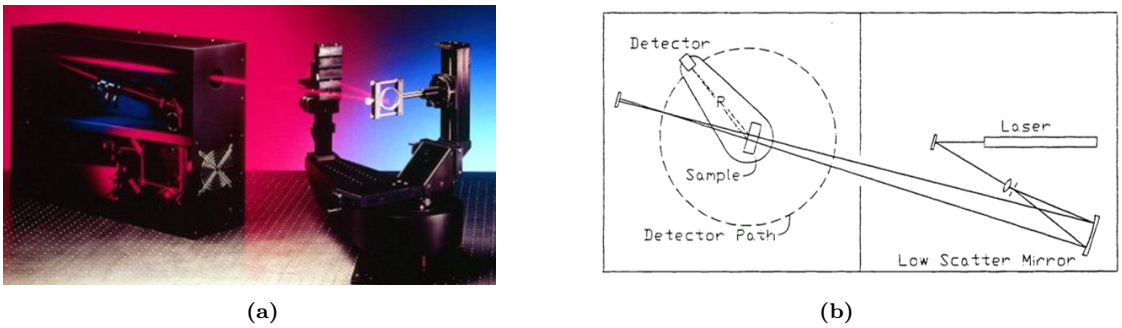

(a) (b)

Figure 4. Image (a) [68] and schematic (b) [59] of a typical CASI® setup. The optics box aligns and focuses a laser source with a fixed incident direction. The material sample stage and detector arm share a rotational axis, which most easily allow in-plane measurements for various incident angles.

As originally designed, the CASI® utilizes detectors comprised of only one detection area (pixel), and thus, flux can only be measured for one scatter direction at a time. Coupled with the complexity required to precisely tilt material surfaces, this makes out-of-plane measurements very cumbersome and impractical with the CASI®. Even when concentrating on in-plane measurements, changing azimuthal planes still requires rotating the material sample about its own normal. In reality, the traditional CASI® is really best suited for collecting in-plane measurements of isotropic materials.

In an effort to measure anisotropic BRDF data throughout the entire hemisphere, Filip mounted an incoherent light source and a camera to their own independent two-axis goniometers, so that each could be moved anywhere within the hemisphere above a fixed material surface [26]. Although able to sample the entire four-dimensional space, the angular measurement resolution along any dimension did not surpass 2°. Even once the process was established, at least 16 hours were required to collect a single material measurement [26].

Ward employed a slightly different method for collecting anisotropic measurements, using a fixed incoherent source to illuminate a fixed material sample at the center of a half-silvered hemispherical mirror [75]. The light reflected from the sam-

ple surface into all directions was then reflected by the hemispherical mirror back to a camera with a fisheye lens. Although measurement collection time was shortened significantly without the need to step through various incident and scattered angle geometries individually, the method lacked resolution sufficient for specular surfaces due to various reasons, such as imperfections in the acrylic hemisphere, incandescent source directionality, and fisheye lens aberrations [75].

Ngan and Matusik directed yet another method which involved a fixed camera, incandescent light source on a single-axis goniometer, and material samples mounted to a rotating cylinder. The material stage rotated about an axis perpendicular to its longitudinal axis, and was wrapped in multiple sample strips which were each comprised of the same material placed at various azimuthal orientations [22]. Although the cylindrical sample stage cleverly accounted for a degree of freedom without necessitating motion, not all samples can be adequately stretched and curved to wrap around the surface of a cylinder. In addition, the angular resolution of cylinder rotations were limited to 5° while the individual strips represented orientation differences of 9°.

To summarize, there is a need to further refine methods for exploring anisotropic and out-of-plane BRDF measurements with both high spatial resolution and practical time expenditures, particularly for specular materials.

Measurement Uncertainty.

As with any laboratory measurement, it is important to understand and quantify applicable uncertainties in the BRDF measurement process. Even though certain models like Beard-Maxwell attempt to reduce uncertainty by incorporating empirical measurements, Crockett also warns that quality data can be difficult to measure accurately.[19]

"Historically, round-robin measurement programs (in which a material sample is passed from laboratory to laboratory to have its BRDF measured) do not return consistent data. Between laboratories there are the usual differences between mechanical resolution, aperture size, stray light, detector noise levels, how the sample is held (stationary, spun)....Finally, there is an issue with the exact, current, real-world state of a target material surface. How old is the surface finish? Has it been changed by weather, oxidation, handling, sand-blasting, or heat? Just how valid are the measured BRDFs that we use to do the simulation modeling?"[19]

At least when it comes to uncertainty inherent in laboratory measurement setups, Cady presented a formulation for quantifying BRDF measurement uncertainty, and applied the technique specifically to the CASI®. First, he began with Equation (45) as the equation for calculating BRDF from measurable quantities. Then, by taking partial differentials with respect to each variable, he formed the total relative error

$$\frac{\Delta f_r}{f_r} = \left[\left(\frac{\Delta \Phi_s}{\Phi_s} \right)^2 + \left(\frac{\Delta \Phi_i}{\Phi_i} \right)^2 + \left(\frac{\Delta \Omega_d}{\Omega_d} \right)^2 + \left(\frac{\Delta \theta_s \sin \theta_s}{\cos \theta_s} \right)^2 \right]^{1/2}, \tag{71}$$

where each term represents the first-order linearized relative error contributed by uncertainty in each individual measured quantity, added in quadrature. Cady then goes on to write sub-expressions for each term when multiple uncertainties apply to each measurable quantity. For instance, he writes $\Omega_d = \pi r^2 / R^2$, where r is the radius of the detector's circular aperture and R is the distance from sample to detector, so that the sub-expression

$$\frac{\Delta \Omega_d}{\Omega_d} = \left[\left(\frac{2\Delta r}{r} \right)^2 + \left(\frac{2\Delta R}{R} \right)^2 \right]^{1/2} \tag{72}$$

represents the full uncertainty in detector solid angle, based on quantifiable uncertainties in the parameters r and R.

As Crockett described, in addition, there are important uncertainties to understand among material samples, which include differences between the materials measured in laboratory settings – which are used to inform radiometric models – and those measured in the field. For example, when modeling satellite material reflection, even if measurements in a laboratory setting are theoretically made with total accuracy, satellite materials are subjected to extreme environments on orbit, and the effects of space weathering on the optical properties of materials are not well understood [45, 46]. Multilayer insulation, for example, which is often present in large quantities across satellite surfaces, often shows wrinkling and anisotropic behavior after installation [20], as do milled metals and potentially solar panels [76]. In addition, the solid angles subtended by target satellites in GEO are many orders of magnitude smaller than those used in laboratory setups [45, 46]. Crockett goes on to say that when relying on reflectance measurements from pristine samples, "we are likely to overestimate the specular and underestimate the diffuse contributions" when modeling a material in a real-world situation [19].

According to Crockett's description, any remote sensing application, including satellite light curve analysis, is most certainly susceptible to several major pitfalls of BRDF modeling. In order to retain a realistic chance of solving inverse problems, the BRDFs for materials onboard real satellites must be properly understood and modeled.

2.4 Space Domain Awareness

As worldwide satellite populations, technologies, and capabilities continue to grow, the United States Air Force (USAF) and the United States Space Force (USSF) must continue to improve their abilities to detect, track, characterize, and catalogue the myriad spacecraft in orbit. These particular capabilities fall squarely within a mission

set known as Space Domain Awareness (SDA), which at its heart strives to maintain current and predictive knowledge of the space environment, ultimately in order to preserve the United States' various national interests in space [2]. As an Air Force Space Command (AFSPC) chief architect for SDA succinctly described: "You want to know more about what an object's capabilities are, what its potential uses could be, what's normal pattern of behavior versus different pattern of behavior" [7]. Despite this rather easily stated overarching premise, the actual process of distilling relatively sparse observational data from largely unknown satellites into specific and useful characteristics or attributes can be an incredibly difficult problem. In fact, some leaders have asserted that SDA "is not an exact science" based solely on technical capabilities and algorithms, but rather an art – "primarily the result of inference" – based on the combined roles of technology, intelligence, and experience [49].

One readily available source of information from satellites in orbit comes from optical radiation collected by ground-based or even space-based telescopes. In general, every satellite reflects optical radiation originating from bodies such as the Sun, Earth, and Moon, and also emits radiation based on its own thermal state. Reflected and emitted radiation can then be passively collected by detectors sensitive to the appropriate electromagnetic wavelengths. For satellites in high Earth orbit, such as those in the geosynchronous belt, optical collections are almost exclusively spatially unresolved, due to the vast distances between target and observer [15]. Once observations are collected, the task then becomes to leverage the full complement of known information to infer or back out unknown properties of the observed satellite. However, this process of inference, also known as solving the inverse problem, requires sufficient predictive knowledge of how input parameters – in this case properties such as satellite size, shape, material composition, operational status, position and orientation relative to light sources and observers, etc. – map to measurable outputs

– such as spatial, spectral, polarimetric, and time-dependent components of optical observations. In other words, solutions to the forward problem must be sufficiently characterized, along with associated uncertainties, in order to inform inferences or solutions to the inverse problem.

Satellite observations in the visible regime are predominantly comprised of reflected light, and so forward-solving the radiometric problem requires modeling satellite reflectance with sufficient accuracy. For many applications throughout both the commercial sector and the Department of Defense (DoD) which require material reflectance models, some form of appropriate BRDF is typically chosen to encapsulate the desired reflectance functionality. The complexity, utility, and diversity among published BRDF models, though, is quite vast, and due to their various underlying assumptions, none are perfectly or universally applicable. Thus, the accuracy and predictive power of any satellite radiometric simulation depends significantly on the realism of the BRDF models it uses.

Early SDA Inverse Problem.

Solving the inverse problem represents the end goal of the SDA process, whereby radiometric measurements of unknown spacecraft can be used to back out properties such as size, orbit, orientation, composition, capability, etc. For satellites in low-Earth orbit (LEO), solutions to the inverse problem are typically informed by substantially resolved data from high-powered ground-based radar and electro-optical telescopes [46]. Unfortunately, for satellites in higher orbits at much longer ranges, such as geosynchronous orbit (GEO), the inverse problem becomes much more difficult. GEO satellites are beyond the effective range of terrestrial radar, and thus solutions must instead rely almost exclusively on unresolved solar reflectance signatures collected by telescopes [34, 63, 40]. Despite the challenges, early attempts to solve the inverse

problem yielded some promising results.

In 1976, for example, Friedman of MIT's Lincoln Laboratory analyzed photometry data collected from a known rocket body flying in space, and used the data to predict a periodic gyration every 40 seconds. To prove his solution to this inverse problem, he solved the forward problem by developing a model for specular reflection from a cylindrical body, and then reproduced the same periodic glinting reflection pattern observed in the collected data. He was able to show how a misalignment of the rocket body caused a precession which periodically satisfied the geometrical requirements for specular reflection, resulting in observable glints from the ground [27]. However, sparse computational resources prevented Friedman and other early scientists from more complex analysis [46].

At about the same time as Friedman's work, scientists in the computer graphics field were investigating the importance of modeling glinting features. In particular, Phong developed an algorithm which could successfully replicate specular reflection in computer generated imagery, thereby enhancing the realism of visual features with specular characteristics. In essence, he incorporated the basic law of reflection from geometric optics into a very computationally efficient code, accounting for variables such as surface normal vectors, source illumination locations, and observer locations [53]. In his findings, Phong stressed that the quality of a computer generated image depended heavily on correctly modeling specular reflection [53]. Even though DoD scientists had been independently developing similar algorithms to handle specular reflection for use in optical designs for military equipment such as infrared seekers [50, 48], Phong's algorithm garnered special attention from SDA researchers because it offered a fast, somewhat physics-based model to describe the commonly observed glinting phenomenon in satellite radiometric measurements [50, 54].

In 1980, Posdamer borrowed Phong's algorithm and published a feasibility study

investigating the use of computers to assist in determining a satellite's geometry based solely on glinting patterns in its light curve, or intensity plot versus time. Posdamer started from the assumption that bright specular peaks were caused by flat polygonal surfaces when their normal vectors matched the bisector between the observer and illumination source (i.e., whenever the geometric law of reflection was satisfied). Theoretically, he could then identify the possible polygonal orientations and combinations which could produce a given light curve. Unfortunately, Posdamer concluded that without radiometric models which could more accurately represent reflections from various surfaces, the process did not produce a useful set of possible solutions to the inverse SDA problem [54].

Modern SDA Radiometric Modeling.

Since Posdamer's work in the 1980s on the SDA inverse problem, modern SDA researchers have focused considerable effort towards solving the SDA forward problem, in hopes of gaining better understanding for solutions to the inverse problem. However, a consistent theme has arisen from virtually every attempt to simulate and validate light intensity curves from satellite surfaces and materials. Namely, BRDFs ubiquitously struggle to accurately model the specular portions of reflection [20]. Unfortunately, the specular glints produced in satellite light curves often contain the most valuable information about the satellite's characteristics [46]. What's more, although the problem with glinting has been consistently identified, few research efforts have attempted to quantify the impact of such error when modeling GEO satellite light curves [46]. Interestingly, the computer graphics industry has independently identified the same issues when modeling realistic specular glinting phenomena in computer generated imagery for movies or video games [46].

In 2007, AFRL tested the feasibility of using the Time-Domain Analysis Simula-

tion for Advanced Tracking (TASAT), which accesses AFRL's database of empirical satellite material optical measurements, to predict the spin rate of NASA's Imager for Magnetopause-to-Aurora Global Exploration (IMAGE) satellite. Although they concluded that prediction was possible, the published study noted that TASAT's simulated light curves exaggerated the specular contributions from the satellite's booms when compared to photometry data obtained by the Advanced Maui Optical and Space Surveillance (AMOS) telescope [32].

In 2014, AFRL launched the Automated Navigation and Guidance Experiment for Local Space (ANGELS) satellite, and collected photometric data from ground-based telescopes at the United States Naval Observatory (USNO) and Kirtland Air Force Base [46]. Prior to launch, the radiometric properties of the satellite and the Delta IV upper stage rocket body were extensively measured, so that researchers could use truth data to adjust their radiometric models to match measurements from orbit. The ANGELS experiment represents the most comprehensive publicly disclosed test of satellite radiometric modeling accuracy to date [46]. Although the experiment validated the ability to discriminate among types of satellite maneuvers given a priori knowledge of satellite characteristics, the models still suffered significant errors during glints. "It seems that some features on the satellite are very specular and are not being well-described by the BRDFs..." [46]. Even a former chief scientist for the AFRL Space Vehicles Directorate stated in a paper that "The Beard-Maxwell BRDF model...used in TASAT..., while accurate for many materials, has been shown to decrease in accuracy for materials with very specular scattering" [20].

Other organizations have also worked to improve modeling for the forward SDA problem. In 2014, scientists at the University of Arizona worked with AFRL to develop a new model able to replicate light curves of known GEO satellites. However, all three of their BRDF model choices struggled to match AFRL's truth data. In

particular, the models failed to predict solar panel glints from multiple observation datasets, leading the authors to recommend future work in order to "better capture solar panel glints" [16].

In 2009, the Air Force's Advanced Missile Signature Center studied light curve patterns from basic geometric shapes like spheres and cylinders in an effort to recognize subtle changes in spacecraft characteristics. However, their models failed to realistically simulate nadir-pointing spacecraft due to "limitations...in the simulation to account for the surface material specularity" [43].

Other institutions such as Lockheed Martin, Ball Aerospace, Boeing, the Rochester Institute of Technology, and even researchers and organizations from other countries such as China, have all produced studies which have shown promise in detecting certain spacecraft characteristics and events, such as actively controlled or tumbling orientations, maneuvers, and close proximities to other satellites, but in each case, the glinting issue recurs [4, 33, 42, 74]. In summary, 40 years of attempts to accomplish detailed satellite characterization, beyond basic pattern recognition, have consistently produced unrealistic and unbounded solutions [46].

Ultimately, errors in BRDF models produce errors in solutions to the SDA forward problem, particular regarding specular glints, which in turn can easily lead to false or misleading inferences while solving the inverse problem [46]. When recalling the conservation of energy, it is also easy to see that models which either exaggerate or underestimate specular reflection very likely also underestimate or exaggerate diffuse reflection, respectively, for the same material, leading to compounding errors in simulated light curves beyond just the specular region [46].

It is important to note that although the light curve studies referenced in this section utilized various microfacet BRDF models, they each relied on the fundamental form given in Equation (51). At best, the models included a single specular term –

driven by an isotropic microfacet distribution function – along with diffuse volumetric and Lambertian factors. Sometimes, though, researchers have even used purely Lambertian models [17, 39]. Regardless, none of the models described any out-of-plane reflectance features, and none of them included any wavelength-dependent diffraction features.

Applying Flexible BRDFs to SDA.

In the entertainment industry, computer graphics designers often use very similar or even identical algorithms when computing BRDFs for scene generation purposes. Not surprisingly, they also report challenges when attempting to realistically model specular reflection in their images. In 2005, a group from MIT selected seven representative BRDFs and quantitatively identified reflection errors in every model. On average, materials with more specular properties such as metals and glossy paints demonstrated errors ten times greater than those for more diffuse materials [22]. They concluded that although empirical BRDFs offer powerful representations, the required data resolution in order to achieve modeling accuracy is very high, and often unattained [22]. Quality reflectometers are often as large as a room, and acquiring the data for a single BRDF can easily take many hours [22]. However, due to the smoothness observed in even complex empirical reflection patterns, they recommended further focus on parametric BRDFs, which offer researchers and computer graphics artists much greater flexibility in manipulating models to correct for errors [22].

The findings from MIT complement another finding from Crockett. As stated earlier, SDA researchers most commonly use the Beard-Maxwell empirical BRDF model. However, "the primary assumptions in the Beard-Maxwell BRDF model...seem to be well satisfied by most man-made machines materials with a fairly smooth finish. How-

ever...extremely rough surface finishes are not well modeled...Also, the Beard-Maxwell BRDF model cannot easily handle mirror-like finishes" [19]. Based on its underlying assumptions, and due to its inflexible empirical basis, the Beard-Maxwell BRDF may not actually represent the best model for SDA purposes [46].

In 2017, Lowery applied the concept of flexible BRDFs directly to the SDA forward problem in order to quantify the uncertainties associated with choosing different microfacet distribution functions [46]. He began by selecting two of the most commonly used BRDF models for SDA – Beard-Maxwell and Phong-Blinn – and then selected four distinct microfacet distribution functions to use within them – Beard-Maxwell, Hyper-Gaussian, Lorentzian, and Sandford-Robertson (described in Section 2.3). He set up a radiometric simulation using MATLAB and the Satellite Visualization and Signature Tool (SVST) to model solar glinting conditions for an object in GEO observed by a ground-based telescope, and generated light intensity curves for 270 different satellite materials. By comparing simulations, he was able to determine which BRDF combinations simulated the highest intensity specular reflections, which simulated the lowest intensity specular reflections, and determined overall uncertainty in terms of the greatest simulated difference [46].

After completing the analysis for each individual satellite material, Lowery then obtained computer-aided design (CAD) models for ten surrogate GEO satellites from AFRL. Using SVST's ability to alter portions of BRDF models for individual surfaces, he created three different versions of each satellite. The first version maintained the default BRDF and microfacet distribution used in typical SDA research for each satellite material. However, in the second version, he changed the BRDF model and microfacet distribution function for each individual material on the satellite to the combination which produced the highest specular reflection for that particular material, as determined from his first set of simulations. In the third version, he instead

selected the BRDF model and distribution function combination which corresponded to the lowest specular reflection for each individual material. He then ran the solar glinting simulations using the entire satellite CAD models, using ten different rotational orientation schemes for each [46].

From his simulations, Lowery offered several important conclusions. First and foremost, he showed that it was possible to quantify uncertainty in the SDA forward problem by utilizing flexible BRDF expressions in radiometric simulations. In fact, he discovered that simply changing the microfacet distribution function led to average light curve intensity differences of 93% across all ten satellite models. The uncertainty in glinting patterns for individual satellite materials was often orders of magnitude higher. He also noted that the default BRDF models and distribution functions typically used in SDA research corresponded to his highest specular reflection curves over 72% of the time, which essentially means that if researchers simply choose parameters other than the default, they are virtually guaranteed to lower their simulated specular reflection values [46].

2.5 Research Path

It is important to note here that Lowery's work produced powerful results, demonstrating the range of potential impacts to light curve analysis simply by exchanging BRDF model components which already exist. However, as described in Section 2.4, studies and efforts to reconcile light curve observations and simulations using existing BRDF models have consistently struggled to match specular glints from materials such as solar panels. In general, across the entire field of BRDF research (beyond just light curve analysis), there is a lack of specular out-of-plane material BRDF measurements with high angular resolution, and in turn, there is a lack of BRDF models capable of capturing out-of-plane behavior.

The next chapters describe work completed to design, build, and implement a novel out-of-plane BRDF measurement system to fill this gap. The device is then used to measure a satellite solar cell, capturing significant out-of-plane behavior caused by its complex anisotropic surface features, including a diffraction pattern which appears through a wide swath of scatter directions, well beyond the main specular direction. Finally the data is used to inform a new closed-form solar cell BRDF model, significantly different than those published to date. Ultimately, the updated model can be incorporated into future work investigating its impact on the aforementioned light curve disparities.

III. Out-of-Plane BRDF Measurement System

As described in Section 2.3, a gap exists in the field of BRDF measurement, which lacks a method capable of accurately and reliably capturing both in-plane and out-of-plane data surrounding material specular peaks with high angular resolution. This chapter presents a device capable of filling this gap by augmenting a traditional CASI® with a scientific-grade CCD camera. As a fundamental premise, the system utilizes the high precision motion stages and illumination source conditioning optics of the CASI® as a backbone, but mounts a multi-pixel CCD with an alignment apparatus to the detector arm. As opposed to the traditional single-pixel CASI® detectors, each CCD pixel measures flux reflected in a different scatter direction, thus capturing both in-plane and out-of-plane data simultaneously.

Constructing this system and preparing it for material BRDF measurements requires several steps, beginning with selection of an appropriate CCD compatible with the desired illumination source. Once procured, the CCD must be mounted to the CASI® detector arm, along with a combination of motion stages capable of precise alignment. After mounting, the CCD and the illumination source must be calibrated and then aligned with the source beam's incident direction. In addition, each CCD pixel must be mapped to the correct scatter coordinates. At this point, the CCD is ready to measure the illumination source beam signature (meaning the focused source beam without a material sample in place), which can be used for converting raw pixel flux measurements into BRDF values using Equation (45). The sections below work through each step of this process in detail, and conclude with a comparison of beam signature measurements between the CCD-augmented system and the CASI®'s original detector. Uncertainty analysis and material BRDF measurement results follow in Chapters IV and V.

3.1 Camera Specifications

A scientific-grade low-noise CCD camera from Thorlabs® was chosen for incorporation into AFIT's already modified version of the CASI® for emphasis with visible laser sources. The camera's 3296 × 2472 pixel focal plane array (FPA) is built by ON Semiconductor® and includes built-in microlenses with anti-reflective coatings. It utilizes silicon-based detection to produce a monochrome (single-channel) output with quantum efficiencies >10% for wavelengths between 350-810 nm and a peak quantum efficiency of ∼50% near 510 nm. The camera comes with a pre-installed but removable filter which doubles as a protective cover, and which sharply limits the incoming light to >90% transmission only between 392-695 nm, effectively blocking most light outside the visible spectrum.

Each pixel is 5.50 μm × 5.50 μm in extent, with a total imaging area of 18.13 × 13.60 mm. Without using external triggering devices, exposure times can be set anywhere between 1 ms and 1000 s in 1 ms increments. Published pixel full well capacity is listed as 20,000 electrons, but the digital output is limited to 14 bits, or readings between 0 and 16,383 digital counts. The black level offset can be set anywhere from 0 to 4095, which provides the ability to shift the digital output above signal-independent noise levels from the measurements, and the camera's software also has the ability to internally average up to 32 frames into a single frame output. This particular model (8051-USB) connects to a computer for both control and data output via USB cable.

Noise characteristics are published, but the total combination of signal-independent internal noise sources can also be characterized and validated by imaging with the lens cap on at various integration times. These noise characteristics can then be used to quantify signal-to-noise ratio (SNR) and pixel uniformity at various conditions. As a demonstration, one average over 32 frames with the lens cap on, 1 ms exposure

time, and the default black level offset of 54, yielded an image with a mean pixel reading of 29.29 digital counts and a standard deviation of 2.14 counts, while the same case with exposures of 15 ms produced a mean pixel reading of 29.62 digital counts and a standard deviation of 11.21 counts. Noise characteristics are discussed in further detail as part of the uncertainty analysis in Section 4.2.

3.2 Mounting to the CASI®

A significant portion of initial work involves designing a method for physically mounting the CCD to the existing CASI® structure with an apparatus capable of precisely aligning the camera with the source beam. The camera – along with an additional Thorlabs® photodiode power meter calibrated to NIST specifications – is physically mounted to the CASI® detector arm approximately 30-35 cm from the sample. This location allows the original detector mount to remain 50 cm from the sample, while still attempting to leave room for additional optics in front of both sensors, including the rotating waveplate and polarizer necessary for dual rotating retarder (DRR) measurements [72]. In order to achieve proper alignment with the source beam, the camera requires finely resolved translational and rotational motion achieved through a combination of mechanical devices. Figures 5-7 provide images of the final mounting setup.

Starting at the bottom and working upwards, the first device mounted to the CASI® detector arm is a motorized 150 mm linear translation stage (LTS150) built by Thorlabs®, which can be controlled via USB connection by the same computer used to control the camera. It achieves calibrated absolute accuracy better than 5 μm – less than the size of one pixel – and it is mounted perpendicular to the detector arm's radial direction, labeled the x-axis or in-plane direction. The primary purpose of this stage is to provide easy switching between the camera, power meter, and

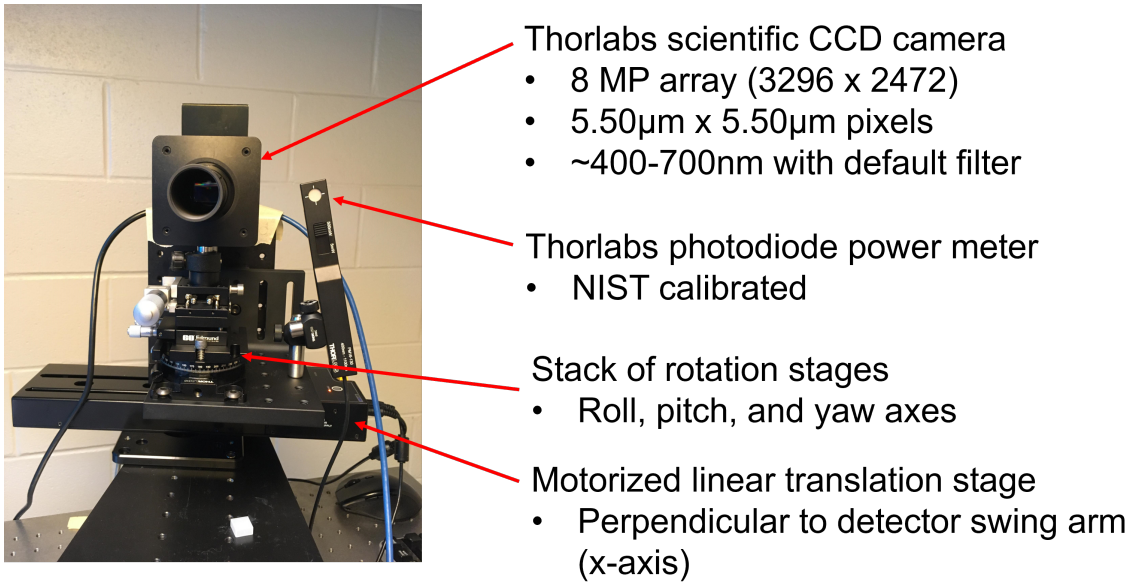

Figure 5. CCD mounting setup: front view

original CASI® detectors. The camera and power meter can be moved horizontally out of the source beam path to allow use of the original detector, or they can each be quickly and accurately centered on the beam as desired.

Directly atop the LTS sits a 90 degree bracket with a manual micrometer-driven linear translation stage mounted for motion along the vertical direction, labeled the y-axis or out-of-plane direction. This stage in turn supports another 90 degree bracket with a mounting surface normal to the vertical. The camera and the power meter, along with the rest of their respective mounts and stages, rest atop this surface. The vertical translation stage is limited to 1 inch of travel, but various mounting locations on the bracket allow for coarse alignment within 1 inch of the beam height, so that fine manual alignment can be used to accurately center the camera and power meter vertically onto the beam path.

The next two camera mounts are rotation stages. The bottom rotation stage is a Thorlabs® PR01, and atop that sits an Edmund Optics TechSpec® Tip-Tilt Stage.

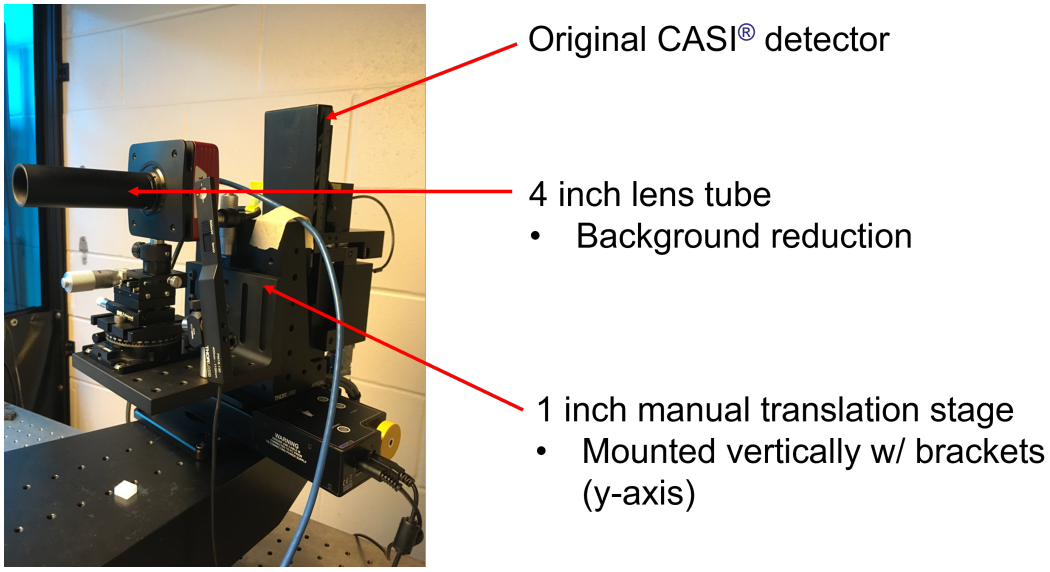

Figure 6. CCD mounting setup: side view

The PR01 rotates to provide yaw control, while the tip-tilt stage provides pitch and roll control. Combined, the two stages provide manual but precise control of all three degrees of rotational freedom.

The final stage beneath the camera but atop the rotation stages is a small micrometer-driven linear translation stage. This stage can translate the camera forward 1 inch along its optical axis (the direction in which it is pointing). This stage is utilized for assessing yaw and pitch misalignment, discussed further in Section 3.4.

Lastly, the power meter is attached to a locking swivel mount located beside the camera mount, so that its 9.5 mm diameter aperture can be manually aligned with the source beam separately.

3.3 Calibration

After mounting, several calibration steps are required to prepare the CCD for measurements. This work uses a 15 mW red helium neon (HeNe) laser source with 632.8 nm wavelength, although the same process could be implemented with other

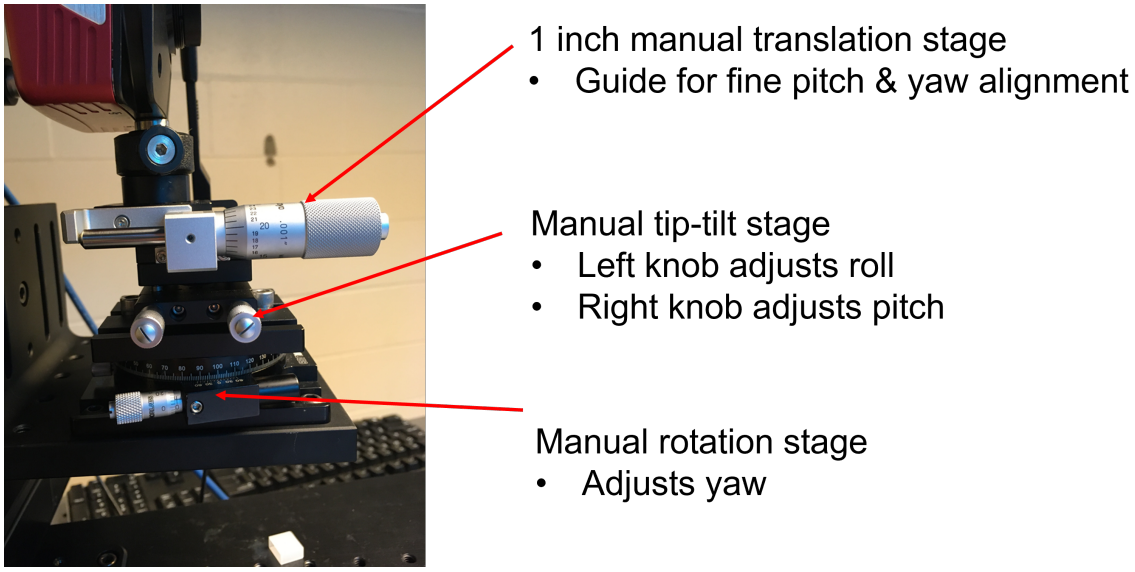

Figure 7. CCD mounting setup: rotation stages

sources with different power levels or wavelengths.

Power Meter.

Unlike the CASI®, the camera is not calibrated to measure power in Watts. Theoretically, absolute BRDF can be calculated using any power units, such as digital counts per second, because the scatter power units cancel with the incident power units in the calculation given by Equation (45). However, having some convenient method to measure power in Watts is still desirable because certain specifications such as source laser outputs, neutral density (ND) filter limitations, etc., are typically reported in Watts. The CASI®'s power reading could theoretically provide the baseline, but the CASI® detector is located farther away from the sample than the camera, which would require more frequent beam refocusing. Also, without knowing the accuracy of the CASI® calibration to Watts, the NIST-calibrated compact power meter can be used to measure the total beam power when needed. The installed power meter can detect 500 pW to 5 mW at 100 pW resolution, and 5 mW to 500

mW at 10 nW resolution, responds to wavelengths between 400 and 1100 nm, and plugs directly into a computer via USB for control and display.

Pixel and Array Angular Extents.

Unlike single-pixel detectors, the FPA can accomplish a beam signature measurement from a single position without moving the detector arm, providing high spatial resolution in both the in-plane and out-of-plane directions. Since the array and pixel sizes are fixed, the angular ranges and resolutions are determined by the distance between the sample and camera. For instance, for this work the camera was mounted 30.7 ± 0.2 cm from the sample, and the published FPA location is somewhere between 16.6 and 18.7 mm from the camera front [69]. By taking into account these range of values, the center pixel subtends $(9.70 \pm 0.09) \times 10^{-4}$ linear degrees in both the in-plane and out-of-plane directions, and $(2.86 \pm 0.06) \times 10^{-10}$ sr, while the full array subtends (3.19 by 2.40) ± 0.03 linear degrees and $(2.34 \pm 0.05) \times 10^{-3}$ sr. Since the array is flat, the in-plane and out-of-plane angles subtended by each pixel are not necessarily constant across the array. However, for a sample-to-camera distance on the order of 30 cm, whose square is much larger than both the area of the array and the area of the sample spot size, the maximum difference in angular extent among pixels is only approximately 1×10^{-6} deg and 2×10^{-13} sr. More detailed scatter coordinate angle calculations for each pixel are given in Section 3.5, with a more complete uncertainty analysis given in Chapter IV.

Depending on the application and desired results, the camera can be mounted with its longer axis in either the horizontal (in-plane) or vertical (out-of-plane) direction. Table 2 summarizes the linear angles and solid angles, including known precision, assuming that the FPA long axis is aligned with the in-plane direction, which was the orientation chosen for this work.

Table 2. Linear and solid angles subtended by the center pixel and by the entire FPA when mounted 30.7 cm from the sample stage. In this case, the long axis is aligned with the in-plane direction and the short axis is aligned with the out-of-plane direction. θ_x and θ_y represent linear angles subtended in the in-plane and out-of-plane directions, respectively, while $\Delta\theta$ and $\Delta\Omega_d$ represent the first-order uncertainties based on camera and FPA distance from the sample stage. Linear angles values are given in degrees, and solid angle values are given in steradians.

	$\boldsymbol{\theta_x}$ (°)	$\boldsymbol{\theta_y}$ (°)	$\boldsymbol{\Delta\theta}$ (°)	$\boldsymbol{\Omega_d}$ (sr)	$\boldsymbol{\Delta\Omega_d}$ (sr)
Pixel	9.70×10^{-4}	9.70×10^{-4}	$\pm 0.09 \times 10^{-4}$	2.86×10^{-10}	$\pm 0.06 \times 10^{-10}$
Array	3.19	2.40	± 0.03	2.34×10^{-3}	$\pm 0.05 \times 10^{-3}$

Beam Attenuation.

The power of the source beam must be adjustable in order to maximize the SNR without saturating the pixels. The first important boundary case is the beam signature, which represents the strongest possible raw signal per pixel, because the unimpeded source is focused to a minimum spot size at the FPA with no sample in place. This case is important for two reasons. First, Thorlabs® and ON Semiconductor® have not published laser damage threshold data for this FPA, and focusing a laser beam to a small spot can run the risk of damaging the FPA. Second, when pixels are saturated, measurements become invalid, because all that can be known is that the maximum value has been exceeded. In practice, FPAs are built with safety margins, so it should be safe to assume that saturation limits are reached at lower powers than damage limitations. Thus, it can be assumed that for a given incident beam, as long as all pixels remain unsaturated at the camera's fastest exposure time (1 ms), then no design or damage limitations have been exceeded.

In order to ensure that no pixels are saturated for a beam signature measurement, the required beam attenuation must first be estimated and confirmed. The estimate requires knowledge of the total power contained in the unattenuated beam, the power required to saturate each pixel with 1 ms exposure, and the size of the focused spot

on the FPA.

The total power P_u contained in the entire unattenuated beam can be measured by conducting a total signal reading with the power meter or original CASI® detector.

The size of the focused beam spot can be estimated by calculating beam parameters for the laser source, deriving transfer matrices for the CASI® setup including variable spatial filter location, and then applying the ABCD law [73] as required.

The power required to saturate an individual pixel with 1 ms exposure can be discovered by first de-focusing the unattenuated beam, and then slowly re-focusing onto the FPA until the center pixels begin to saturate. At this saturation point, the average beamwidth $w = 1/e^2$ can be extracted from the CCD image numerically, and then a fitting algorithm can be run using the two-dimensional symmetric Gaussian

$$G(x, y) = A \exp\left[\frac{-2(x^2 + y^2)}{w^2}\right] \tag{73}$$

to solve for the remaining parameter A. The calculated Gaussian fit represents the irradiance distribution (power per pixel area). If the peak power given by the amplitude A is assumed constant over the center pixel, then A represents the power required to saturate an individual pixel. Putting the pieces together, the total allowable power P_a within the entire focused source beam at the saturation limit for the center pixel can be approximated by integrating another Gaussian function with amplitude A and whose beamwidth corresponds to the minimum estimated beamwidth.

Finally, the optical density (OD) required to attenuate the total unimpeded beam signature power can be found by calculating

$$\mathrm{OD}_b = \log_{10} \frac{P_a}{P_u}. \tag{74}$$

Using published parameters for a similar 15 mW red HeNe source laser, CASI® optical

train parameters, and measured camera distance from sample, the calculations yield an estimated OD_b of 5.

To attenuate the beam and validate the estimated saturation limit, neutral density filters were placed after the CASI® reference detector but before the spatial filter, as shown in Figure 8. Beginning with a de-focused beam an OD of 5, the beam was gradually focused onto the FPA. Slightly before full focus, the central pixels began to saturate, so the OD was increased to 5.2. At this point, the pixels never saturated when the beam was fully focused on the FPA.

Background Signal Suppression.

In its current configuration, the CCD lacks access to several background reduction features designed to help the original detectors operate near their inherent noise limits.

For instance, the CCD is not integrated with the chopper wheel and lock-in amplifiers used by the original detectors to suppress contributions from ambient light sources in the room [56]. Across the UV-visible-NIR wavelengths sensed by the CCD, negligible radiation results from self-emission, but light emitted from other sources in the room does reflect off various surfaces and ultimately reaches the detector. Since the CCD is sensitive across the visible spectrum, room lights must be turned off or minimized to reduce background signal, especially as exposure time increases, although certain lights such as computer screens cannot always be sacrificed.

Also, unlike the original detectors, no additional lens is placed in front of the CCD. The original detectors use a lens which constrains the field of view onto the material sample, thus reducing susceptibility to other background signals in the room, such as diffuse laser reflection from imperfect mirrors on the optical table. Lenses work for single-pixel detectors on the CASI® because they only measure flux in one scatter direction at a time. If a lens were placed in front of the CCD, each pixel

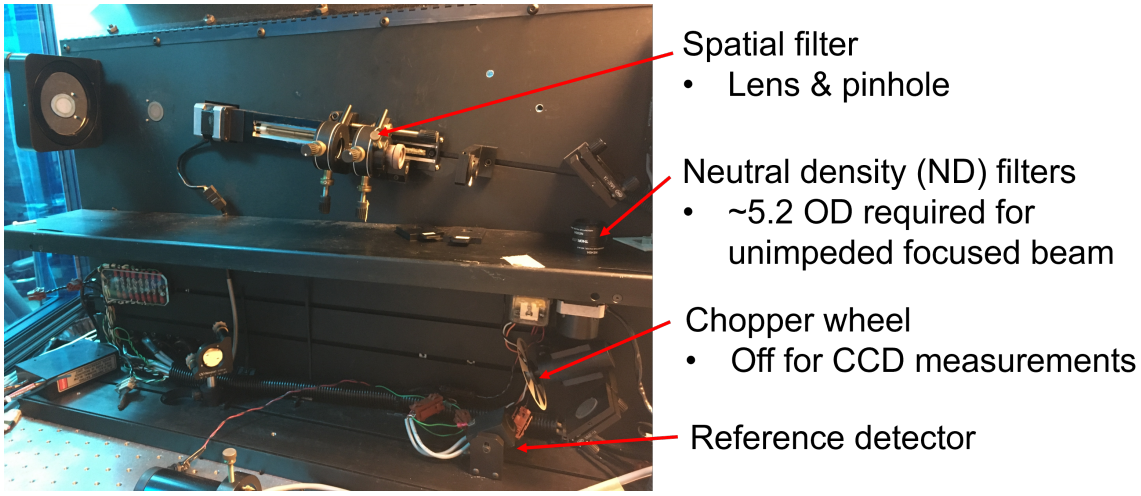

Figure 8. ND filters are placed after the CASI® reference detector but prior to the spatial filter when beam attentuation is necessary. An OD_b of 5.2 is required for unsaturated beam signature measurements at 1 ms exposure.

would have an independent field of view, meaning each pixel would instead measure the flux reflected from a different location on the material sample, essentially imaging the material instead of measuring its BRDF. The lack of a lens allows each pixel in a single frame to measure the flux reflected into a unique scatter direction from a common illumination spot. However, without a lens, the pixel fields of view are constrained only by the camera aperture. When possible, physically blocking the camera's view of the laser path assists in reducing background interference.

In addition to reducing ambient light sources and blocking the camera's view of the laser path, mounting an empty lens tube to the front of the camera provided another successful means of background suppression. This work incorporated a 4 inch tube, which drastically reduced the possible solid angles from which stray light in the room can enter the detector, but fully received reflected signals from the sample. The tube's improvement was especially pronounced for longer integration times, and when the CCD was centered on the specular peak, the tube did not contribute negative impacts to the measurements. It is important to note, however, that when the detector arm

was slewed such that the specular peak intercepted the interior of the tube, the tube's grooved internal threads reflected significant unwanted diffraction artifacts back onto the CCD, corrupting the measurement. Fortunately, this work focuses solely on measurements centered on the specular direction, leaving a remedy for this particular degradation as future work.

One unsuccessful method for limiting stray room light involved mounting a narrow band-pass filter inside the lens tube in front of the camera. However, during testing with a 10 nm full width half maximum (FWHM) filter centered on the red HeNe laser wavelength, preliminary measurements contained unwanted diffraction artifacts. Even after careful cleaning of the filter, the diffraction artifacts only disappeared once the filter was removed, as shown in Figure 9. The original CASI® detectors incorporate band-pass filters [56], but since they consist of single pixels measuring only one scatter direction at a time, any similar artifacts would not register across different spatial directions. Sensitivity to an imperfectly clean surface thus represents a limitation to using a laser line filter for background signal reduction, and so the filter was removed for the remainder of this work.

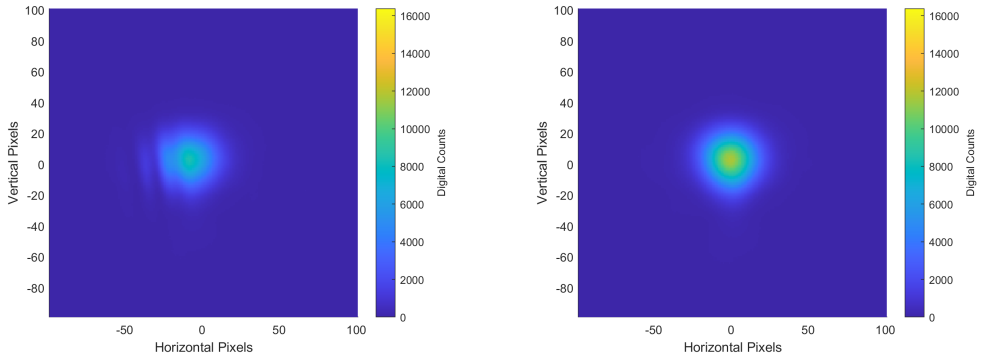

Figure 9. Demonstration of unwanted bandpass filter diffraction effects with imperfect cleaning. Both images represent measurements of the fully focused beam, using the center 200 x 200 pixels with 1 ms exposure. Noticeable diffraction artifacts are evident in (a) with the bandpass filter in place, but those features are eliminated in (b) when the bandpass filter was removed.

Further discussion of the CCD-augmented system's noise limits including background reduction techniques is found in Section 4.2.

3.4 Alignment

With the camera fully mounted and the source beam sufficiently attenuated, camera alignment can be accomplished by making adjustments while viewing the camera output in continuous frame mode on the computer. The LTS150 and vertical translation stages can be adjusted to center the FPA on the source beam rather easily.

Focus.

Spatial filter positioning can be adjusted to ensure that the beam is fully focused and symmetric on the FPA. Beam symmetry and focus are part of the original CASI® alignment too, but without the FPA, they can only be easily verified and evaluated in-plane. Figure 10 demonstrates what beam focus adjustment looks like using a 1 ms exposure. Progressing from left to right, as the CASI® beam focus parameter is adjusted, the beam symmetry changes. Although one-dimensional in-plane slices through (a) and (c) would each appear symmetric on their own, those beams are clearly asymmetric in two-dimensions. The two-dimensional cross-section provided by the CCD allows us to ensure that the incident beam is as close to TEM_{00} mode as possible. In addition, because the CCD pixel size is small relative to the focused beam spot size, the peak power increases as focus improves, as indicated by the colorbar scales in Figure 10.

Roll.

Rotational alignment requires a bit more creativity. The roll axis can be aligned by moving the CASI® detector arm and sweeping the CCD all the way across the

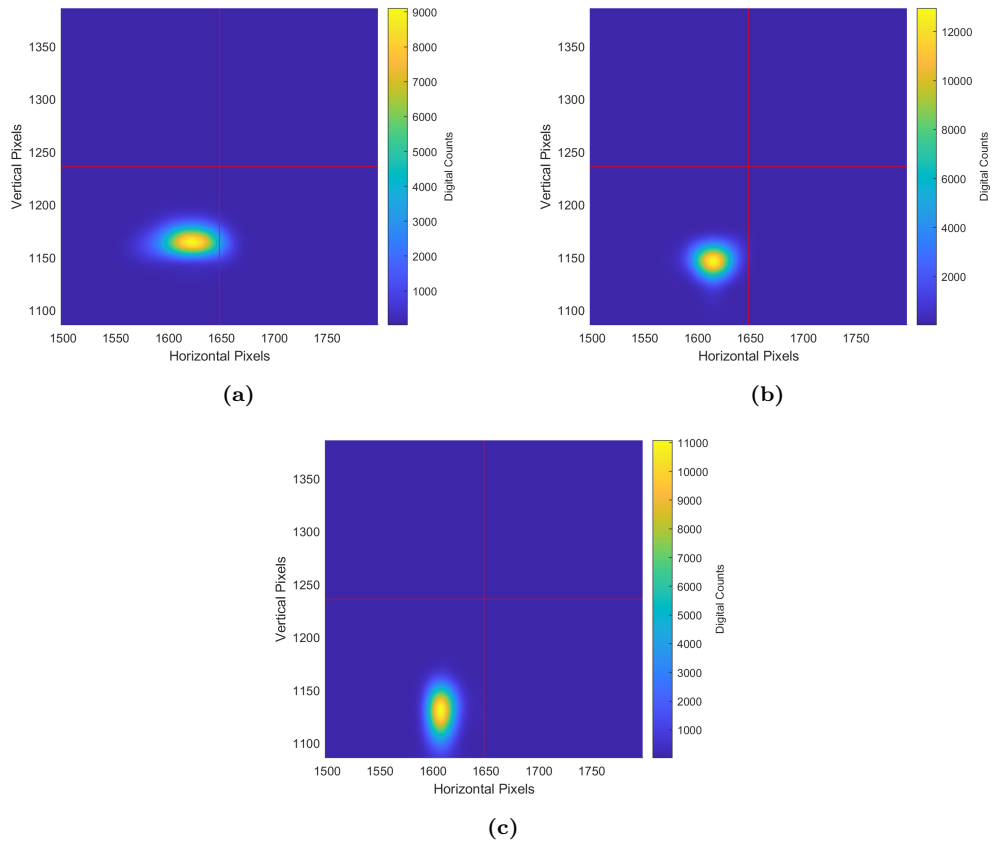

Figure 10. Examples of beam focus adjustment using the CCD with 1 ms exposure, central 300x300 pixels, and 10 frame averages. As the spatial filter location is adjusted, the beam spot starts with two-dimensional asymmetry and peak power near 9000 digital counts in (a), progresses to symmetric with peak power above 12,000 digital counts in (b), and back to asymmetric with peak power near 11,000 digital counts in (c). The spatial filter location varied by 0.50 mm between each image sequentially.

beam. If the roll axis is misaligned, the beam will display at a different vertical pixel location at each edge of the camera. Of the three rotational axes, roll may be most important because it aligns the CCD with the detector arm's plane of motion, which in turn aligns the CCD's central horizontal row with the plane of incidence. When the detector arm is slewed to collect off-specular CCD measurements in the future, images will require stitching, which will be much easier when the CCD orientation is aligned properly.

The roll alignment process has been tested and validated, with an example ad-

justment shown in Figure 11. First, the focused beam spot was centered on the FPA, as shown in (a). When the CASI® detector arm was slewed 1.5°, the beam spot center shifted 1,545 pixels horizontally and 24 pixels vertically, as shown in (b), representing a roll misalignment of $\tan^{-1}(24/1545) = 0.89°$. The tip-tilt stage was used to apply a correction, the detector arm was slewed back to zero, and the beam spot re-centered on the FPA. When the detector arm was slewed once more by 1.5°, the beam spot center only shifted 3 pixels vertically, representing an roll misalignment of $\tan^{-1}(24/1545) = 0.11°$. Thus, with only one correction, the roll alignment was improved by almost an order of magnitude.

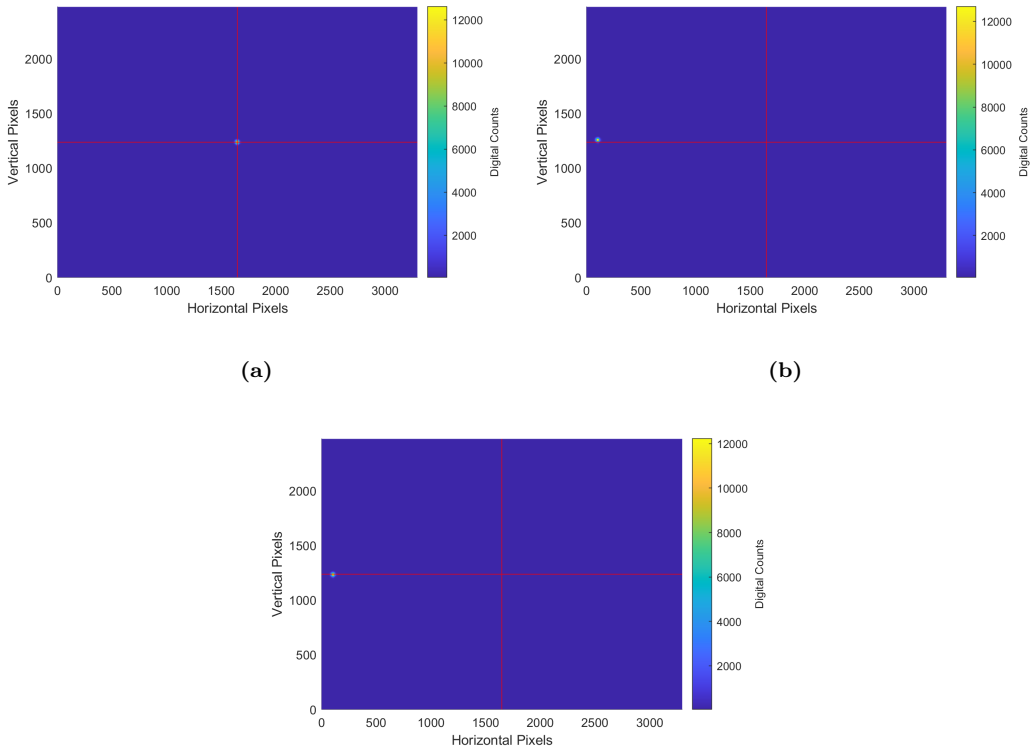

(a) **(b)**

(c)

Figure 11. Examples of CCD roll axis alignment images, using 1 ms exposure and full 10 frame averages. Red lines denote central pixel row and column on CCD. (a) demonstrates the detector arm and CCD centered on the beam. (b) shows the spot shift when the detector arm is slewed -1.5° prior to roll adjustment. (c) demonstrates the slewed position after one roll adjustment and recentering.

Pitch and Yaw.

Pitch and yaw alignment can be accomplished by merging two methods. With visible source beams, the first method involves mounting a mirror in a lens tube and reflecting the beam away from the camera. By lining up the reflected beam with the original spot on the final mirror in the CASI®'s optical train, the camera's pitch and yaw can be coarsely aligned. The second method requires mounting a manual linear translation stage atop the rotation stages, which can move the camera in the direction in which it is pointing. If the pitch and yaw are misaligned, the translation should cause the displayed beam center on the FPA to move a discernible amount which corresponds directly to the angular misalignment.

The precision of the mirror method depends upon how closely the laser spot centers can be lined up visually, and Figure 12 shows an example of the process. The translation method is more precise, and Figure 13 shows an example of fine adjustment following a coarse alignment. The focused beam was first centered on the FPA, as shown in (a). The linear translation stage was advanced 1 inch, and the beam center shifted 46 pixels horizontally and 12 pixels vertically, as shown in (b). Since 4618.2 pixels are in 1 inch, this shift corresponded to a yaw misalignment of $\tan^{-1}(46/4618.2) = 0.57°$ and a pitch misalignment of $\tan^{-1}(12/4618.2) = 0.15°$. The tip-tilt and rotation stages were used to apply corrections, and the beam spot was recentered. When the translation stage was moved back 1 inch to its original position, the spot center shifted only 5 pixels horizontally and 2 vertically, as shown in (c), which corresponded to yaw misalignment of $\tan^{-1}(5/4618.2) = 0.062°$ yaw and pitch misalignment of $\tan^{-1}(2/4618.2)0.025°$. Thus, with only one iteration, the pitch and yaw alignments were improved by nearly an order of magnitude.

The measured rotational misalignment approximations are included in Chapter IV as part of the system's uncertainty analysis.

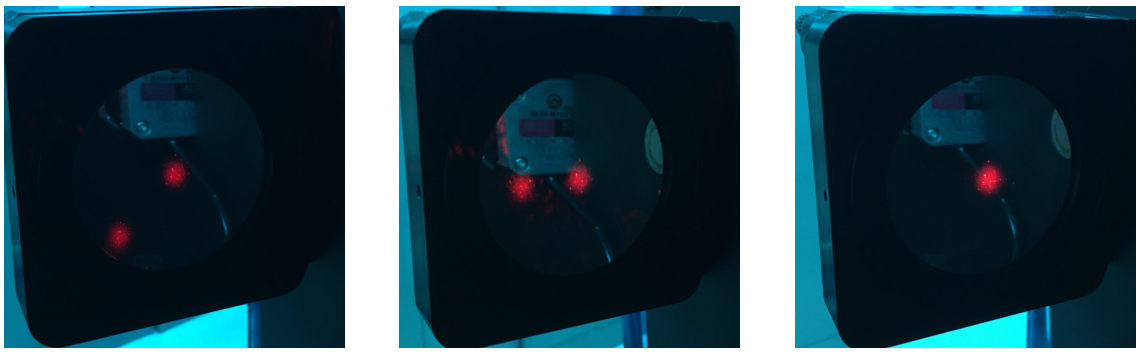

(a) (b) (c)

Figure 12. Examples of CCD pitch and yaw axis coarse alignment utilizing a CCD lens tube mirror. (a) demonstrates an initial misaligned case, where the reflection from the misaligned CCD does not align with the original spot location. (b) shows coarse pitch adjustment, and (c) shows coarse yaw adjustment, ultimately lining up the two spots visually.

3.5 Mapping CCD Pixel Scatter Coordinates

For any single CCD measurement frame, each pixel on the CCD maps to a unique scatter direction $\hat{\boldsymbol{\omega}}_{\boldsymbol{s}}$, which can be derived directly from the geometry of the augmented CASI® setup and the quality of alignment. For now, though, an assumption of perfect alignment will be made, leaving the effects of imperfect alignment for the system uncertainty investigation in Chapter IV. Assuming both the CCD and material surfaces are flat, it is natural to formulate the pixel locations first in Cartesian coordinates, and then convert to spherical coordinates as necessary.

Cartesian Scatter Coordinate System.

The first step is to define the scatter coordinate system, such as the $(\hat{x}, \hat{y}, \hat{z})$ coordinate system shown in Figure 14, which aligns with the scatter hemisphere "above" the material surface. The origin is placed at the center of the illumination spot on the surface of the material sample, depicted as a gray square. The $+\hat{x}$ direction points along the material surface within the plane of incidence (in-plane) which coincides with the CASI® detector arm's plane of motion; the $+\hat{y}$ direction points downward

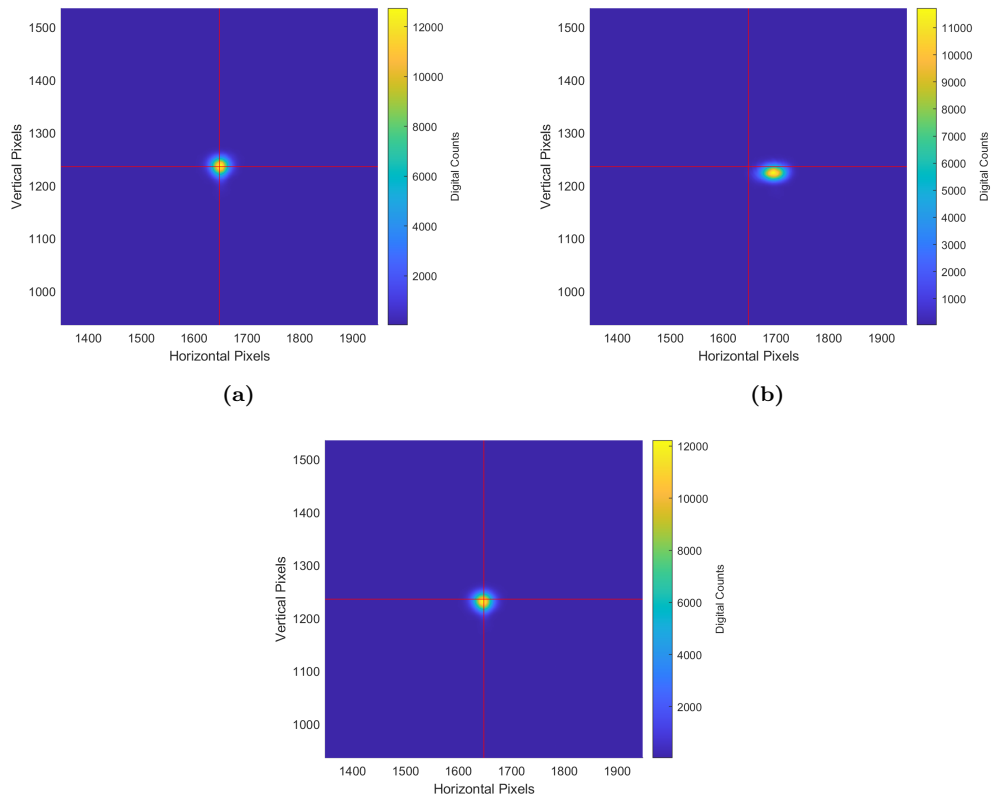

Figure 13. Examples of CCD pitch and yaw axis fine alignment with 1ms exposure, middle 600x600 pixels, and 10 frame averages, utilizing linear translation stage with 1 inch travel atop the rotational alignment stages. (a) demonstrates an initial coarsely aligned case with the beam centered on the CCD and the translation stage at zero travel. (b) shows the spot location after fully advancing the translation stage, and (c) shows the spot location after adjusting pitch and yaw axes, recentering the beam, and then moving the translation stage back 1 inch.

along the material surface perpendicular to the plane of incidence (out-of-plane); and the $+\hat{z}$ direction coincides with the material's macrosurface normal vector in order to make a right-handed coordinate system.

Under illumination at normal incidence, the $+\hat{z}$ direction aligns with the incident direction $\hat{\boldsymbol{\omega}}_{\boldsymbol{i}}$. Assuming perfect material sample alignment, the CASI® sample stage rotates about the $\hat{y}$ axis. During sample rotation, the scatter hemisphere and the $(\hat{x}, \hat{y}, \hat{z})$ coordinate system remain fixed relative to the material surface; the surface normal vector and $+\hat{z}$ direction rotate away from the CASI's® fixed source beam

within the plane of incidence ($\hat{x}$-$\hat{z}$ plane). As long as the sample stage rotation remains $\leq 90°$ from normal incidence, $\hat{\boldsymbol{\omega}}_{\boldsymbol{i}}$ remains within the scatter hemisphere.

The CCD pixel locations for any measurement can then be described in terms of these $(\hat{x}, \hat{y}, \hat{z})$ scatter coordinates by successively taking into account CCD pixel index, the CCD's mounting location a distance R from the sample, and the detector arm's in-plane location θ_c. Afterwards, the Cartesian coordinates can be converted to spherical coordinates. In Figure 14, the red dot illustrates the mapping geometry for one example pixel. The gray square represents the material sample, and the grid represents the CCD's array of pixels, which is also projected onto the material surface plane. The spherical coordinates are described in Section 3.5.

Pixel Indexing Scheme.

In order to describe the CCD pixel locations relative to one another, one of its four central pixels is temporarily placed exactly at the $(\hat{x}, \hat{y}, \hat{z})$ origin, with the pixel rows and columns perfectly aligned with the $\hat{x}$ and $\hat{y}$ axes, respectively. The $\hat{z}$ axis then points perfectly normal to the CCD surface. A pixel indexing scheme (n_h, n_v) is defined such that the desired central pixel is denoted $(0, 0)$, and the horizontal and vertical pixel index values increase according to the same directional convention as the $\hat{x}$ and $\hat{y}$ axes, respectively. For instance, when using the 1648th horizontal pixel from the left and 1236th vertical pixel from the top as the central pixel for alignment purposes, the top left pixel index becomes $(-1647, -1235)$ and the bottom right pixel index becomes $(1648, 1236)$. Thus, the vectors describing each pixel location relative to the center of the CCD can be written

$$\vec{\boldsymbol{r}}_{\boldsymbol{p}} = \begin{bmatrix} n_h d_h \\ n_v d_v \\ 0 \end{bmatrix}, \tag{75}$$

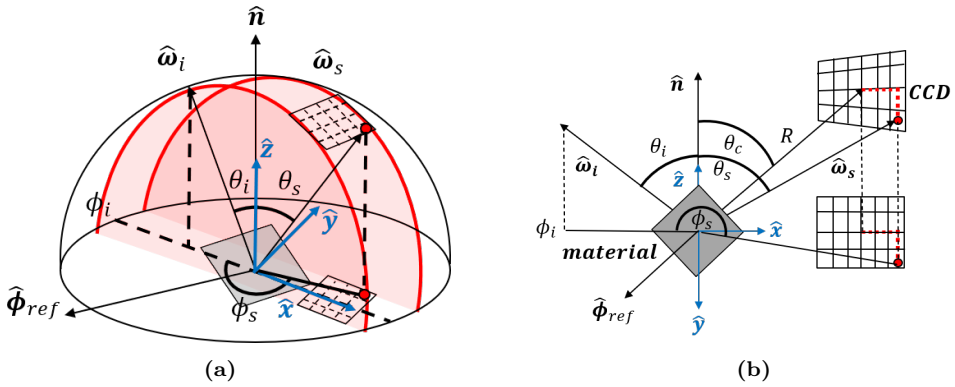

Figure 14. Illustrations of the chosen scatter coordinate definitions from two different perspectives. Both depict the Cartesian coordinate system axes $(\hat{x}, \hat{y}, \hat{z})$, along with their spherical coordinate counterparts (θ, ϕ), each relative to the material surface (gray square). Both also illustrate a projection of the CCD onto the plane of the material surface, which is particularly relevant for ϕ_s visualization and calculation.

where d_h and d_v are the horizontal and vertical dimensions of each individual pixel.

Pixel Scatter Coordinates with Perfect Alignment.

The mounted distance between the CCD and the material sample can be incorporated by adding R to the $\hat{z}$ component of each pixel vector. Then, a single rotation θ_c about the $\hat{y}$ axis accounts for in-plane detector arm location, where θ_c is measured relative to the normal incidence direction, or $\hat{z}$ axis. The vectors for each pixel can now be written in Cartesian scatter coordinates simply as

$$\vec{\boldsymbol{r}}_{\boldsymbol{s}} = \mathbb{R}_y(\theta_c) \left(\vec{\boldsymbol{r}}_{\boldsymbol{p}} + \begin{bmatrix} 0 \\ 0 \\ R \end{bmatrix} \right). \tag{76}$$

When the rotation $\mathbb{R}_y(\theta_c)$ is replaced with its matrix form

$$\mathbb{R}_y(\theta_c) = \begin{bmatrix} \cos\theta_c & 0 & \sin\theta_c \\ 0 & 1 & 0 \\ -\sin\theta_c & 0 & \cos\theta_c \end{bmatrix}, \tag{77}$$

Equation (76) can be expanded into

$$\vec{\boldsymbol{r}}_{\boldsymbol{s}} = \begin{bmatrix} n_h d_h \cos\theta_c + R\sin\theta_c \\ n_v d_v \\ R\cos\theta_c - n_h d_h \sin\theta_c \end{bmatrix}, \tag{78}$$

which describes the location of the center of each pixel relative to the center of the illumination spot on the sample material, using pixel index and θ_c as inputs, and assuming no CCD misalignment.

Equation (78) can be verified logically by thinking through what happens as the detector arm rotates the CCD from $\theta_c = 0$ to $\theta_c = 90°$. First of all, with no misalignment, the $\hat{y}$ component for any pixel never depends on θ_c; this makes sense because the detector arm rotation is modeled as a purely in-plane rotation about the $\hat{y}$ axis. At normal incidence when $\theta_c = 0$, the $\hat{x}$ component for each pixel reduces to the horizontal pixel indexing scheme $n_h d_h$, and the $\hat{z}$ component for every pixel reduces to the mounting distance R. Conversely, at $\theta_c = 90°$, the $\hat{x}$ component for every pixel reduces to R, and the $\hat{z}$ component for each pixel reduces to the horizontal pixel indexing scheme $-n_h d_h$. The negative sign correctly shows that pixels "left" of the CCD center, which have negative horizontal index values, would have positive $\hat{z}$ components at this angle.

For θ_c angles between 0 and 90°, the $\hat{x}$ and $\hat{z}$ components are comprised of appropriately scaled versions of both the horizontal pixel index and mounting distance.

Within the $\hat{x}$ component, as θ_c increases, the horizontal pixel index projection term becomes less prominent while the mounting distance projection term becomes more prominent. Conversely, within the $\hat{z}$ component, the horizontal pixel index projection term grows more significant while the mounting distance projection term grows less significant. It may also be helpful to consider the central pixel by itself, for which $n_h = 0$. For this pixel, the $\hat{x}$ and $\hat{z}$ components do not depend on pixel index at all; they depend only on mounting distance and detector arm location, scaling as $R\sin\theta_c$ and $R\cos\theta_c$, respectively. Thus, for any given detector arm location, shifting to pixels on the CCD with different horizontal index values amounts to scaled translations in the $\hat{x}$ and $\hat{z}$ directions.

Of course, the Cartesian pixel scatter coordinate vector $\vec{\boldsymbol{r}}_{\boldsymbol{s}}$ is not normalized as written in Equation (78), which simply requires dividing by the magnitude

$$|\vec{\boldsymbol{r}}_{\boldsymbol{s}}| = \sqrt{n_h^2 d_h^2 + n_v^2 d_v^2 + R^2}. \tag{79}$$

As expected, $|\vec{\boldsymbol{r}}_{\boldsymbol{s}}|$ does not vary for any detector arm location θ_c.

Conversion to Spherical Coordinates.

The conversion from Cartesian to spherical coordinates follows standard conventions except for a choice to measure azimuthal angle relative to the $-\hat{x}$ direction rather than the $+\hat{x}$ direction. This convention does not change the calculation for θ_s, but does require adding π to the calculation of ϕ_s, since standard trigonometric functions are based on angles relative to the $+\hat{x}$ axis. As a result, the spherical scatter

coordinates for each pixel can be written

$$\theta_s = \cos^{-1}\left(\frac{\vec{\boldsymbol{r}}_{\boldsymbol{s}} \cdot \hat{\boldsymbol{z}}}{|\vec{\boldsymbol{r}}_{\boldsymbol{s}}|}\right) \qquad = \cos^{-1}\left(\frac{R\cos\theta_c - n_h d_h \sin\theta_c}{\sqrt{n_h^2 d_h^2 + n_v^2 d_v^2 + R^2}}\right) \tag{80a}$$

$$\phi_s = \tan^{-1}\left(\frac{\vec{\boldsymbol{r}}_{\boldsymbol{s}} \cdot \hat{\boldsymbol{y}}}{\vec{\boldsymbol{r}}_{\boldsymbol{s}} \cdot \hat{\boldsymbol{x}}}\right) + \pi = \tan^{-1}\left(\frac{n_v d_v}{n_h d_h \cos\theta_c + R\sin\theta_c}\right) + \pi, \tag{80b}$$

where the $\tan^{-1}$ function must distinguish among all four quadrants (such as the `atan2` function in MATLAB®). Equations (80a) and (80b) provide the means to map each pixel to spherical scatter coordinates (θ_s, ϕ_s), simply using parameters from the geometry of the augmented CASI® setup for a given measurement.

It is also worth noting that in this convention, $\phi_i = 0$ by default, since the CASI®'s source beam is aligned such that the $\hat{x}$-$\hat{z}$ plane is the plane of incidence. However, after calculating ϕ_s using Equation (80b), it is possible to account for differences in material orientation about its own normal (z axis) by defining a reference direction $\hat{\boldsymbol{\phi}}_{\text{ref}}$ along the material surface. Both ϕ_i and ϕ_s can then be adjusted as necessary according to the angular offset between $\hat{\boldsymbol{\phi}}_{\text{ref}}$ and the plane of incidence. Figure 14 includes an illustration of these spherical scatter coordinates relative to the material surface and Cartesian coordinate axes.

Contours of Constant θ_s and ϕ_s.

Now that each pixel within a given frame can be mapped to θ_s and ϕ_s in terms of measurement geometry parameters, it can also be useful to understand how θ_s and ϕ_s change across a given frame. The Cartesian scatter coordinates for each pixel are already expressed in Equation (78) in terms of measurement geometry parameters –

R, d_h, d_v, θ_c – but they can also be written in terms of θ_s and ϕ_s as

$$\vec{\boldsymbol{r}}_{\boldsymbol{s}} = |\vec{\boldsymbol{r}}_{\boldsymbol{s}}| \begin{bmatrix} \sin\theta_s \cos(\phi_s - \pi) \\ \sin\theta_s \sin(\phi_s - \pi) \\ \cos\theta_s \end{bmatrix}, \tag{81}$$

where π is subtracted from ϕ_s due to the same coordinate convention described in Section 3.5 above.

By setting Equations (78) and (81) equal to each other, it is possible to solve for the pixel indices n_h and n_v in terms of both the spherical scatter coordinates (θ_s, ϕ_s) and the measurement geometry parameters. The process requires squaring terms and taking square roots, so multiple solutions exist with identical form but varying signs. In particular, the solution

$$n_h = \frac{R}{d_h}\left(\frac{\cot\theta_c \sin\theta_s \cos(\phi_s - \pi) - \cos\theta_s}{\cot\theta_c \cos\theta_s + \sin\theta_s \cos(\phi_s - \pi)}\right) \tag{82a}$$

$$n_v = \frac{R}{d_v}\left(\frac{\sin\theta_s \sin(\phi_s - \pi)}{\cos\theta_c \cos\theta_s + \sin\theta_c \sin\theta_s \cos(\phi_s - \pi)}\right) \tag{82b}$$

produces expected results for geometries within the scatter hemisphere.

Several limiting cases can be used to verify the behavior of Equation (82a) and (82b). First, when the CCD is located at the scatter hemisphere zenith where $\theta_c = 0$, the zenith scatter direction ($\theta_s = 0$) should map to the central pixel $(n_h, n_v) = (0, 0)$. Furthermore, for any fixed azimuth ϕ_s, changes in θ_s should trace radial lines on the CCD surface originating at the central pixel, while for any fixed θ_s, changes in ϕ_s should project circles onto the CCD surface centered about the central pixel. In fact, when the limit of Equations (82a) and (82b) are taken as θ_c approaches zero, they

reduce to

$$n_h|_{\theta_c=0} = \frac{R}{d_h} \tan\theta_s \cos\left(\phi_s - \pi\right) \tag{83a}$$

$$n_v|_{\theta_c=0} = \frac{R}{d_v} \tan\theta_s \sin\left(\phi_s - \pi\right), \tag{83b}$$

which indeed match the expected behaviors. The signs of the outputs also match the established coordinate conventions. For example, for any θ_s when $\phi_s = 180°$, representing in-plane forward scatter directions along the $+\hat{x}$ axis, the vertical pixel index n_v remains zero while the horizontal pixel index n_h is positive. Conversely, when $\phi_s = 0$, representing in-plane backscatter directions along the $-\hat{x}$ axis, n_v remains zero while n_h is negative. When $\phi_s = 90°$, representing out-of-plane scatter along the $-\hat{y}$ axis, n_h remains zero while n_v is negative, and likewise when $\phi_s = 270°$, representing out-of-plane scatter along the $+\hat{y}$ axis, n_h remains zero while n_v is positive.

Although Equations (83a) and (83b) are not valid if $\theta_s = 90°$, this is an acceptable constraint. By contradiction, the CCD can never measure the scatter hemisphere horizon when it is located at the hemisphere zenith where $\theta_c = 0$.

As another limiting case, if the CCD is positioned at the scatter hemisphere horizon where $\theta_c = 90°$, the scatter direction $(\theta_s, \phi_s) = (90°, 180°)$ should map to the central pixel $(n_h, n_v) = (0, 0)$. Furthermore, due to the relatively small angles subtended by the entire array, changes in θ_s near the horizon should mostly manifest as changes in horizontal pixel index n_h, while changes in ϕ_s near the horizon should mostly manifest as changes in vertical pixel index n_v. In fact, when the limit of Equations (82a) and (82b) are taken as θ_c approaches 90°, they reduce to

$$n_h|_{\theta_c=90°} = -\frac{R}{d_h} \cot\theta_s \sec\left(\phi_s - \pi\right) \tag{84a}$$

$$n_v|_{\theta_c=90°} = \frac{R}{d_v} \tan\left(\phi_s - \pi\right). \tag{84b}$$

which do match the expected behaviors. As with the zenith case, the signs of the outputs in this horizon case also match the established coordinate conventions. When ϕ_s is held constant at 180°, θ_s values less than 90° map to negative n_h values while n_v remains zero. Conversely, when θ_s is held constant at 90°, ϕ_s values less than 180° map to negative n_v values and ϕ_s values greater than 180° map to positive n_v values, while n_h remains zero regardless.

During the simplification from Equations (82a) and (82b) to Equations (84a) and (84b), n_h retains its dependence on both θ_s and ϕ_s, but n_v loses its dependence on θ_s. In reality, when θ_c is set to any values less than 90°, which will be the case for any practical measurements away from grazing angles, the coupling inherent in Equations (82a) and (82b) returns, so that changes in either θ_s or ϕ_s affect both n_h and n_v simultaneously, despite the limiting case.

Finally, Figure 15 illustrates how contours of constant θ_s and ϕ_s throughout the scatter hemisphere should be expected to overlay onto the CCD surface for the full range of θ_c values. In the illustration, the perspective is from a point along the $-\hat{z}$ axis, looking through the material surface ($\hat{x}$-$\hat{y}$ plane) towards the scatter hemisphere zenith. The red concentric rings are plots of constant θ_s in 10° increments projected onto the $\hat{x}$-$\hat{y}$ plane, starting from $\theta_s = 0$ at the center and reaching $\theta_s = 90°$ at the outermost ring. The red radial lines are plots of constant ϕ_s in 30° increments. The dashed grids are illustrations of the CCD pixel array, also projected onto the $\hat{x}$-$\hat{y}$ plane for three different θ_c locations (approximately 0°, 20°, and 60°). Although the depicted size of the pixel array is exaggerated for better visualization, the behavior is consistent. In effect, for smaller values of θ_c, the contours of constant θ_s contained within the CCD field of view will appear more curved, while those visible for larger values of θ_c will appear more vertical, approaching nearly straight lines at $\theta_c = 90°$. Simultaneously, the range of ϕ_s radials contained within the CCD field of view will

be larger when θ_c is smaller, and vice versa.

Pixel Solid Angles.

Even under perfect alignment assumptions, only the central pixel points directly at the center of the illumination spot. As illustrated in Figure 16, any given pixel (such as the example outlined in dashed red) points in the direction denoted $\hat{\boldsymbol{n}}_{\boldsymbol{d}}$, which is offset from the scatter vector $\vec{\boldsymbol{r}}_{\boldsymbol{s}}$ by the angle

$$\theta_d = \tan^{-1}\left(\frac{|\vec{\boldsymbol{r}}_{\boldsymbol{p}}|}{R}\right) = \tan^{-1}\left(\frac{\sqrt{n_h^2 d_h^2 + n_v^2 d_v^2}}{R}\right). \tag{85}$$

It can still be assumed that $|\vec{\boldsymbol{r}}_{\boldsymbol{s}}|^2$ is much greater than both the apparent illumination spot size dA_s and the pixel size dA_d, so that pixel solid angle can be approximated well by

$$\Omega_d \approx \frac{dA_d \cos\theta_d}{|\vec{\boldsymbol{r}}_{\boldsymbol{s}}|^2} = \frac{d_h d_v R}{\left(n_h^2 d_h^2 + n_v^2 d_v^2 + R^2\right)^{3/2}}, \tag{86}$$

where the simplification on the right arises because 1) $dA_d = d_h d_v$, 2) $\cos\left(\tan^{-1}(x)\right) = 1/\sqrt{1+x^2}$, and 3) $|\vec{\boldsymbol{r}}_{\boldsymbol{s}}|$ can be substituted from Equation (79). It should make sense that the expression for Ω_d does not depend on θ_c.

When nominal specifications from the augmented CASI® setup are substituted into Equation (86) (specifically $d_h = d_v = 5.5 \times 10^{-6}$ μm and $R = 0.325$ m), the pixel solid angles are listed in Table 3. The center cell in the table corresponds to the solid angle subtended by the center pixel $(n_h, n_v) = (0, 0)$, the top-left cell in the table corresponds to the top-left pixel $(n_h, n_v) = (-1647, -1235)$, the bottom-right entry in the table corresponds to the bottom-right pixel $(n_h, n_v) = (1648, 1236)$, and so on. The center pixel subtends 2.864×10^{-10} sr^{-1}, while the corner pixels subtend 0.0052×10^{-10} sr^{-1} (or 0.182%) less.

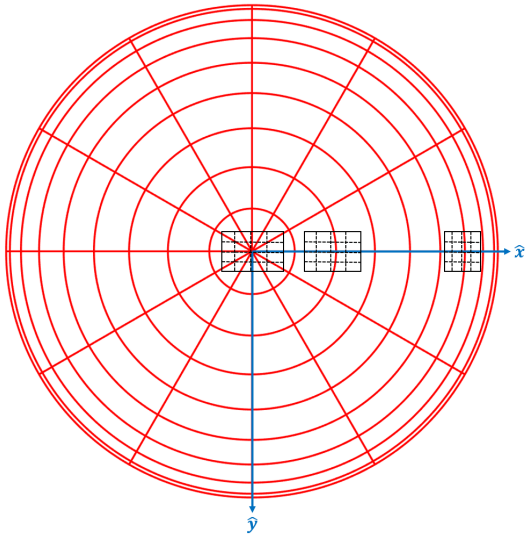

Figure 15. Illustration of constant θ_s and ϕ_s contours projected onto the material surface ($\hat{x}$-$\hat{y}$ plane). The concentric red rings are plots of constant θ_s in 10° increments, and the red radial lines are plots of constant ϕ_s in 30° increments. The dashed grids are illustrations of the CCD pixel array, enlarged for effect, also projected onto the $\hat{x}$-$\hat{y}$ plane for $\theta_c \approx 0^\circ$, 20°, and 60° (center to right). As θ_c increases, the contours of constant θ_s become less curved and more vertical relative to the CCD, and the CCD contains smaller ranges of ϕ_s.

3.6 Extending Dynamic Range

Within any individual frame, at best, the camera can only capture relative differences in power readings up to 4.2 orders of magnitude between pixels, since each pixel registers outputs between 0 and 16,383 digital counts. More realistically, depending on camera settings, if the noise floor is near 50 digital counts, the dynamic range of a single frame with a single exposure time drops closer to 2.5 orders of magnitude. More details on noise characterization are provided in Section 4.2, but fortunately, two methods for increasing the usable dynamic range include increasing exposure time and reducing OD by removing ND filters.

Manipulating exposure time is the primary method for extending dynamic range in this work. Due to noise considerations, Thorlabs® recommends camera cooling when using exposure times greater than 5000ms (the model used for this work is

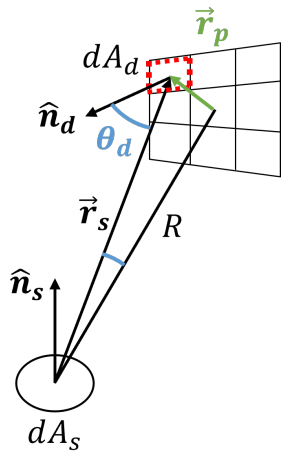

Figure 16. Illustration of the radiometric geometry relevant to calculating the solid angle Ω_d subtended by each pixel. The differential source area dA_s is the illuminated spot on the material sample, oriented with surface normal $\hat{n}_s$. The differential detector area dA_d corresponds to an individual pixel area (example in dashed red), oriented with surface normal $\hat{n}_d$. Since the CCD is flat, the angle θ_d between $\hat{n}_s$ and $\vec{r}_s$ can be calculated by using the geometric relationships among $\vec{r}_s$, $\vec{r}_p$, and R.

uncooled). Increasing exposure time from 1 ms to 5000 ms effectively increases the dynamic range by 3.7 orders of magnitude. In practice, however, due to a combination of inherent detector noise and background signals, the uncooled camera performs best with exposure times up to 1000 ms, providing a boost of 3 orders of magnitude. Again, more details on noise and background characteristics can be found in Section 4.2.

CCD pixel measurements with separate exposure times can be combined to form a single high-dynamic range output given in scaled digital counts (sDC). In simple fashion, the frame with the longest exposure time serves as the baseline, where unsaturated pixels retain their values. Saturated pixels are then replaced using unsaturated pixels from the next shortest exposure time, but their values are scaled according to the difference in exposure. For instance, if a pixel is saturated at 5000 ms exposure, but reads 10,000 digital counts at 1000 ms exposure, then its value can be scaled to $10,000 \times 5,000/1,000 = 50,000$ sDC. The process is iterated until all pixels are scaled to unsaturated values, which should be true for the frame with the fastest exposure

Table 3. Solid angle Ω_d subtended by select CCD pixels spanning the full array in the augmented CASI® system, given in sr. The center cell corresponds to the center pixel $(n_h, n_v) = (0, 0)$, the top-left cell corresponds to the top-left pixel $(n_h, n_v) = (-1647, -1235)$, the bottom-right cell corresponds to the bottom-right pixel $(n_h, n_v) = (1648, 1236)$, and so on.

2.859×10^{-10}	$\cdots$	2.862×10^{-10}	$\cdots$	2.859×10^{-10}
$\vdots$	$\ddots$	$\vdots$	$\iddots$	$\vdots$
2.861×10^{-10}	$\cdots$	2.864×10^{-10}	$\cdots$	2.861×10^{-10}
$\vdots$	$\iddots$	$\vdots$	$\ddots$	$\vdots$
2.859×10^{-10}	$\cdots$	2.862×10^{-10}	$\cdots$	2.859×10^{-10}

time when enough OD is utilized. This stitching process is demonstrated in Section 3.7 using a beam signature as the first example.

The second possible method for extending dynamic range is to remove ND filters to thereby reduce the OD during a measurement. However, when reducing OD, care must be taken to avoid damaging the CCD. As already mentioned, without direct knowledge of CCD damage thresholds, a conservative method involves always ensuring that each pixel is unsaturated at the fastest exposure time. Since this work is only concerned with measurements centered on the specular direction, the OD will not be reduced for any measurement beyond the point of saturation for the peak signal pixel reading. Nevertheless, reducing OD may become a viable means of extending dynamic range when the detector arm is rotated for off-specular measurements where the peak scatter signal no longer intercepts any pixels on the CCD.

3.7 Beam Signature

Once setup, alignment, and calibration are complete, measurements of the source beam provide a baseline from which to compare material BRDF measurements, as well as provide the total incident power Φ_i, which is necessary for calculating BRDF

according to Equation (45). The original CASI® system conducts a signature scan by centering the detector on the unimpeded but focused source beam, measuring the total power contained in the incident beam with a wide aperture, and then doing a finely resolved in-plane measurement sweep, all in order to calculate the BRDF of the beam itself without a material sample. The camera accomplishes a similar baseline by measuring the focused and aligned beam centered on the FPA, but now includes both out-of-plane and in-plane data within a single frame. In addition to measuring the beam itself, the background signal can be collected by taking another measurement with the laser source on, but blocking the beam path at the CASI® optic box output port. The background reading can later be subtracted from the beam signature when computing incident power.

Raw Measurement.

Figure 17 demonstrates a typical result using the CCD detector to measure beam signature of the focused 15 mW red HeNe laser using $OD_b = 5.2$ at various exposure times. Each image is given in raw digital counts. By design, no pixels are saturated at 1 ms. Although 1000 ms will be the maximum exposure time selected for most of this work, an additional exposure of 5000 ms is incorporated here, simply to demonstrate the stitching scheme's ability to handle differences in exposure time less than a full order of magnitude. As expected, more pixels are saturated as exposure time increases, but fainter signals are accessed away from the center of the source beam. Due to the relatively smaller dynamic range available at an individual exposure time, the digital count results are presented on a linear rather than logarithmic scale.

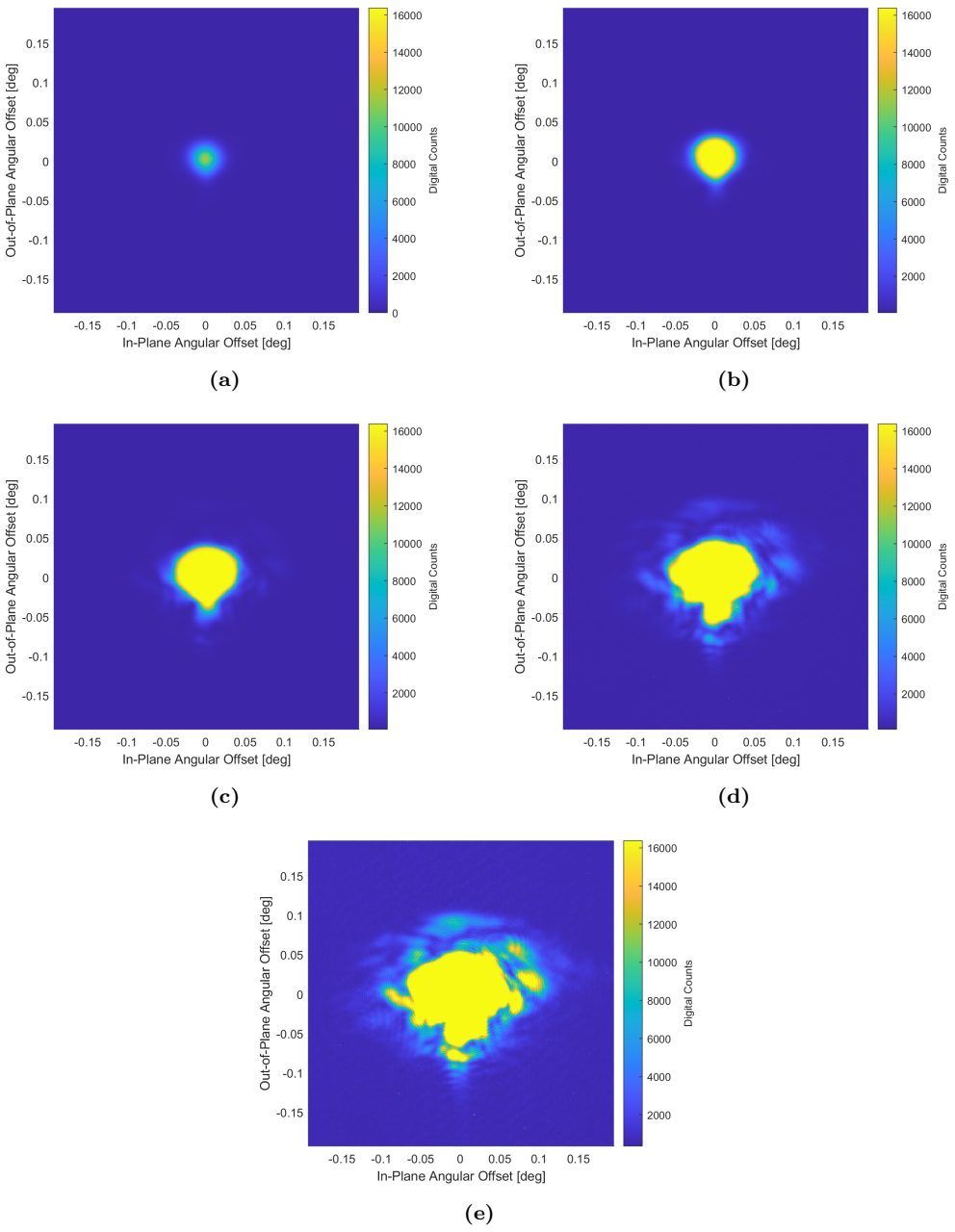

Figure 17. Comparisons of focused beam signature at various exposure times: 1 ms in (a), 10 ms in (b), 100 ms in (c), 1000 ms in (d), and 5000 ms in (e). Here, $OD_b = 5.2$, and in each case, 66 full frames were averaged and then zoomed to the center 400x400 pixels for display. Digital counts are presented on a linear scale for individual exposure times.

Stitching Exposure Times.

Using the stitching scheme described in Section 3.6, the beam signature measurements at separate exposure times can be combined to form a single high-dynamic range beam signature. Figure 18 shows an example of the horizontal in-plane cross-section of the stitched result for the beam signature. As expected, the stitched result traces the scaled values of one frame until reaching a saturation limit, where it switches to scaled values from another. This simple method does not account for differences or inconsistencies among the frames, such as noise levels, and so does not guarantee smooth transitions at the boundaries. For instance, discontinuities are noticeable when zoomed in on the specular peak in (b).

Gaussian Fit Analytics.

An analytic two-dimensionally symmetric Gaussian fit can be computed from the beam signature measurement data using a tool such as MATLAB®'s Curve Fitting Tool. Differences between the best fit and the beam signature can be used to identify subtle asymmetries or other imperfections in the source signature. Figure 19 shows several useful plots for the portion of a beam signature collected with 1 ms exposure, which captures all of the beam's signal above the value at its $1/e^2$ width. The figure includes a two-dimensional plot of the beam signature measurement, a two-dimensional image of the best fit, a map of the differences between the measurement and fit, and various cross-sections through the beam center including in-plane, out-of-plane, and $\pm 45°$, all compared to the fit. Again, with one exposure time, the results are presented on a linear scale.

In particular, when the pixel mapping is converted to in-plane and out-of-plane angular offset, the Gaussian diameters of the measured beam cross-sections are each less than 0.050°, and differ from each other by less than 0.004°. It is worth noting

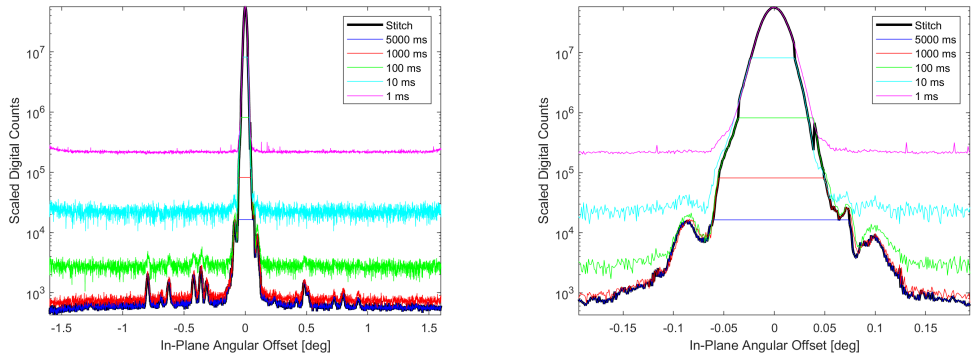

Figure 18. Stitched beam signature after combining various exposure times. An in-plane slice example is shown here. The black line represents the final stitched result, while the other colors represent individual exposure times, given in scaled digital counts.

that the typical default step size for the CASI® when using its smallest aperture is 0.011°, while the angular extent of the center pixel is $(9.70 \pm 0.09) \times 10^{-4}$ degrees, as described in Section 3.3.

3.8 BRDF Calculation

Once the beam signature and its background signal have been collected and stitched, the required pieces now exist for converting the raw pixel readings of any subsequent measurements from sDC into BRDF values using Equation (45).

First, incident flux Φ_i is calculated by summing the beam signature's pixel values in sDC across the entire array. Before computing the sum, the beam signature background signal is typically subtracted. When implementing as much background suppression as practical, described in Section 3.3, the difference in Φ_i after background subtraction is less than 4%. However, Φ_i must also be adjusted to account for differences in the ND filter OD used for material measurements (OD_m) and the ND filter OD used for the beam signature (OD_b). In reality, within the BRDF calculation, the ratio Φ_s/Φ_i matters, not the absolute values of either [13]. When incident flux is

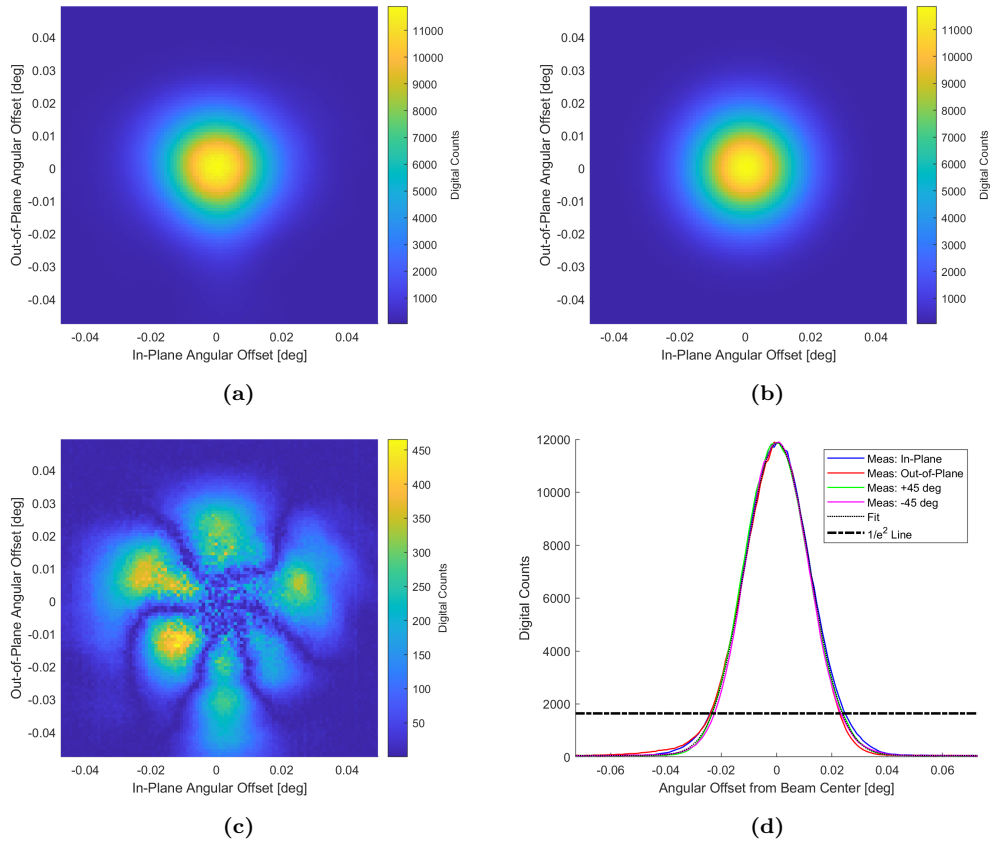

Figure 19. Comparisons of focused beam signature with symmetric Gaussian fit, using 1 ms exposure and $OD_b = 5.2$. Pixel dimensions have been converted to in-plane and out-of-plane angular offsets, given in deg. The images and plots are cropped and zoomed at the FPA center, with measured beam data in (a), the symmetric Gaussian best fit computed by MATLAB®'s Curve Fitting Tool in (b), magnitudes of the differences between each pixel's measured and fitted value in (c), and comparisons of various measurement cross-sections overlaid onto a single plot with the fit (d). Note that the colorbar scale in plot (c) has been lowered relative to the others in order to improve contrast.

computed by summing beam signature pixel values with certain ND filters in place, that particular incident flux value remains valid for any scatter flux measurements using the exact same ND filters. However, when scattered flux measurements are made with less OD than the beam signature, then the ratio Φ_s/Φ_i must be compensated. This can be accomplished by adjusting Φ_i according to

$$\Phi_i = \Phi_b \times 10^{(\mathrm{OD}_b - \mathrm{OD}_m)}, \tag{87}$$

where Φ_b represents the incident flux summation using the ND filter attenuation OD_b for the beam signature, OD_m indicates the ND filter attenuation used for the scattered flux measurement, and Φ_i now becomes the incident flux adjusted for the difference in ND filters. As should be expected, when $\mathrm{OD}_m = \mathrm{OD}_b$, then $\Phi_i = \Phi_b$, with no incident flux adjustment required.

For any beam signature or material measurement, the scatter angles (θ_s,ϕ_s) and the solid angle Ω_d are calculated for each pixel according to Equations (80a), (80b), and (86), respectively, using the nominal values $d_h = d_v = 5.5 \times 10^{-6}$ μm and $R =$ 0.325 m. In this work, each measurement is centered on the specular peak, so θ_c is nominally set to θ_i.

Finally, the scatter flux Φ_s is simply the sDC value for an individual pixel from any desired measurement. In this work, both measurements and beam signatures were stitched using the same exposure times (1, 10, 100, and 1000 ms), so the baseline for computing sDC, as described in Section 3.6, was the same in each case. However, if different exposure times are utilized, then Φ_s must be compensated, which requires multiplying by the ratio of the maximum beam signature exposure time to the maximum measurement exposure time. Of course, as long as both maximum exposure times are equivalent, then this ratio remains unity.

For each measurement, it is also possible to use Equations (82a)–(83b) to generate

contours of constant θ_s and ϕ_s for overlay onto the BRDF measurement plots. Each measurement frame contains some range of θ_s and ϕ_s values. Contours of constant θ_s can be generated by choosing desired θ_s values within the range of a frame, and then calculating n_h and n_v across the frame's full range of ϕ_s values. Likewise, contours of constant ϕ_s can be generated by choosing desired ϕ_s values, and then calculating n_h and n_v across the frame's full range of θ_s values.

Applied to Beam Signature.

Without yet making subsequent material measurements, the BRDF calculation can be applied to the beam signature itself. Conveniently in this case, $\mathrm{OD}_m = \mathrm{OD}_b$ and $\theta_c = 0$. The BRDF calculation yields the results shown in Figure 20. Horizontal and vertical pixel indices are plotted along each figure's horizontal and vertical axes, respectively, and each pixel's BRDF value is displayed according to both linear and logarithmic color scales, as shown. Because the beam signature represents an ideal specular material at normal incidence, $\theta_c = 0$ for this measurement geometry.

On the linear scale, the beam shape qualitatively appears quite Gaussian with a peak BRDF value of 3.82×10^6 sr^{-1}. Depending on the beam's focus, which must be re-accomplished between using the CCD and original detectors, the CASI® typically registers peak values near its maximum measurable BRDF value of 3.5×10^6 sr^{-1}. However, on the logarithmic scale, several artifacts and aberrations become apparent below approximately 250 sr^{-1}. The sources of the artifacts are most likely stray light caused by the infrared blocking protective cover within the camera aperture, noticeable because this system does not incorporate an additional lens in front of the CCD camera. Beam signature comparisons between the CCD-augmented system and the original CASI® are presented with more detail in Section 4.6.

In Figure 20(b), the red concentric circles are contours of constant θ_s calculated

in 0.5° increments, while the red radial lines are contours of constant ϕ_s calculated in 30° increments. The contours match the expected behavior for the measurement geometry when $\theta_c = 0$, as described in Section 3.5. In addition, Table 4 displays the range of θ_s and ϕ_s values found within the pixel array, given in degrees. The cells correspond to pixel location with the same format as Table 3. Both Table 4 and the contours in Figure 20 confirm that for this particular geometry, the CCD captures a full 360° of ϕ_s values, with several degrees of θ_s range.

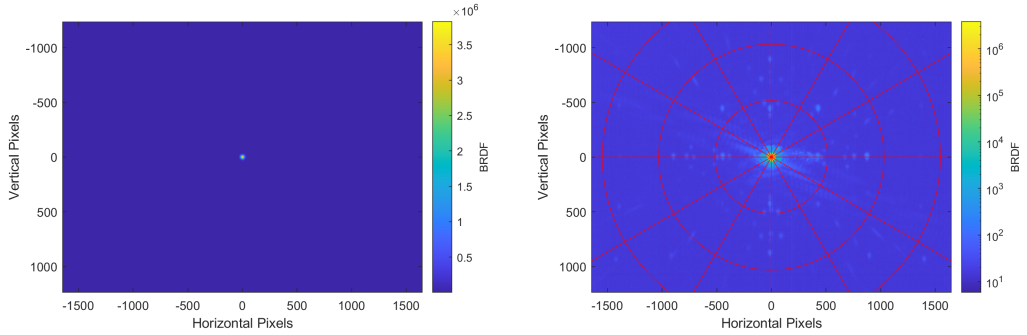

Figure 20. Plots of beam signature measurement data using a linear scale (a) and logarithmic scale (b), with an overlay with contours of constant θ_s and ϕ_s in $0.5°$ and $30°$ increments, respectively, in (b). Here $\theta_c = 0$, and the concentric red circles represent contours of constant θ_s, while the red radial lines represent contours of constant ϕ_s.

Table 4. Scatter angles (θ_s, ϕ_s) for select CCD pixels spanning the full array when $\theta_c = 0$ in the augmented CASI® system. Angles are curtailed at four significant figures for simplicity and given in degrees. The center cell corresponds to the center pixel $(n_h, n_v) = (0, 0)$, the top-left cell corresponds to the top-left pixel $(n_h, n_v) = (-1647, -1235)$, the bottom-right cell corresponds to the bottom-right pixel $(n_h, n_v) = (1648, 1236)$, and so on.

$(1.995, 36.86)$	$\cdots$	$(1.197, 90)$	$\cdots$	$(1.996, 143.2)$
$\vdots$	$\ddots$	$\vdots$	$\iddots$	$\vdots$
$(1.597, 0)$	$\cdots$	$(0, 180)$	$\cdots$	$(1.598, 180)$
$\vdots$	$\iddots$	$\vdots$	$\ddots$	$\vdots$
$(1.996, 323.1)$	$\cdots$	$(1.198, 270)$	$\cdots$	$(1.997, 216.9)$

3.9 Next Steps

With the setup, calibration, alignment, and beam signature complete, along with the methodology for mapping each pixel to appropriate scatter angles and solid angles, the CCD-augmented system is now ready to collect scatter flux and convert pixel readings to BRDF values. However, as with any measurement system, it is important to be able to quantify uncertainties in the results. Thus, Chapter IV steps through a robust uncertainty analysis for this novel system, prior to presenting material measurement results in Chapter V.

IV. Uncertainty Analysis

The original uncertainty analysis for the CASI® [13] was built upon identifying uncertainties in various system parameters, and then quantifying how changes from nominal parameter values affect the overall BRDF calculation in Equation (45). To remain conservative, the impacts of each system uncertainty on each variable were treated independently as first-order linear contributions and then added in quadrature in Equation (71) [13]. Each term in Equation (71) was further subdivided in quadrature whenever multiple system uncertainties applied.

To conduct an uncertainty analysis for the CCD-augmented CASI®, each of the original uncertainties were examined and new uncertainties were considered. The uncertainty analysis presented here ultimately builds upon original CASI® analysis methods [13], but also incorporates the fundamental differences of using a multi-pixel array detector, using formulations described in Chapter III.

Following suit with the rest of this work, this uncertainty analysis will focus on CCD measurements centered on the specular peak, leaving considerations associated with off-specular measurements for future work. Polarizing elements are also not incorporated, so polarization misalignment terms are ignored.

4.1 Uncertainty Linearization

Approximating an uncertainty as a first-order linear term can be useful, especially when the formulation can be written analytically. For example, the solid angle relative uncertainty for a circular aperture is derived by starting with the expression

$$\Omega_d = \frac{\pi r^2}{R^2}, \tag{88}$$

and then linearizing with respect to changes in each variable r and R, which becomes

$$\frac{\Delta\Omega_d}{\Omega_d} \approx \left[\left(\frac{\frac{\partial\Omega_d}{\partial r}\Delta r}{\Omega_d}\right)^2 + \left(\frac{\frac{\partial\Omega_d}{R}\Delta R}{\Omega_d}\right)^2\right]^{1/2} = \left[\left(\frac{2\Delta r}{r}\right)^2 + \left(\frac{2\Delta R}{R}\right)^2\right]^{1/2}. \quad (89)$$

In this case, computing and writing the partial derivatives is straightforward for each term.

However, when the expressions become more complicated, each term can also be calculated by evaluating the original expression itself, rather than using partial derivatives. For example, the solid angle relative uncertainty could also be written

$$\frac{\Delta\Omega_d}{\Omega_d} = \left[\left(\frac{\Omega_d|_{r+\Delta r,R} - \Omega_d|_{r,R}}{\Omega_d|_{r,R}}\right)^2 + \left(\frac{\Omega_d|_{r+,R+\Delta R} - \Omega_d|_{r,R}}{\Omega_d|_{r,R}}\right)\right]^{1/2}. \quad (90)$$

The latter technique will be implemented occasionally for complex expressions.

4.2 Scatter Flux Uncertainty

This section addresses uncertainty in the scatter flux measurement Φ_s for each CCD pixel. Aside from polarization misalignment, the original analysis identified three sources of scatter flux uncertainty [13]. Out-of-plane aperture misalignment will be neglected, while system noise and detector non-linearity contributions contain significant changes due to differences between the original single-pixel detectors and the multi-pixel CCD array.

Out-of-Plane Aperture Misalignment.

The original CASI® apertures translate in the out-of-plane direction (along the $\hat{y}$ axis) in order to align the measured scatter direction within the plane of incidence (usually by centering on the specular peak). However, accuracy limitations in the

aperture movements and centering routines lead to scatter direction misalignment in the out-of-plane direction, where the scattered flux measurement differs from an ideal measurement located exactly in-plane [56, 13]. Ultimately, with a single-pixel detector, the scattered flux lost due to this misalignment cannot be directly recovered, and the associated loss must be modeled as an uncertainty.

This term is not necessary for the CCD-augmented system, however, simply because it incorporates multi-pixel and microlens arrays. After following the CCD alignment procedures from Section 3.4, the CCD still captures in-plane scattered flux within the pixel array, even with small misalignment. In other words, even when imperfectly centered on a specular peak, that peak is still clearly within the CCD frame. The in-plane flux simply shifts to other pixels in the array, rather than being clipped by the aperture.

Although out-of-plane (and other translational) misalignment impacts scatter direction in the CCD-augmented system, it no longer impacts scattered flux, so this term is no longer necessary.

System Noise.

As stated in the original analysis, system noise contributes to scatter flux uncertainty through the noise-to-signal ratio [13]. Rather than calculating this term directly, though, detector noise limits can be characterized and then simply used to identify and ignore measurement regions near the noise level [59, 13]. The same methodology will be employed in this section, with extensions to the CCD-augmented system.

Background Limit.

Section 3.3 discussed several background signal considerations for the CCD-augmented system. In particular, the CCD detector is not integrated with the CASI®'s chopper wheel and lock-in amplifier, nor does it use a lens mounted in front of the detector, both of which reduce the original detector's susceptibility to unwanted background signals. Instead, when using the CCD detector, the ambient room lights are reduced as much as practical, the laser beam path is blocked from CCD detector's field of view, and a 4 inch lens tube is mounted to the front of the camera.

Additionally, the original CASI® software automatically updates exposure time and detector gain, and does not require the use of ND filters with typical low-power visible laser sources, even when measuring the beam signature directly. In contrast, CCD exposure time and gain values must be set manually, and in the absence of known laser damage thresholds, ND filters are required even with relatively low-power visible lasers, both to protect the pixel array and provide unsaturated specular measurements, as introduced in Section 3.3.

The background signal for any system configuration can be characterized by taking flux readings with the laser on but blocked at the CASI® optics box output (prior to reaching the sample stage). In addition, inherent signal-independent detector noise characteristics (which excludes photon shot noise) can be characterized by taking flux readings with an aperture cover or lens cap on. When background flux readings approach detector noise flux readings, the system is operating near the detector noise limit.

Minimum and Maximum BRDF Measurements.

Ultimately, when limited by detector noise rather than background contributions, the noise equivalent BRDF is directly proportional to the detector's noise equivalent

flux, but varies inversely with incident flux and detector solid angle [59]. Using a 15 mW helium-neon (HeNe) laser at 632.8 nm wavelength, the noise floor of the original CASI® using a silicon-based detector was validated through measurement at approximately 5×10^{-8} sr^{-1} [56, 59]. Conversely, for an ideal specular material, represented by the beam signature, the CASI® detector aperture can collect nearly the entire beam's flux within a single solid angle at the specular peak. In this case, the ratio of scattered flux to incident flux approaches unity, and the maximum measurable BRDF approaches $1/\Omega_d$. Using its smallest aperture, the maximum BRDF value of the original CASI® system is approximately 3.5×10^6 sr^{-1} [59]. Thus, the original system is capable of measurements spanning nearly 15 orders of magnitude.

In the CCD-augmented system, measurements are typically captured using 1, 10, 100, and 1000 ms exposure times with default gain and black level offsets. Since the saturation limit for each individual pixel is 16,383 digital counts, when the results from each exposure time are scaled and stitched together according to Section 3.6, the scatter flux values for each pixel can range from zero to $\Phi_{s,\text{high}} = 1.6383 \times 10^7$ sDC. Meanwhile, using the 15 mW red HeNe laser with $\text{OD}_b = 5.2$, a representative incident flux summation yields $\Phi_b = 9.828 \times 10^9$ sDC.

Background measurements were captured after reducing background interference as much as practical. After scaling and stitching, the mean pixel output across the entire array was 48.05 sDC with a standard deviation of 23.11 sDC. For comparison, when the lens cap was installed, the mean pixel output was only slightly lower at 45.88 sDC with a similar standard deviation, demonstrating that the CCD-augmented system was operating near the detector noise limit (within 5%). The scatter flux lower limit can thus be expressed $\Phi_{s,\text{low}} = 48.05$ sDC. Due to their location in the optics box, the ND filters attenuate the signal with negligible changes to the background, so $\Phi_{s,\text{low}}$ does not change with OD_m.

The noise equivalent BRDF and its associated standard deviation for the CCD-augmented system using the 15 mW red HeNe laser can then be calculated by substituting Equation (87) into Equation (45), and then also substituting the nominal values $\cos\theta_s = 1$, $\Omega_d = 2.864 \times 10^{-10}$ sr^{-1}, $\Phi_b = 9.828 \times 10^9$ sDC, and $\mathrm{OD}_b = 5.2$. Then, the scattered flux Φ_s is set first to the lower operating limit $\Phi_{s,\mathrm{low}}$ and then to its standard deviation. When $\mathrm{OD}_m = \mathrm{OD}_b$, such as when measuring an ideal or highly reflective surface, the noise equivalent BRDF is 17.07 sr^{-1} with a standard deviation of 8.21 sr^{-1}. If however $\mathrm{OD}_b - \mathrm{OD}_m = 1.1$, such as when measuring the polished aluminum sample shown later in Section 5.2, the noise equivalent BRDF and standard deviation reduce to 1.36 sr^{-1} and 0.65 sr^{-1}, respectively. Finally, if scattered flux measurements are made without ND filters so that $\mathrm{OD}_m = 0$, then the minimum measurable BRDF reaches 1.08×10^{-4} sr^{-1}, with a standard deviation of 5.18×10^{-5} sr^{-1}.

If the source beam could be focused onto a single pixel with the appropriate OD_b to stay below pixel saturation, then $\Phi_s = \Phi_i$ in Equation (45), and the maximum measurable BRDF when $\mathrm{OD}_m = \mathrm{OD}_b$ theoretically becomes $1/\Omega_d = 3.5 \times 10^9$ sr^{-1}. In practice though, the red HeNe laser focuses to a minimum $1/e^2$ width of approximately 25 pixel widths. Instead, the practical peak BRDF value can be calculated by substituting $\Phi_{s,\mathrm{high}}$ into Equation (45). When $\mathrm{OD}_m = \mathrm{OD}_b$, for ideal or highly reflective measurements, the maximum measurable BRDF value becomes 5.82×10^6 sr^{-1}. When for example $\mathrm{OD}_b - \mathrm{OD}_m = 1.1$, the maximum measurable BRDF becomes 4.62×10^5 sr^{-1}. Finally, if $\mathrm{OD}_m = 0$, the maximum BRDF decreases to 36.7 sr^{-1}.

Dynamic Range Comparison.

Ultimately, for any stitched measurement composed of exposure times from 1 to 1000 ms with a fixed OD_m, as is the case for measurements centered on the specular

peak, the CCD-augmented system can measure BRDF values spanning approximately $\log_{10}(\Phi_{s,\text{high}}/\Phi_{s,\text{low}}) = 5.53$ orders of magnitude. For the sake of comparison, the ideal noise-free dynamic range would span $\log_{10}(\Phi_{s,\text{high}}) = 7.21$ orders of magnitude. If OD_m is increased or decreased, depending on the magnitude of the material's specular peak, the maximum and minimum measurable BRDF values shift accordingly, but still span 5.53 orders of magnitude within a single stitched CCD frame, representing a bit more than one-third of the original CASI's® dynamic range.

In theory, by rotating the CASI® detector arm to shift the CCD away from the specular direction, it becomes possible to safely reduce OD_m from $\text{OD}_m = \text{OD}_b$, perhaps all the way to $\text{OD}_m = 0$. The maximum achievable dynamic range could then increase to $\log_{10}(\Phi_{s,\text{high}}/\Phi_{s,\text{low}}) + \text{OD}_b$. For the 15 mW red HeNe laser source where $\text{OD}_b = 5.2$, the maximum theoretical dynamic range would become 10.7 orders of magnitude, or two-thirds of the original CASI's® dynamic range. However, this extension requires investigating impacts when the specular peak is shifted off the pixel array, such as stray reflections inside the camera aperture.

Non-Linearity.

In the original CASI® uncertainty analysis, detector linearity was evaluated by adding an ND filter to attenuate the source beam, and then comparing the expected and actual change in detector response [14]. The resulting error was limited to a maximum of 1% with software correction [13]. In the CCD-augmented system, though, each pixel functions as an independent detector, and each requires its own linearity evaluation, which cannot be readily accomplished by attenuating a highly focused Gaussian source laser. Specifications for our particular CCD list a maximum signal error due to non-linearity differences (1%), but this value is only valid from 10% to 90% saturation [62]. Furthermore, this linearity reporting may be in terms of average

pixel response [24], rather than the linearity of each pixel individually.

Following standard camera characterization methods [24], the CCD was centered 32 in from the 4 in aperture of an Electro-Optical Industries ISV410 integrating sphere with no lens or lens tube. Measurements were taken under continuously adjustable uniform illumination as 66-frame averages (limited by maximum individual file size) with 1 ms exposure. Ten luminance values (50, 100, 300, 500, 1000, 1500, 2000, 2500, 3000, and 3200 ft-L) were selected ranging from the sphere's minimum achievable stable luminance to near-saturation. At 50 ft-L, the average pixel reading was 292 DC (1.78% saturation), with a maximum of 336 DC and a minimum of 256 DC (1.56% saturation), all above the noise floor. At 3200 ft-L, the average pixel reading was 15,155 DC (92.5% saturation), with a minimum of 12,994 DC and a maximum of 15,636 DC (95.4% saturation), all below saturation.

As a baseline for comparison, CCD linearity was first computed using only the range of luminance values which induced 10-90% saturation (500-3000 ft-L), fitting a single linear regression to the array-wide pixel averages for each luminance. Using a standard formulation, the linearity errors at each luminance level were calculated as the relative difference between the measured array-wide pixel averages and the regression [24], expressed as

$$\Delta \mathrm{NL}_s[i] = \frac{y[i] - (a_0 + a_1 H[i])}{(a_0 + a_1 H[i])}. \tag{91}$$

In Equation (91), $H[i]$ represents the indexed set of scalar luminance values, $y[i]$ is the indexed set of scalar array-wide pixel averages measured at each luminance, and a_0 and a_1 are scalar linear regression fit parameters [24]. The linearity error $\Delta \mathrm{NL}_s[i]$ is then a scalar value at each luminance. The resulting maximum linearity error was 0.64%. When the regression parameters and linearity errors were re-calculated using the full luminance range (50-3200 ft-L), the maximum linearity error increased to

1.72%. However, this baseline method compresses the linearity characterization to a single value for the entire array at each luminance level.

Two additional methods extended the baseline method in order to isolate and characterize individual pixel linearity. In the first method, linear regression parameters were generated for each individual pixel's response over the full luminance range, and then linearity errors were calculated as the relative difference between each individual measured pixel response and its own regression at each luminance. Thus, in Equation (91), $y[i]$ became an array of individual pixel measurements at each luminance, a_0 and a_1 became arrays comprised of regression fit parameters for each pixel, and the linearity error $\Delta\mathrm{NL}_s[i]$ became an array comprised of error values for each pixel at each luminance. $\Delta\mathrm{NL}_s[i]$ could then be condensed by finding the maximum error for each pixel across all luminance values. Using this method, the maximum linearity error among all pixels was 3.52%, while the average linearity error for each pixel was 1.74% with a standard deviation of 0.14%. Although this method evaluates the linearity of each pixel independently, it does not capture differences in each pixel's response relative to a common baseline.

The final method combines the others and defines linearity error as the relative difference between each individual pixel response and the array-wide linear regression, ultimately describing each pixel's individual photo-response relative to a common array-wide average linear response. In this method, $y[i]$ remains the array of individual pixel measurements at each luminance, but a_0 and a_1 remain the scalar regression fit parameters from the array-wide pixel averages. Here, $\Delta\mathrm{NL}_s[i]$ is still an array comprised of error values for each pixel at each luminance, but now referenced to a single common regression. Again, $\Delta\mathrm{NL}_s[i]$ can be condensed by finding the maximum error for each pixel across all luminance values. Using this method, the maximum linearity error among all pixels was 16.32%, while the average linearity error for each

pixel was 2.18% with a standard deviation of 0.50%.

The final method will be used to assign a maximum non-linear error value $\Delta \mathrm{NL}_s$ to each pixel independently, taking into account non-uniformities among pixel photo-responses. Although the overall maximum error is rather high at over 16%, such values are significant outliers, and could either be corrected or ignored as desired. For example, for this particular CCD, only 0.021% of pixels exceed an error of 5.19%, or six standard deviations above the average error.

Combined Scatter Flux Uncertainty.

In summary, aperture misalignment is not applicable, and although system noise is characterized, it is left to visual identification. Thus, the only contributing term for scatter flux relative uncertainty becomes pixel non-linearity

$$\frac{\Delta \Phi_s}{\Phi_s} = \left[\Delta \mathrm{NL}_s^2\right]^{1/2}, \tag{92}$$

where $\Delta \mathrm{NL}_s$ is an array containing the maximum non-linear error for each pixel relative to the array-wide average linear response. Since $\Delta \mathrm{NL}_s$ can be negative, the root mean square ensures a positive value.

4.3 Incident flux Uncertainty

This section addresses uncertainty in measured incident flux Φ_i. Aside from polarization misalignment, the original analysis identified four sources of scatter flux uncertainty [13]. The detector noise and aperture area effects remain negligible, but non-linearity and temporal contributions are adjusted. An extra term is incorporated to address ND filter uncertainty.

System Noise.

As described in the original CASI® analysis, the same noise-to-signal ratio affects the detector output whether measuring incident or scatter flux, and so the noise contribution was not directly included within the incident flux uncertainty calculation [13]. Even though the CCD measures incident flux by summing over the entire array of pixels, this term can still be omitted. By averaging the beam signature over a maximum number of frames (66) and subtracting the detector-limited background measurement, noise contributions can be neglected.

Non-Linearity.

For the original single-pixel CASI® detectors, the same linearity error derived as part of the scatter flux uncertainty was also included as part of the incident uncertainty [13]. With a CCD, non-linear responses still affect each pixel when measuring the beam signature, but since the pixel outputs are summed, the average non-linear response matters more. At the focused 15 mW red HeNe minimum spot size, the $1/e^2$ beam width, which includes approximately 86% of the beam's power, still encompasses more than 1,850 pixels. When linearity error terms are calculated using the final method from Section 4.2, the average pixel non-linearity across the entire array and dynamic range is

$$\Delta \mathrm{NL}_i = 0.018\%. \tag{93}$$

This single scalar value becomes the non-linearity contribution $\Delta \mathrm{NL}_i$ to incident flux uncertainty.

Aperture Area.

Even when measuring incident flux from a focused Gaussian beam using the largest available aperture, part of the signal inevitably falls outside the collection area. The

original CASI® detectors have circular apertures, but our particular CCD has a rectangular array with square pixels. The relative flux outside the rectangular array can be approximated by

$$\frac{\Delta\Phi_A}{\Phi_A} = 1 - \text{erf}\left(\frac{\sqrt{2}a}{w}\right)\text{erf}\left(\frac{\sqrt{2}b}{w}\right), \tag{94}$$

where a and b represent the pixel indices at the edge of the array, and w is the $1/e^2$ radius of the focused laser spot on the CCD. For an array with 3296×2472 square pixels, a becomes 1648 and b becomes 1236. A numerical value for w can be found by performing a non-linear least squares fit to the 15 mW red HeNe laser's Gaussian beam signature, yielding approximately 25 pixel widths. When these values are substituted into Equation (94), the expression evaluates to zero within machine precision:

$$\left.\frac{\Delta\Phi_A}{\Phi_A}\right|_{w=25} \approx 0. \tag{95}$$

Thus, the aperture area term can be neglected for the CCD-augmented system.

Temporal Fluctuations.

The original CASI® detectors utilize a reference detector to monitor source power and correct for short-term fluctuations during scatter measurements, which allows for neglecting temporal uncertainty contributions [13]. However, the CCD is not integrated with a reference detector.

To evaluate the stability of the 15 mW red HeNe laser source, a NIST-calibrated photodiode power meter collected more than 1.5 hrs of power readings at 16.6 frames per second (fps). Due to individual file size limitations, the data was collected in roughly 15 min sets. The first collection began immediately after turning on the laser, with immediate transitions into the second and third sets. The fourth collection began

the next day, again immediately after turning on the laser, with immediate transitions into the fifth and sixth sets.

At most, due to individual file size limitations, our particular CCD collects 66 full frames at 2.3 fps, which spans approximately 28.7 seconds. Each set of power meter data can be converted into rolling 28.7 second averages, representing possible windows in which the CCD incident flux measurement occurs. The relative difference can be found between each rolling average and the overall 15 min average for the set, and this process can be repeated for each set. In both cases, as expected, the maximum relative difference was much higher within the first 15 min, before the laser had a chance to sufficiently stabilize. However, after the first 15 minutes, the maximum relative difference in incident flux within a 15 minute measurement window was 0.72%.

The same process can be repeated when the CCD collects smaller numbers of frames for a beam signature. For instance, when the CCD collects only 5 full frames at 2.3 fps, each incident flux collection spans approximately 2.17 seconds, and the power meter data is instead converted into 2.17 second rolling averages. Once again, the maximum difference relative to the overall 15 min average was much higher within the first 15 min, but afterwards peaked at 1.01%.

Rather than neglecting temporal flux relative uncertainty, it will be set to a single scalar value

$$\frac{\Delta\Phi_T}{\Phi_T} = 1.01\% \tag{96}$$

which contributes to each pixel uniformly.

Optical Density Uncertainty.

As shown in Equation (87), the measurement and scaling of Φ_i depends on the difference between OD_b and OD_m. In practice, the best OD for remaining just below

saturation can require stacking multiple ND filters, so that OD_b can be written $\mathrm{OD}_{b1}+\mathrm{OD}_{b2}+...+\mathrm{OD}_{bn}$, and OD_m can be written $\mathrm{OD}_{m1}+\mathrm{OD}_{m2}+...+\mathrm{OD}_{mk}$, where n and k indicate the total number of filters in each combination. For example, the 5.2 OD required for beam signature measurement can be accomplished by stacking $\mathrm{OD}_{b1}=4.0$, $\mathrm{OD}_{b2}=1.0$, and $\mathrm{OD}_{b3}=0.2$. Likewise, the 4.1 OD necessary for measuring a polished aluminum sample can be accomplished by stacking $\mathrm{OD}_{m1}=4.0$ and $\mathrm{OD}_{m2}=0.1$.

The set of absorptive ND filters available for this work have published OD tolerances based primarily on uncertainty in filter thickness during production. Unfortunately, from a transmission percentage standpoint, the published tolerances are rather large at higher OD values. For example, the 0.1, 0.2, and 0.3 OD filters have a tolerance of ± 0.01 OD, which corresponds to transmission uncertainties of 2.33% each, while the 4.0 OD filter has a tolerance of ± 0.2 OD, which alone corresponds to a transmission uncertainty of 58.5%.

The relative uncertainty in incident flux due to uncertainties in optical density can be written by linearizing Equation (87) with respect to changes in each OD value

$$\frac{\Delta\Phi_{\mathrm{OD}}}{\Phi_{\mathrm{OD}}} = \ln(10)\sqrt{\Delta\mathrm{OD}_{b1}^2+...+\Delta\mathrm{OD}_{bn}^2+\Delta\mathrm{OD}_{m1}^2+...+\Delta\mathrm{OD}_{mk}^2}. \tag{97}$$

If certain ND filters are repeated in both OD_b and OD_m, those terms can be omitted, because despite any tolerance, the actual value for an individual filter is constant.

It is important to note that this OD uncertainty depends largely on the ND filters required to measure a specific material, and represents a constant contribution across all pixels. Baseline published uncertainties represent worst-case knowledge, which could be significantly improved with independent filter characterization. For combined relative uncertainty calculations in Section 4.6, results will be presented using both worst-case and perfect OD uncertainties for comparison.

Combined Incident Flux Uncertainty.

In summary, system noise and aperture area considerations can be ignored for incident flux relative uncertainty. The relevant contributions become pixel non-linearity, temporal fluctuation, and ND filter uncertainties, which can be combined as

$$\frac{\Delta\Phi_i}{\Phi_i} = \left[\Delta \mathrm{NL}_i^2 + \left(\frac{\Delta\Phi_T}{\Phi_T}\right)^2 + \left(\frac{\Delta\Phi_{\mathrm{OD}}}{\Phi_{\mathrm{OD}}}\right)^2\right]^{1/2}. \tag{98}$$

Each term represents a single scalar value which is uniformly valid for every pixel measurement within a single stitched CCD frame.

4.4 Scatter Angle Uncertainty

This section addresses uncertainty in the scatter angles associated with each pixel during a CCD measurement. In the original analysis for single-pixel detectors making in-plane measurements, uncertainty in θ_s depends only on the uncertainty in the material sample's normal direction and the angular precision of the detector arm [13, 11]; uncertainty in ϕ_s was not relevant. During a CCD measurement, though, each pixel maps to a unique (θ_s, ϕ_s) combination which depends on pixel index (n_h, n_v), pixel dimensions d_h and d_v, the distance R from material sample to CCD location, and detector arm offset angle θ_c, as described in Section 3.5. This section describes how uncertainties in each parameter affect θ_s and ϕ_s even with perfect CCD alignment, and then describes a formulation for characterizing how CCD alignment uncertainty can further affect the scatter angles.

Uncertainty with Perfect Alignment.

Equations (80a) and (80b) provide the calculations for θ_s and ϕ_s assuming perfect alignment. Our current CCD has square pixels, so that $d_h = d_v = d$.

Uncertainty in θ_s.

By using partial derivatives, the relative uncertainty in θ_s due to the uncertainty ΔR is

$$\frac{\Delta\theta_{s_R}\sin\theta_s}{\cos\theta_s} = \left(\frac{R}{d^2(n_h^2+n_v^2)+R^2} + \frac{1}{dn_h\tan\theta_c - R}\right)\Delta R, \tag{99}$$

where the scaling factor $\sin\theta_s/\cos\theta_s$ comes from Equation (71). The relative contribution from $\Delta\theta_{s_R}$ is always zero at the center pixel where $(n_h, n_v) = (0, 0)$, which makes intuitive geometric sense. Moving the CCD closer to or farther from the material sample would not change the scatter direction for the center pixel.

Similarly, the relative uncertainty in θ_s due to the uncertainty Δd can be written

$$\frac{\Delta\theta_{s_d}\sin\theta_s}{\cos\theta_s} = \left(\frac{d(n_h^2+n_v^2)}{d^2(n_h^2+n_v^2)+R^2} + \frac{n_h}{R\cot\theta_c - dn_h}\right)\Delta d. \tag{100}$$

The relative contribution from $\Delta\theta_{s_d}$ is also always zero at the center pixel where $(n_h, n_v) = (0, 0)$, which again makes intuitive geometric sense, because changing pixel size does not alter the scatter direction of the center pixel.

Lastly, the relative uncertainty in θ_s due to the uncertainty $\Delta\theta_c$ can be written

$$\frac{\Delta\theta_{s_c}\sin\theta_s}{\cos\theta_s} = \left(\frac{dn_h\cos\theta_c + R\sin\theta_c}{R\cos\theta_c - dn_h\sin\theta_c}\right)\Delta\theta_c. \tag{101}$$

Notably, this uncertainty contribution does not depend at all on vertical pixel index n_v, meaning changes in detector arm location affect changes in θ_s equivalently for pixels in the same column.

Uncertainty in ϕ_s.

Although ϕ_s does not appear directly in the BRDF calculation given by Equation (45), this angle is important for annotating each pixel's scatter coordinates for data

analysis.

By using partial derivatives, the relative uncertainty in ϕ_s due to the uncertainty ΔR is

$$\frac{\Delta\phi_{s_R}}{\phi_s} = -\frac{dn_v \sin\theta_c}{d^2 n_v^2 + (dn_h \cos\theta_c + R\sin\theta_c)^2}\frac{\Delta R}{\phi_s}. \tag{102}$$

Notably, this relative uncertainty is zero if either $n_v = 0$ or $\theta_c = 0$, which makes intuitive sense. When the horizontal pixel row is aligned perfectly in-plane, changing the CCD's distance from the material sample does not change the azimuthal plane for those pixels. In addition, when the center of the CCD is lined up directly with the material surface normal, changing the distance does not change the azimuthal plane for any pixel, even though the zenith angles θ_s change.

Similarly, the relative uncertainty in ϕ_s due to the uncertainty Δd can be written

$$\frac{\Delta\phi_{s_d}}{\phi_s} = \frac{n_v R \sin\theta_c}{d^2 n_v^2 + (dn_h \cos\theta_c + R\sin\theta_c)^2}\frac{\Delta d}{\phi_s}. \tag{103}$$

This relative uncertainty also equals zero if either $n_v = 0$ or $\theta_c = 0$, which again makes intuitive geometric sense. When the horizontal pixel row is perfectly aligned in-plane, changing the pixel size does not change the azimuthal plane for the center pixel row. In addition, when the center of the CCD is lined up directly with the material surface normal, changing the pixel size does not change the azimuthal plane for any pixel, despite changing the zenith angles θ_s.

Finally, the relative uncertainty in ϕ_s due to the uncertainty $\Delta\theta_c$ can be written

$$\frac{\Delta\phi_{s_c}}{\phi_s} = \frac{dn_v(dn_h \sin\theta_c - R\cos\theta_c)}{d^2 n_v^2 + (dn_h \cos\theta_c + R\sin\theta_c)^2}\frac{\Delta\theta_c}{\phi_s}. \tag{104}$$

This relative uncertainty is zero if $n_v = 0$, which means that when perfectly aligned, changing the detector arm angle does not change the azimuthal plane for the center horizontal row of pixels.

In each of Equations (102)-(104), a mathematical discontinuity exists when n_h, n_v, and θ_c all equal zero simultaneously. However, the discontinuities each resolve when the appropriate limits are taken.

Numeric Values.

The uncertainty ΔR arises from imperfect knowledge of the distance between the CCD and material sample. Combining use of a tape measure and camera specifications [69], ΔR rounds up conservatively to 5 mm. The uncertainty Δd arises from imperfect knowledge of pixel size. When Δd exceeds 4×10^{-9} m, the size of the full array would no longer round to any of its listed dimensions, so this value serves as a conservative upper bound. Finally, the uncertainty $\Delta\theta_c$ arises from imperfect knowledge of the absolute angle between the material surface normal and the CCD's position as controlled by rotating the detector arm. For most specular materials, physics dictates that $\theta_s = \theta_i$ at the center of the specular peak, so similar to the original system, θ_c is most easily determined by rotating the detector arm to center the CCD on the specular peak, and then assuming that $\theta_c = \theta_i$. Uncertainty in θ_c can then be traced to uncertainty in θ_i, as well as rotation stage accuracy tolerances. Conservatively, $\Delta\theta_c$ can be estimated at 0.5° [11].

When these numeric values for ΔR, Δd, and $\Delta\theta_c$ are substituted into Equations (99)-(101), the resulting relative uncertainties in θ_s vary from pixel to pixel. For example, when $\theta_c = 20^\circ$, the maximum relative uncertainties within the pixel array are 0.018%, 8.34×10^{-4}%, and 0.35%, respectively. When $\theta_c = 40^\circ$, those maximum values become 0.039%, 0.0018%, and 0.77%, and when $\theta_c = 60^\circ$, those maximum values become 0.080%, 0.038%, and 1.61%, respectively.

When the numeric values for ΔR, Δd, and $\Delta\theta_c$ are substituted into Equations (102)-(104), the resulting relative uncertainties in ϕ_s also vary from pixel to pixel. For

example, when $\theta_c = 20°$, the maximum relative uncertainties within the pixel array are 0.036%, 0.0017%, and 0.056%, respectively. When $\theta_c = 40°$, those maximum values become 0.017%, 8.13×10^{-4}%, and 0.012%, and when $\theta_c = 60°$, those maximum values become 0.012%, 5.81×10^{-4}%, and 0.0042%, respectively.

Uncertainty from Imperfect Alignment.

Even after iteratively applying the alignment process from Section 3.4 to align the CCD with a specular peak, the CCD is likely to possess some combination of rotational and translational misalignment. The uncertainty in each scatter angle due to misalignment will be labeled $\Delta\theta_{s_m}$ and $\Delta\phi_{s_m}$.

Misalignment Formulation.

The CCD's orientation can be described as a rotation applied to the perfectly aligned and projected pixel vectors, defined in Equation (75) relative to the (x, y, z) coordinate axes. Any generic orientation can be expressed as a chained series of three Euler rotations, as long as the axis of the second rotation is orthogonal to both the axes of the first and third rotations [29], but for now the general rotation will be designated simply as $\mathbb{R}_{CCD}$.

Apart from rotational misalignment, the center of the CCD may also be slightly offset from the actual center of the specular peak. In-plane alignment is actuated by detector arm rotation, but out-of-plane alignment is actuated by a vertical linear translation stage. At the measurement location, the CCD still carries the orientation defined by $\mathbb{R}_{CCD}$, which in theory affects the apparent location of pixel offset manifestations. However, for small residual angles following iterative alignment, this particular effect will be ignored. As a result, the Cartesian scatter vectors for each

pixel can be rewritten to include misalignment

$$\vec{r}_s = \mathbb{R}_y(\theta_c + \Delta\theta_{c_m})\,(\mathbb{R}_{CCD}\vec{r}_p + R\hat{\boldsymbol{z}}) + \Delta y\hat{\boldsymbol{y}}. \tag{105}$$

Here, $\Delta\theta_{c_m}$ and Δy represent the in-plane angular offset and out-of-plane translational offset, respectively. If m_h and m_v are the apparent in-plane and out-of-plane pixel offsets from the center of the specular peak, then $\Delta\theta_{c_m} = m_h(9.70^\circ \times 10^{-4})$ and $\Delta y = m_v(5.50\mu\text{m})$, where $9.70^\circ \times 10^{-4}$ is the linear angle subtended by each pixel near the CCD center (as given in Section 3.3) and 5.50μm is the pixel width. The scatter angles θ_s and ϕ_s for each pixel are then computed using the spherical coordinate conversions in Equations (80a) and (80b).

To implement a specific rotation within Equation (105), the general rotation $\mathbb{R}_{CCD}$ is replaced with the Tait-Bryan rotation series $\mathbb{R}_z(\theta_r)\mathbb{R}_y(\theta_y)\mathbb{R}_x(\theta_p)$. The roll, yaw, and pitch misalignment angles θ_r, θ_y, and θ_p can be directly measured and approximated during the CCD alignment process from Section 3.4. Although different rotation series could also sufficiently represent the CCD orientation, this particular order best matches the measurement setup. When alignment procedure motions are modeled by extending Equation (105), this particular choice allows the change in horizontal pixel index to mathematically reach zero when $\theta_y = 0$, and allows the change in vertical pixel index to mathematically reach zero when either $\theta_r = 0$ or $\theta_p = 0$.

Numeric Values.

From the specific camera alignment corresponding to the results in this work, a single example alignment iteration resulted in $\theta_r = 0.11^\circ$, $\theta_y = 0.062^\circ$, and $\theta_p = 0.025^\circ$; these angles remained valid for all subsequent measurements without CCD orientation readjustment. Values for m_h and m_v, however, vary independently for every specific measurement. Perhaps the simplest quantitative way to determine m_h

and m_v is to compare the location of the peak pixel reading to the center of the pixel array.

The absolute uncertainties $\Delta\theta_{s_m}$ and $\Delta\phi_{s_m}$ are then computed as the difference between the nominal values for θ_s and ϕ_s assuming perfect alignment, and the values including misalignment. Relative differences require the scaling used in Equations (99)-(104).

For example, in the broadband metallic mirror measurements with $\theta_i = 20°$ (discussed later in Section 5.1), the peak pixel reading shows $m_h = 3$ and $m_v = 5$. The resulting relative misalignment uncertainties in θ_s and ϕ_s vary with pixel, but the maximum values in this case are 0.0034% and 0.012%, respectively. As another example, in the polished aluminum measurement with $\theta_i = 40°$ (shown in Section 5.2), peak pixel readings show $m_h = -1$ and $m_v = -1$, with maximum relative uncertainties of 0.0049% and 0.0036%, respectively. Finally, for the Kapton® measurement with $\theta_i = 60°$ (presented in Section 5.3), the peak pixel reading shows $m_h = 72$ and $m_v = -3$, with maximum relative uncertainties of 0.23% and 0.0045%, respectively.

Combined Scatter Angle Uncertainty.

In summary, pixel scatter angle uncertainty depends on uncertainty in the distance between material sample and CCD, uncertainty in the angle between detector arm and material surface normal, uncertainty in pixel width, and CCD rotational and translational misalignment. The relative uncertainties can be combined in quadrature as

$$\frac{\Delta\theta_s \sin\theta_s}{\cos\theta_s} = \frac{\sin\theta_s}{\cos\theta_s}\left[\Delta\theta_{s_r}^2 + \Delta\theta_{s_d}^2 + \Delta\theta_{s_c}^2 + \Delta\theta_{s_m}^2\right]^{1/2} \tag{106a}$$

$$\frac{\Delta\phi_s}{\phi_s} = \frac{1}{\phi_s}\left[\Delta\phi_{s_R}^2 + \Delta\phi_{s_d}^2 + \Delta\phi_{s_c}^2 + \Delta\phi_{s_m}^2\right]^{1/2}. \tag{106b}$$

Each term represents an array of values for each individual pixel within a stitched measurement.

4.5 Solid Angle Uncertainty

This section addresses relative uncertainty in the solid angle Ω_d subtended by each pixel during a CCD measurement. As with the original detectors, this uncertainty still depends on uncertainty in pixel dimensions and the distance R, but now accounts for an array of square pixels. Uncertainties are first described assuming perfect alignment, and then a formulation is presented for characterizing how uncertainty in CCD alignment can also impact the solid angles.

Uncertainty with Perfect Alignment.

Equation (86) provides the calculation for Ω_d assuming perfect alignment. As in Section 4.4, pixel dimensions are assumed equal, so that $d_h = d_v = d$.

By using partial derivatives, the relative uncertainty in Ω_d due to the uncertainty ΔR is

$$\frac{\Delta\Omega_{d_R}}{\Omega_d} = \left(\frac{1}{R} - \frac{3R}{d^2(n_h^2 + n_v^2) + R^2}\right)\Delta R, \tag{107}$$

which has a minimum at the center pixel. Similarly, the uncertainty in Ω_d due to the uncertainty Δd can be written

$$\frac{\Delta\Omega_{d_d}}{\Omega_d} = \left(\frac{2R^2 - d^2(n_h^2 + n_v^2)}{dR^2 + d^3(n_h^2 + n_v^2)}\right)\Delta d, \tag{108}$$

which has a maximum at the center pixel.

Uncertainty from Imperfect Alignment.

CCD rotational and translational misalignment can also contribute to solid angle uncertainty. Although the solid angle of each pixel does not depend on θ_c, it does depend on θ_d, defined in Equation (85) as the angle between the pixel normal direction and the pixel scatter vector $\vec{r}_s$. The solid angle with misalignment can be computed

$$\Omega_d \approx \frac{d^2 \cos\theta_d}{|\vec{r}_s|^2} = \frac{d^2(\vec{r}_s|_{\theta_c=0} \cdot \mathbb{R}_{CCD}\hat{\boldsymbol{z}})}{\left|\vec{r}_s|_{\theta_c=0}\right|^3}, \tag{109}$$

where the vector $\vec{r}_s$ is evaluated using Equation (105) with $\theta_c = 0$. The rotational misalignment $\mathbb{R}_{CCD}$ can still be incorporated as the Tait-Bryan rotation from Section 4.4, but the translational misaligmnent offsets m_h and m_v are instead derived from the beam signature. With perfect alignment at $\theta_c = 0$, the pixel normal directions would each match the $\hat{\boldsymbol{z}}$ direction.

The absolute uncertainties $\Delta\Omega_{d_m}$ and $\Delta\Omega_{d_m}$ are then computed as the difference between the nominal values for Ω_d assuming perfect alignment and the values including misalignment. Dividing by the nominal values for Ω_d gives the relative uncertainty.

Numeric Values.

Using the same values for ΔR and Δd from Section 4.4, the maximum relative uncertainty in Ω_d due to the uncertainty ΔR is 3.08%, while the maximum relative uncertainty in Ω_d due to the uncertainty Δd is 0.15%. Then, using the same rotational misalignment angles from Section 4.4, and beam signature translational misalignment offset $m_x = -1$ and $m_y = -1$, the largest relative uncertainty in Ω_d due to misalignment is 0.012%.

Combined Solid Angle Uncertainty.

In summary, pixel solid angle uncertainties depend on uncertainties in the distance between material sample and CCD, pixel width, and CCD rotational and translational misalignment. The relative uncertainties can be combined in quadrature as

$$\frac{\Delta\Omega_d}{\Omega_d} = \frac{1}{\Omega_d}\left[\Delta\Omega_{d_R}^2 + \Delta\Omega_{d_d}^2 + \Delta\Omega_{d_m}^2\right]^{1/2}. \tag{110}$$

Each term represents an array of values for each individual pixel within a stitched frame.

4.6 Total Uncertainty

The total relative measurement uncertainty can now be calculated by substituting the combined scatter flux, incident flux, scatter angle, and solid angle relative uncertainty terms into Equation (71). The results are applied to CCD measurement data and compared to original CASI® uncertainty analysis.

Array Average Uncertainties.

Table 5 compiles relative uncertainty statistics across the entire pixel array for two different specular peak measurements, demonstrating how the total uncertainty and each contribution change with both incident angle and ND filter uncertainty. The left half displays uncertainty results for normal incidence and $\mathrm{OD}_m = \mathrm{OD}_b$, when both θ_c and $\Delta\Phi_{\mathrm{OD}}/\Phi_{\mathrm{OD}}$ are zero. These conditions apply, for example, when converting beam signatures directly into BRDF values. The right half then demonstrates uncertainty results with $\theta_i = 60°$, $\mathrm{OD}_b = 5.2$, and $\mathrm{OD}_m = 3.5$, which corresponds to $\theta_c = 60°$ and $\Delta\Phi_{\mathrm{OD}}/\Phi_{\mathrm{OD}} = 59.7\%$ with worst-case OD uncertainty. These conditions apply, for example, to the Kapton® specular peak measurements shown in Section 5.3.

The bottom row compares total relative uncertainty between the cases when OD uncertainty is totally mitigated.

In general, Table 5 shows several key features. First, depending on the ND filters used, worst-case OD uncertainty can easily provide the largest source of uncertainty in the BRDF calculation. However, like the other incident flux uncertainties, this term is applied uniformly to every pixel, and so does not affect the relative shape of the BRDF across a single stitched frame. On average, solid angle uncertainty provides the second largest source of relative uncertainty. For the original CASI® detectors, the smallest aperture carried approximately 2% relative uncertainty [13], slightly less than the 3% relative uncertainty for each CCD pixel. On average, pixel non-linearity provides the third largest source of relative uncertainty, just above 2%, although a small number of outliers possess up to 16%. Scatter angle relative uncertainty contributions increase with θ_s, as expected from the original analysis [13], up to an average of approximately 1.5% near 60°.

Table 5. Total BRDF relative uncertainty and contributing terms for two specular CCD measurements, compiled as array-wide average, standard deviation, maximum, and minimum values, in percentage [%]. The left half corresponds to normal incidence with $\mathbf{OD}_m = \mathbf{OD}_b$. The right half corresponds to $\theta_s = 60°$ with $\mathbf{OD}_b = 5.2$ and $\mathbf{OD}_m = 3.5$. The bottom row demonstrates the impact of OD uncertainty mitigation.

	$\theta_i = 0°$				$\theta_i = 60°$			
	Avg	Std Dev	Max	Min	Avg	Std Dev	Max	Min
$\frac{\Delta f_r}{f_r}$	3.93	0.300	16.6	3.41	59.8	0.0211	61.9	59.8
$\frac{\Delta \Phi_s}{\Phi_s}$	2.18	0.502	16.3	1.05	2.18	0.502	16.3	1.05
$\frac{\Delta \Phi_i}{\Phi_i}$	1.01	0	1.01	1.01	59.7	0	59.7	59.7
$\frac{\Delta \theta_s \sin \theta_s}{\cos \theta_s}$	0.0122	0.00703	0.0244	0	1.53	0.0569	1.63	1.43
$\frac{\Delta \Omega_d}{\Omega_d}$	3.08	0.00122	3.08	3.07	3.08	0.00122	3.08	3.07
$\frac{\Delta f_r}{f_r}\Big\vert_{\frac{\Delta \Phi_{\mathrm{OD}}}{\Phi_{\mathrm{OD}}}=0}$	3.93	0.300	16.6	3.41	4.22	0.282	16.7	3.72

According to these numbers, the easiest way to reduce total relative uncertainty would be to mitigate OD uncertainty by independently characterizing each ND filter rather than relying on broad published production tolerances. In addition, differences in pixel linearity could be software corrected to an average response, and outlier pixels could be selectively ignored.

Specific Pixel Uncertainties.

Finally, Table 6 displays total relative uncertainty results for several specific in-plane scatter angles as part of two additional specular peak CCD measurements. Here, $\theta_i = 20°$ and $40°$ are chosen to match Butler's analysis using original CASI® measurements at these angles [11]. For the $\theta_i = 20°$ case, $\mathrm{OD}_b = 5.2$ and $\mathrm{OD}_m = 5.0$ are chosen to mimic the broadband mirror measurements in Section 5.1, where $\Delta\Phi_{\mathrm{OD}}/\Phi_{\mathrm{OD}} = 2.30\%$ in the worst-case. For the $\theta_i = 40°$ case, $\mathrm{OD}_b = 5.2$ and $\mathrm{OD}_m = 4.1$ are chosen to mimic the polished aluminum measurements in Section 5.2, where $\Delta\Phi_{\mathrm{OD}}/\Phi_{\mathrm{OD}} = 14.2\%$ in the worst-case. The in-plane angles are written as deviations from specular, or $\theta_s - \theta_i$, and then matched to appropriate pixels in the CCD's center horizontal row. For the sake of comparison, total relative uncertainty is also presented when OD uncertainty is completely mitigated.

In the original analysis, out-of-plane aperture misalignment comprised the largest portion of relative uncertainty nearest the specular peak – up to 12% out of 17% total uncertainty [13, 11]. However, this contribution diminished monotonically away from the specular peak. Total uncertainties reduced to a mininum of 7.5% somewhere between $\theta_s - \theta_i = 0.5°$ and $1.0°$, before increasing again due to scatter angle relative uncertainty contributions [13, 11]. The out-of-plane term no longer applies to the CCD, as described in Section 4.2, and as a result, the total uncertainty values no longer increase so dramatically approaching the specular peak. Instead, individual

Table 6. Total BRDF relative uncertainty for two specular CCD measurements, reported from individual pixels corresponding to specific in-plane specular offset angles ($\theta_s - \theta_i$). Values are given as percentages [%], with separate columns including and omitting ND filter uncertainty. On the left half, $\theta_i = 20°$, $\mathbf{OD}_b = 5.2$, and $\mathbf{OD}_m = 5.0$. On the right half, $\theta_i = 40°$, $\mathbf{OD}_b = 5.2$, and $\mathbf{OD}_m = 4.1$.

$\theta_s - \theta_i$	$\theta_i = 20°$		$\theta_i = 40°$	
	$\frac{\Delta f_r}{f_r}\Big\vert_{\frac{\Delta\Phi_{OD}}{\Phi_{OD}}=2.30\%}$	$\frac{\Delta f_r}{f_r}\Big\vert_{\frac{\Delta\Phi_{OD}}{\Phi_{OD}}=0}$	$\frac{\Delta f_r}{f_r}\Big\vert_{\frac{\Delta\Phi_{OD}}{\Phi_{OD}}=14.2\%}$	$\frac{\Delta f_r}{f_r}\Big\vert_{\frac{\Delta\Phi_{OD}}{\Phi_{OD}}=0}$
0.011°	5.05	4.50	14.9	4.54
0.022°	4.45	3.81	14.7	3.86
0.05°	4.36	3.70	14.7	3.76
0.1°	4.38	3.73	14.7	3.79
0.5°	4.24	3.57	14.7	3.63
1.0°	4.83	4.24	14.8	4.30

pixel non-linearity and OD uncertainty largely determine how CCD uncertainties compare to the original CASI®. When a pixel's non-linearity is near the array's average, and when OD uncertainty is low, then overall CCD uncertainty is similar or even less than the original CASI® [13, 11]. When either non-linearity or OD uncertainty is relatively high, then the overall CCD uncertainty eclipses the original values.

Comparison to Original CASI®.

Figure 21 offers a visualization by overlaying the total relative uncertainty bounds onto an in-plane slice of the beam signature CCD measurement data. When BRDF values are shown on a log scale over the full dynamic range, the uncertainty bounds are difficult to visually differentiate from the measurement data, as long as the OD uncertainty remains negligible. For comparison, beam signature measurement data from the original CASI® detector is also overlaid. It is important to note that due to the difference in the distance R, the beam must be refocused when switching between

the CCD and original detector, so a perfect match is unrealistic. Nevertheless, there is quite good agreement near the specular peak, both in terms of maximum value, beam width, and beam shape.

As expected, the CCD lacks the dynamic range of the original system, especially within a single stitched frame, but it does possess higher spatial resolution. In addition, the CCD detects two potentially undesirable features which the original detectors do not. First, high-frequency diffractive noise is noticeable in Figure 21(b). Second, the CCD registers several sub-peaks, also shown in the beam signature results in Section 3.8. However, as shown in Figure 21, the uncertainty bounds and detector noise analysis conducted in this work are not wide enough to explain or absorb either characteristic. Pending further investigation, these features may arise from stray light from this particular camera's protective IR blocking filter or the ND filters. For instance, the diffractive noise may be explained as scatter from particles on imperfectly clean filters, and the sub-peaks may arise from multiple reflections at the filter interfaces. Unlike the original detectors, the CCD does not incorporate a lens, and so even though stray light may exist within the original detector optics, the CCD allows stray signals to spatially register on different pixels.

Further investigation of these artifacts will be left to future work. In particular, measurements taken while successively slewing the CCD away from the center of the specular peak may provide further insight and mitigation of the sub-peaks. For now, though, data analysis can still be performed by filtering out such features. In particular, since the sub-peaks are still more than 4.8 orders of magnitude below the main peak, an adjusted noise floor can easily be implemented, as shown in Figure 21(a).

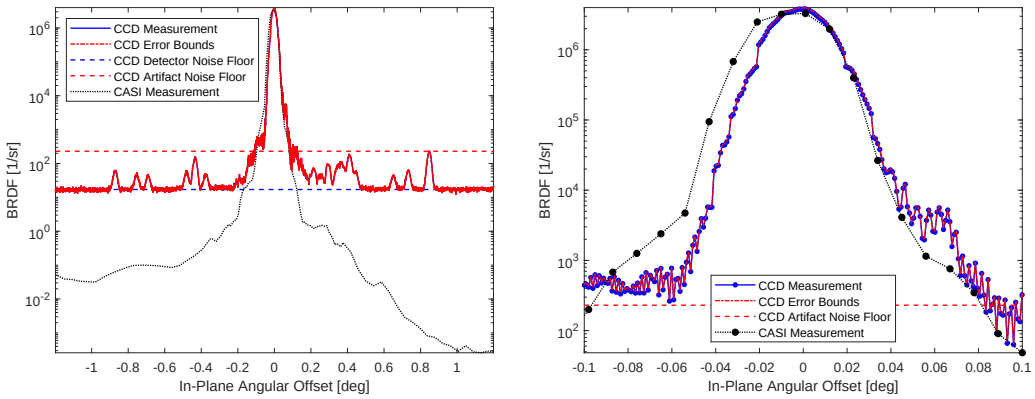

Figure 21. Plots of beam signature measurement data using a 15 mW red HeNe laser source. CCD measurements were collected as one stitched frame using 1, 10, 100, and 1000 ms exposures with 5.2 OD. In-plane pixel results, uncertainty bounds, and noise floors based on both inherent detector noise and measurement artifacts are shown. In-plane CASI® measurements using the appropriate original detector are shown in black. The full CCD angular extent is plotted in (a), with zoom near the specular peak in (b)

4.7 Uncertainty Summary

In summary, the out-of-plane aperture misalignment term, which had previously served as the dominant uncertainty source for near-specular measurements, was no longer necessary as a source of scatter flux uncertainty. Detector non-linearity and incident flux temporal fluctuation both demanded reassessment, scatter angle and solid angle relative uncertainty expressions each required new analytical derivations, and detector noise limits needed reevaluation. In addition, new terms were devised to account for optical density uncertainty and CCD misalignment.

Ultimately, the largest uncertainty term was shown to be OD uncertainty in certain cases, although it varied from 0 to almost 60%, depending on the ND filters used for different measurements and their known tolerances. Solid angle uncertainty was the second largest contributor, with relative uncertainties slightly larger than those in the original analysis, consistently near 3%. On average, detector non-linearity

was the third largest term, just above 2% relative uncertainty, although a very small number of outlier pixels possess up to 16%. Scatter angle uncertainty increases with θ_s up to approximately 1.5% near $\theta_s = 60°$. When OD uncertainty is negligible, the typical total relative uncertainties for nearly any scatter angle are in the vicinity of 4%, compared to minimum uncertainties near 2% in Cady's analysis [13] or 7.5% in Butler's analysis [11].

Finally, the CCD sacrifices nearly two-thirds of the dynamic range of the original CASI® when making measurements centered on the specular peak, but gains almost ten times greater spatial resolution. Although beam signature CCD measurements agree well with equivalent CASI® in-plane data, the CCD encounters two potentially undesirable artifacts: 1) high-frequency diffractive noise, and 2) multiple sub-peaks. The uncertainty bounds and noise analysis from this work are not wide enough to explain or absorb either characteristic, but due to the relatively small impact from each, they can be filtered prior to further data analysis.

4.8 Next Steps

Now that the CCD-augmented measurement system's uncertainties have been robustly characterized and quantified, and even applied to several pertinent material measurement cases, Chapter V will present and discuss out-of-plane measurement data for a broadband mirror, polished aluminum, Kapton®, and solar cell material samples.

V. Material Measurement Results

This section presents BRDF measurements of four different specular materials using the CCD-augmented CASI® with a 15 mW helium-neon laser source at 632.8 nm. The material samples include a broadband metallic front-surface reflecting laboratory mirror, a circularly polished aluminum disk, an unwrinkled sheet of Kapton®, and a commercially available small satellite solar cell. Each material was measured at incident angles of 20°, 40°, and 60°. Due to occlusion of the source by the detector, 20° was selected as the lower limit for incident angle; due to material sample mount grazing limitations, 60° was selected as the upper limit; and 40° provided an incident angle in between. However, for the sake of conciseness, this chapter presents the broadband mirror results only for $\theta_i = 20°$, the polished aluminum results only for $\theta_i = 40°$, and the Kapton® results only for $\theta_i = 60°$. The remaining results for those materials are placed in the Appendix. Due to the complexity of its out-of-plane behavior, the solar cell results are presented at various orientations and incident angles.

Images of the mirror, aluminum, and Kapton® samples are shown in Figure 22, and an image of the illuminated portion of the solar cell is shown in Figure 23. In particular, since Kapton® is partially transparent, care was taken to allow transmitted light to pass into a beam dump in order to isolate and measure the reflected light. The other three materials were opaque with negligible transmission.

After aligning and calibrating the system according to Sections 3.3 and 3.4, the laser source beam signature was measured without a material sample in place, corresponding to the beam signature results presented in Section 3.8. Following the beam signature collection, each material was mounted to the CASI® sample stage in succession and measured at each of the three incident angles. Using the method described in Section 3.6, data from four different exposure times (1ms, 10ms, 100ms, and 1s) were scaled and stitched together.

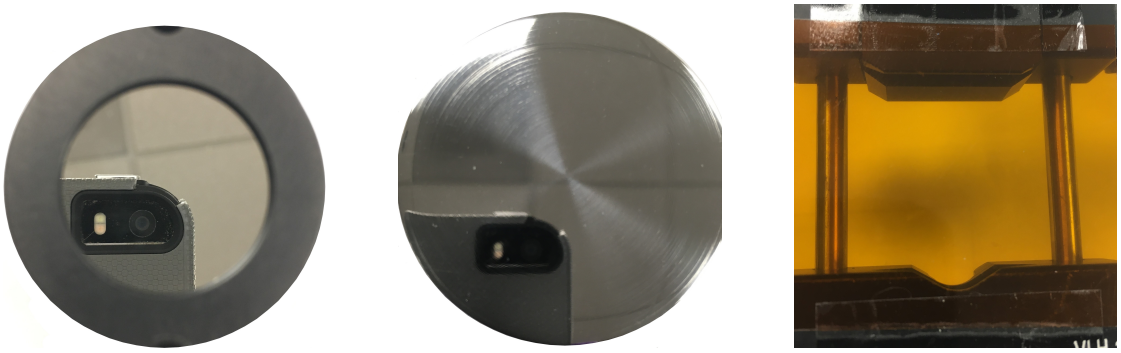

(a) (b) (c)

Figure 22. Images of three specular material samples: broadband metallic laboratory mirror (a), circularly polished aluminum disk (b), and Kapton® sheet (c). The mirror and aluminum were photographed at angles where the reflection of the phone camera was visible, demonstrating their specular qualities.

For each material measurement at each incident angle, every pixel's scatter flux reading was converted to a BRDF value, using the process described in Section 3.8. Incident flux Φ_i was calculated as the sum of every stitched pixel readings across the entire beam signature (after subtracting off background noise), and adjusted according to Equation (87) based on the OD required to just keep each measurement below the pixel saturation limit. The scatter angles θ_s and ϕ_s and the solid angles Ω_d were calculated for each pixel according to Equations (80a), (80b), and (86), respectively, using the nominal values $d_h = d_v = 5.5 \times 10^{-6}$ μm and $R = 0.325$ m. Each measurement was centered on the specular peak, so θ_c was set to θ_i for each case. Scatter flux Φ_s was simply taken as the sDC reading from every individual pixel separately. The raw measurements were finally converted to BRDF by substituting θ_s, Ω_d, Φ_i, and Φ_s into Equation (45), and BRDF values over the entire pixel array were plotted as scaled color-scaled arrays.

For each measurement, it was also possible to use Equations (82a)–(83b) to generate contours of constant θ_s and ϕ_s for overlay onto the BRDF measurement plots. Each measurement frame contains some range of θ_s and ϕ_s values. Contours of con-

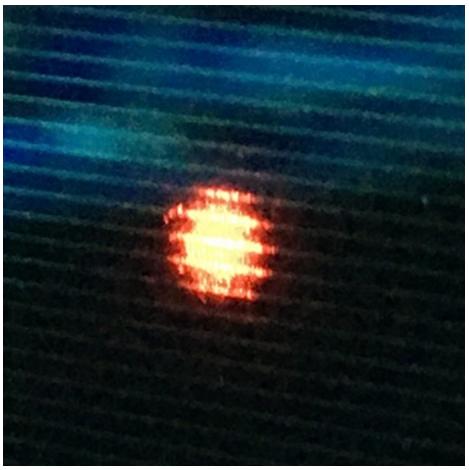

Figure 23. Image of the solar cell material surface, including the illuminated laser beam spot. In particular, the metal conducting bars, which are separated by approximately 800 μm are visible running in one direction across the solar cell surface.

stant θ_s could be generated by choosing desired θ_s values within the range of a frame, and then calculating n_h and n_v across the frame's full range of ϕ_s values. Likewise, contours of constant ϕ_s could be generated by choosing desired ϕ_s values, and then calculating n_h and n_v across the frame's full range of θ_s values.

5.1 Broadband Mirror

The broadband mirror BRDF results for $\theta_i = 20°$ are displayed in Figure 24. The mirror surface was assumed to possess consistent surface characteristics throughout, so that placement of the illuminating laser spot did not require consideration. As should be expected for a highly specular material, the reflected pattern looks remarkably similar to the beam signature in Figure 20, only flipped horizontally during the process of reflection [38].

The peak BRDF value reaches 2.50×10^6 sr^{-1}, which is less than the peak value for the beam signature, but of the same order of magnitude. The measurement results for incident angles of 40° and 60° are displayed in Appendix 1.1, but the peak values

at those angles are 3.19×10^6 sr^{-1} and 5.09×10^6 sr^{-1}, respectively. Since Fresnel reflectance generally increases with incident angle [38], the increasing peak values are expected.

When $\theta_i = 20°$, the measurement geometry requires $\theta_c = 20°$. In Figure 24(c), the contours of constant θ_s are still plotted in 0.5° increments, but as expected, they appear much more vertical (although still slightly curved). The contours of constant ϕ_s are plotted here in 1° increments; at this geometry, the array now contains less than 8° of ϕ_s radials on the left and slightly more than 6° of ϕ_s radials on the right. Table 7, whose format matches Table 4, displays the range of θ_s and ϕ_s values found within the pixel array, given in degrees.

Although more detailed quantitative analysis regarding anisotropicity is saved for other work, the broadband metallic mirror provides a solid baseline for isotropic reflectance, as demonstrated by the qualitative symmetry observed about its specular peak.

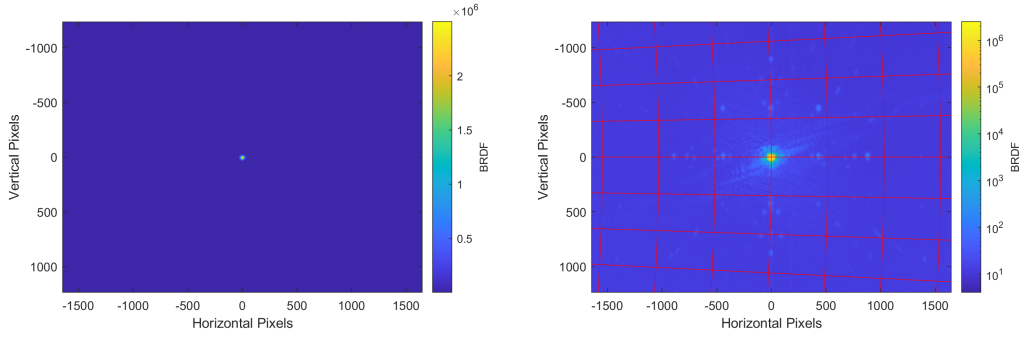

Figure 24. Plots of the broadband mirror BRDF measurement data for $\theta_i = 20°$ using a linear scale in (a) and logarithmic scale in (b), including an overlay with contours of constant θ_s and ϕ_s in 0.5° and 1° increments, respectively, in (b). The reflected pattern appears very similar to the beam signature in Fig. 20, but flipped, which should be expected for a highly specular surface with isotropic surface characteristics. Here $\theta_c = 20°$, and the contours of constant θ_s appear largely vertical but slightly curved, and the full array contains nearly 8° of ϕ_s radials on the left and slightly more than 6° of ϕ_s radials on the right.

Table 7. Scatter angles (θ_s, ϕ_s) for select CCD pixels spanning the full array when $\theta_c = 20^\circ$ in the augmented CASI® system. Angles are curtailed at four significant figures for simplicity and given in degrees. The center cell corresponds to the center pixel $(n_h, n_v) = (0, 0)$, the top-left cell corresponds to the top-left pixel $(n_h, n_v) = (-1647, -1235)$, the bottom-right cell corresponds to the bottom-right pixel $(n_h, n_v) = (1648, 1236)$, and so on.

$(18.44, 176.2)$	$\cdots$	$(20.03, 176.5)$	$\cdots$	$(21.63, 176.8)$
$\vdots$	$\ddots$	$\vdots$	$\iddots$	$\vdots$
$(18.40, 180)$	$\cdots$	$(20, 180)$	$\cdots$	$(21.60, 180)$
$\vdots$	$\iddots$	$\vdots$	$\ddots$	$\vdots$
$(18.44, 183.8)$	$\cdots$	$(20.03, 183.5)$	$\cdots$	$(21.63, 183.3)$

5.2 Polished Aluminum

Unlike the mirror with relatively consistent surface characteristics, the aluminum sample possesses circular grooves imparted during the polishing process which are visible even to the naked eye, as in Figure 22(b). The diameter of the illumination spot is approximately 5 mm, while the diameter of the aluminum sample is approximately 5 cm. Thus, the orientation of the grooves are relatively consistent within illumination spots sufficiently far from the sample center. However, changes to the spot location also change the orientation of the illuminated grooves relative to the plane of incidence.

BRDF data are displayed in Figure 25 when $\theta_i = 40^\circ$ for one selected illumination spot location (sufficiently far from the sample center). At this incident angle, the peak BRDF value reaches 4.57×10^5 sr^{-1}. Measurement results for the same spot location at incident angles of 20° and 60° are displayed in Appendix 1.2. The peak values at those angles are 3.49×10^5 sr^{-1} and 1.36×10^6 sr^{-1}, respectively, roughly an order of magnitude smaller than the beam signature and broadband mirror values, indicating

a slightly less specular material. Unlike the mirror, though, whose isotropic surface characteristics produced a specular peak with a qualitatively symmetric shape, the aluminum sample produces a specular peak with a qualitatively asymmetric shape due to anisotropic surface characteristics within the illuminated spot. Again, more detailed quantitative analysis regarding anisotropicity is saved for other work.

Since this sample's surface characteristics change significantly on scales larger than the illumination spot size, the results from a single spot cannot necessarily be extrapolated over the rest of the surface. In fact, due to the overall circular surface pattern, if this entire sample was illuminated simultaneously, or if enough locations were measured independently, it is plausible that the anisotropic reflectance patterns from each individual spot would average into a larger overall isotropic pattern. Nonetheless, these single-spot results demonstrate the augmented CASI®'s ability to directly capture anisotropic specular BRDF data for materials whose surface characteristics within approximately 5mm are representative of the entire surface.

When $\theta_i = 40°$, the measurement geometry requires $\theta_c = 40°$. In Figure 25(b), the contours of constant θ_s and ϕ_s are once again plotted in 0.5° and 1° increments, respectively. As expected, the θ_s contours appear more vertical and less curved than their counterparts when $\theta_c = 20°$, and fewer ϕ_s radials (approximately 4°) are contained within the frame. Table 8 displays the range of θ_s and ϕ_s values found within the pixel array, given in degrees, following the format of Tables 4 and 7.

Overall, the circularly polished aluminum provides a useful example of localized anisotropic reflectance, whose data can be used for further study of anisotropic BRDF characterization.

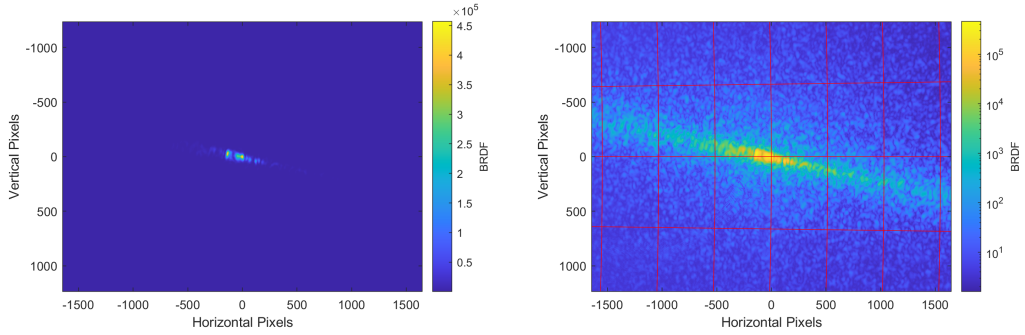

(a) **(b)**

Figure 25. Plots of the polished aluminum BRDF measurement data for $\theta_i = 40°$ using a linear scale (a) and logarithmic scale (b), including an overlay with contours of constant θ_s and ϕ_s in $0.5°$ and $1°$ increments, respectively, in (b). The specular peak appears qualitatively asymmetric when compared to the beam signature and mirror, which should be expected with visibly anisotropic grooves on the surface. Here $\theta_c = 40°$, so the θ_s contours appear more vertical and less curved than their counterparts when $\theta_c = 20°$, and fewer ϕ_s radials (approximately $4°$) are contained within the frame.

Table 8. Scatter angles (θ_s, ϕ_s) for select CCD pixels spanning the full array when $\theta_c = 40°$ in the augmented CASI® system. Angles are curtailed at four significant figures for simplicity and given in degrees. The center cell corresponds to the center pixel $(n_h, n_v) = (0, 0)$, the top-left cell corresponds to the top-left pixel $(n_h, n_v) = (-1647, -1235)$, the bottom-right cell corresponds to the bottom-right pixel $(n_h, n_v) = (1648, 1236)$, and so on.

$(38.42, 178.1)$	$\cdots$	$(40.01, 178.1)$	$\cdots$	$(41.6, 178.2)$
$\vdots$	$\ddots$	$\vdots$	$\iddots$	$\vdots$
$(38.40, 180)$	$\cdots$	$(40, 180)$	$\cdots$	$(41.60, 180)$
$\vdots$	$\iddots$	$\vdots$	$\ddots$	$\vdots$
$(38.42, 181.9)$	$\cdots$	$(40.02, 181.9)$	$\cdots$	$(41.61, 181.8)$

5.3 Kapton®

As previously mentioned, the Kapton® sheet is partially transparent, so care was taken during mounting to ensure that transmitted light did not reflect from other

surfaces back through the Kapton® and interfere with measurements. In addition, although the Kapton® holds its own shape well enough to avoid crumpling or wrinkling without intentional external force, it is flexible enough to bow easily under its own weight without vertical support. As shown in Figure 22, scotch tape was used to secure the edges and gently pull the sample taut. Unlike the polished aluminum sample, the Kapton's® surface characteristics are difficult to evaluate with the naked eye.

BRDF data are displayed in Figure 26 from one selected spot in the center of the sample when $\theta_i = 60°$. At this incident angle, the peak BRDF value reaches 1.63×10^5 sr^{-1}. Measurement results for the same spot location at incident angles of 20° and 40° are displayed in Appendix 1.3. The peak values at those angles are 1.85×10^4 sr^{-1} and 2.50×10^4 sr^{-1}, respectively, roughly an order of magnitude smaller than the polished aluminum and two orders of magnitude smaller than the beam signature and broadband mirror values.

Like the polished aluminum, the Kapton® at this spot produces a specular peak with a qualitatively asymmetric shape. However, without more detailed measurement and analysis of the entire surface, it is not immediately obvious whether the asymmetric peak is due to consistently anisotropic surface characteristics or an imperfectly flat sample. Also interestingly, the Kapton® appears to reflect a more evenly diffuse pattern surrounding the specular peak. As a partially transparent polyimide film [21], Kapton® may exhibit significant volumetric scattering, which is also worth further exploration. Nonetheless, these initial results demonstrate the augmented CASI®'s ability to directly capture BRDF data from asymmetrically-shaped specular peaks, reflected by materials with potentially anisotropic surface characteristics.

When $\theta_i = 60°$, the measurement geometry requires $\theta_c = 60°$. In Figure 26(b), the contours of constant θ_s and ϕ_s are once again plotted in 0.5° and 1° increments,

respectively. As expected, the θ_s contours appear even more vertical and less curved than their counterparts when $\theta_c = 40°$, and even fewer ϕ_s radials (less than 3°) are contained within the frame. Table 9 displays the range of θ_s and ϕ_s values found within the pixel array, given in degrees, following the format of Tables 4, 7, and 8. At this geometry, ϕ_s values do not vary within four significant digits across the pixel rows.

Overall, the unwrinkled Kapton® sheet provides another useful example of anisotropic specular reflectance, whose data can be used for further study of anisotropic BRDF characterization.

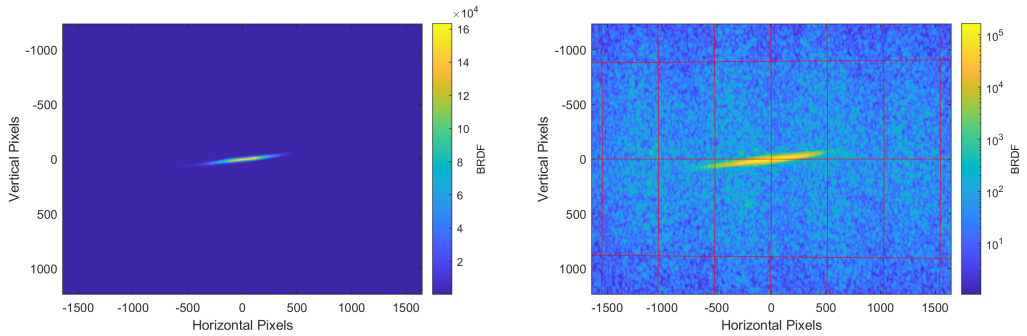

(a) **(b)**

Figure 26. Plots of the Kapton® BRDF measurement data for $\theta_i = 60°$ using a linear scale (a) and logarithmic scale (b), including an overlay with contours of constant θ_s and ϕ_s in $0.5°$ and $1°$ increments, respectively, in (b). The specular peak appears qualitatively asymmetric when compared to the beam signature and mirror. Here $\theta_c = 60°$, so the θ_s contours appear even more vertical and less curved than their counterparts when $\theta_c = 40°$, and fewer ϕ_s radials (less than $3°$) are contained within the frame.

Table 9. Scatter angles (θ_s, ϕ_s) for select CCD pixels spanning the full array when $\theta_c = 60^\circ$ in the augmented CASI® system. Angles are curtailed at four significant figures for simplicity and given in degrees. The center cell corresponds to the center pixel $(n_h, n_v) = (0, 0)$, the top-left cell corresponds to the top-left pixel $(n_h, n_v) = (-1647, -1235)$, the bottom-right cell corresponds to the bottom-right pixel $(n_h, n_v) = (1648, 1236)$, and so on.

$(58.41, 178.6)$	$\cdots$	$(60.01, 178.6)$	$\cdots$	$(61.60, 178.6)$
$\vdots$	$\ddots$	$\vdots$	$\iddots$	$\vdots$
$(58.40, 180)$	$\cdots$	$(60, 180)$	$\cdots$	$(61.60, 180)$
$\vdots$	$\iddots$	$\vdots$	$\ddots$	$\vdots$
$(58.41, 181.4)$	$\cdots$	$(60.01, 181.4)$	$\cdots$	$(61.60, 181.4)$

5.4 Solar Cell BRDF Measurements

The solar cell obtained for this study consists of periodically-spaced metal conducting bars mounted atop triple-junction photovoltaic absorption layers with an epoxy-mounted coverglass. According to production specifications, the metal bars are approximately 10 μm wide and spaced approximately 800 μm apart, running in one direction along the solar cell surface. Even with the beam focused at the pixel array, the sample's illumination spot was large enough to encompass multiple metal bars.

Metal Bars Oriented In-Plane.

Figure 27 shows BRDF measurement results from one particular illumination spot when the solar cell is mounted with the metal bars aligned with the in-plane (horizontal) direction. Figures 27(a) and 27(c) display the entire pixel array of BRDF measurements for $\theta_i = 20^\circ$ and $\theta_i = 60^\circ$, respectively, which simultaneously include both in-plane and out-of-plane data centered on the specular direction.

Even qualitatively, three distinct reflectance features are distinguishable: 1) one specular peak centered in the frame, 2) a second specular peak offset from the first, and 3) a vertical diffraction pattern oriented in the out-of-plane direction. Figures 27(b) and 27(d) extract BRDF values from the pixel columns running vertically (out-of-plane) through the center of each specular peak in Figures 27(a) and 27(c). At both incident angles, the diffraction pattern signal is well above any detector and artifact noise levels, and therefore caused by solar cell surface features. However, for larger θ_i, as in Figure 27(c), the diffraction pattern begins to curve noticeably in shape, appearing less vertically straight. It is worth mentioning that the difference in diffraction peak magnitudes evident between the left and right sides of Figure 27(d) arise only because the solar cell metal bars are not oriented perfectly in-plane, and so the center vertical pixel column does not follow the measured diffraction pattern perfectly. In reality, the peak values match near each edge of the CCD detector.

Measurement uncertainty was calculated according to Chapter IV, which identified neutral density (ND) filter uncertainty as the largest contributor. The measurement for $\theta_i = 20°$ required ND filters with a combined optical density (OD) of $\text{OD}_m = 3.3$, while the measurement for $\theta_i = 60°$ required an increase to $\text{OD}_m = 4.0$ in order to handle the higher scatter flux at that angle. For $\text{OD}_m = 3.3$, none of the stacked ND filters matched those used for the beam signature, and so the worst-case ND filter uncertainty based on published tolerances was 59.3%. For $\text{OD}_m = 4.0$, however, the same 4.0 OD filter was also used in the beam signature, and so the worst-case ND filter uncertainty was 14.0%.

It is important to note that unlike many other uncertainty contributions, ND filter uncertainty affects each pixel's BRDF measurement uniformly, and so it does not impact the relative shape of the BRDF. When ND filter uncertainty is omitted from the overall uncertainty calculation, the average relative uncertainty considering

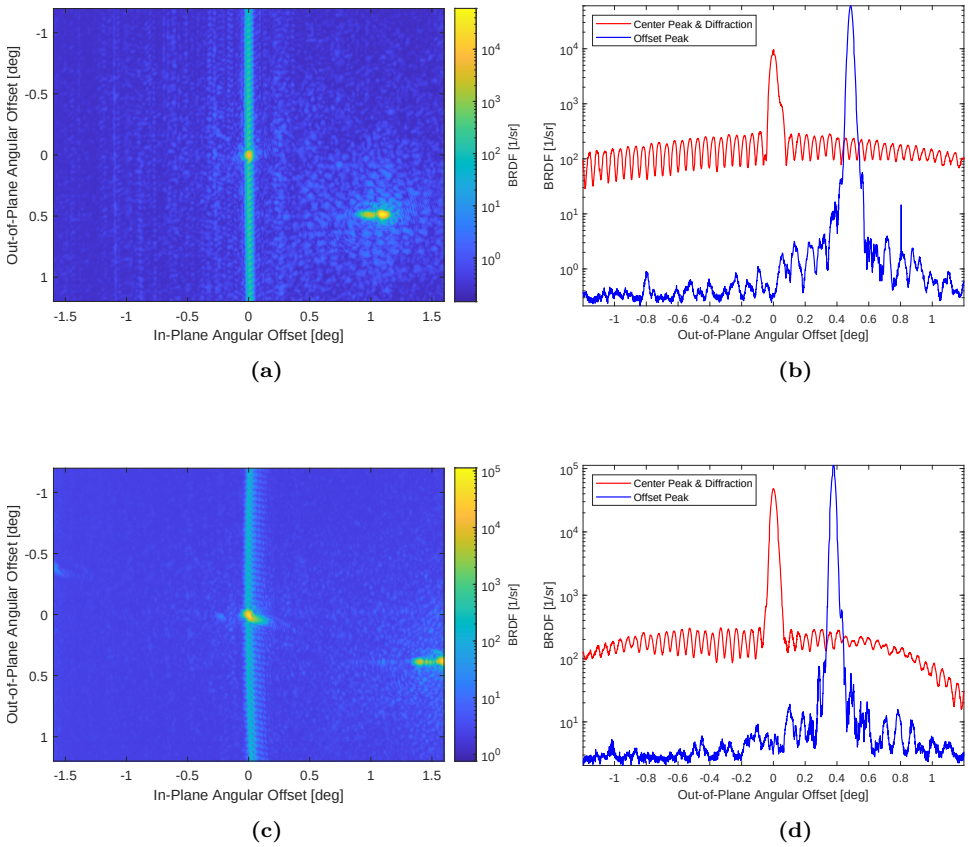

Figure 27. Plots of solar cell BRDF measurement data using a 15 mW red HeNe laser source with metal conducting bars oriented in-plane, where $\theta_i = 20°$ in (a) and (b), and $\theta_i = 60°$ in (c) and (d). The full CCD pixel arrays in (a) and (c) capture three distinct reflectance features, which include a central specular peak, an offset specular peak, and a diffraction pattern. The pixel column readings through the center of each peak, plotted in (b) and (d), show that each feature lies well above the noise floor.

all other contributions across all pixels for the $\theta_i = 20°$ measurement in Fig. 27(a) is only 4.00% with a standard deviation of 0.29%. For the $\theta_i = 60°$ measurement in Figure 27(c), the average relative uncertainty is 6.42% with a standard deviation of 0.24%.

Metal Bars Oriented Out-of-Plane.

Fourier optics teaches that diffraction through rectangular apertures results in far field irradiance patterns with sinc^2 spacing between high-frequency peaks [30]. More details involving specific diffraction model construction and numerical parameter selection are given in Sections 6.3 and 6.4, but the high-frequency pattern displayed in Figure 27 corresponds very well to the diffraction expected through rectangular apertures whose dimensions match the solar cell's conducting bars. It is thus possible to deduce that the diffraction pattern noticeable in the BRDF measurement is caused by the solar cell's periodically spaced metal bars.

As a result, changing the orientation of the bars by rotating the solar cell about its surface normal should cause a corresponding change in diffraction pattern orientation. Figure 28 compares measurements at $\theta_i = 40°$ with the metal bars oriented approximately 45° out-of-plane in (a) and fully out-of-plane in (b). The illumination spot on the solar cell is the same for both cases, although slightly different than the spot used in Figure 27. As expected, the diffraction pattern orientation changes with solar cell orientation.

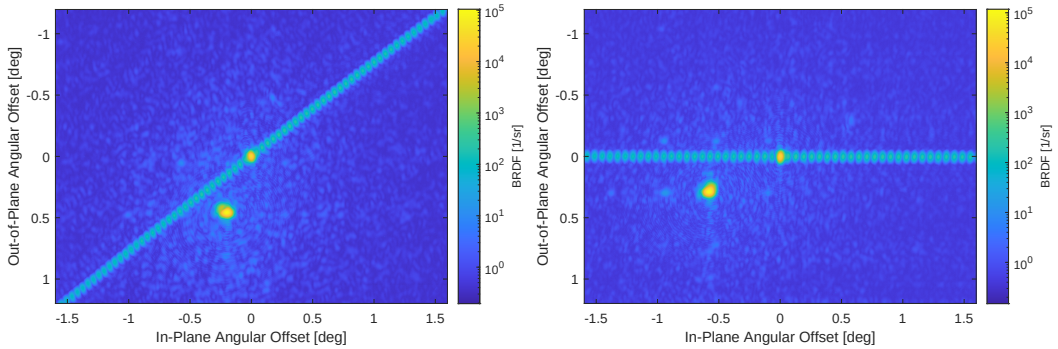

Figure 28. Plots of solar cell BRDF measurement data using a 15 mW red HeNe laser source and $\theta_i = 40°$, with the metal conducting bars oriented 45° out-of-plane in (a) and fully out-of-plane in (b). Both the diffraction pattern and the offset specular peak rotate about the center specular peak along with the solar cell.

No matter how the solar cell is oriented, one specular peak always appears aligned with the center of the diffraction pattern. This peak is plausibly linked to the photovoltaic material beneath the metal bars, indicating that these two materials have very similar surface normal directions. The second specular peak, however, is very clearly offset from the first peak. Its apparent location rotates about the center peak as the solar cell rotates, and even shifts location slightly as the illumination spot changes. In addition, when a white sheet of paper is slowly advanced from the CCD to the sample stage (taking advantage of the visible laser source), the apparent spacing between the two peaks gradually shrinks. The combination of these behaviors indicates that the second specular peak is caused by another material whose surface normal points in a slightly different direction. The coverglass for this particular solar cell was manually affixed with epoxy, with slightly uneven or offset applications possible, making it a plausible candidate for the cause of the second peak.

Interestingly, when the illumination spot location and metal bar orientation are fixed, the apparent orientation of the diffraction pattern also changes as θ_i increases. In fact, both the diffraction pattern and the offset specular peak measurements seem to compress in the out-of-plane direction. Figures 29(a) and 29(b) demonstrate this phenomenon for one particular illumination spot and solar cell orientation when $\theta_i = 20°$ and $\theta_i = 60°$, respectively. This phenomenon will be addressed within the diffraction model presented in Sec. 6.3.

In-Plane Comparison to CASI®.

Lastly, with the diffraction pattern oriented in-plane, the original CASI® detector was used to validate the CCD measurement. In order to allow the CASI® to sample the diffraction pattern successfully, the smallest aperture and step sizes were manually forced for the entire scan. As shown in Figure 30, using $\theta_i = 40°$ as the example,

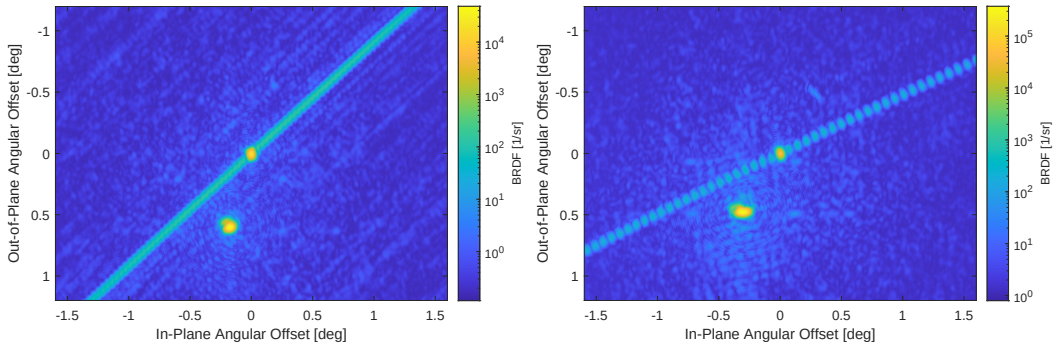

Figure 29. Plots of solar cell BRDF measurement data using a 15 mW red HeNe laser source with fixed illumination spot and metal bar orientation while varying θ_i from 20° to 60° in (a) and (b), respectively. The apparent diffraction pattern orientation and offset specular peak location shift with θ_i.

the agreement is quite good between the industry-standard CASI® and the CCD-augmented measurements. The individual diffraction peak spacing matches, and the peak magnitudes measured by the CASI® are within the uncertainty range of the CCD measurements. The CASI®'s maximum measurement uncertainty reaches approximately 17% near the specular direction [11], and so even most conservatively, if that uncertainty value is applied to the entire set of CASI® data points, the peak values still fall within the depicted CCD detector uncertainty bounds.

Since the traditional CASI® detector is constrained to single-pixel slices through the scatter hemisphere, for any other solar cell and diffraction pattern orientation, the CASI® is not able to easily measure the out-of-plane diffraction captured by the CCD detector.

5.5 From Measurement to Model

Data from any of the measured materials in this chapter can now be used for further analysis and modeling efforts. However, the solar cell measurements discovered particularly distinct and interesting reflectance features. In addition, previous studies

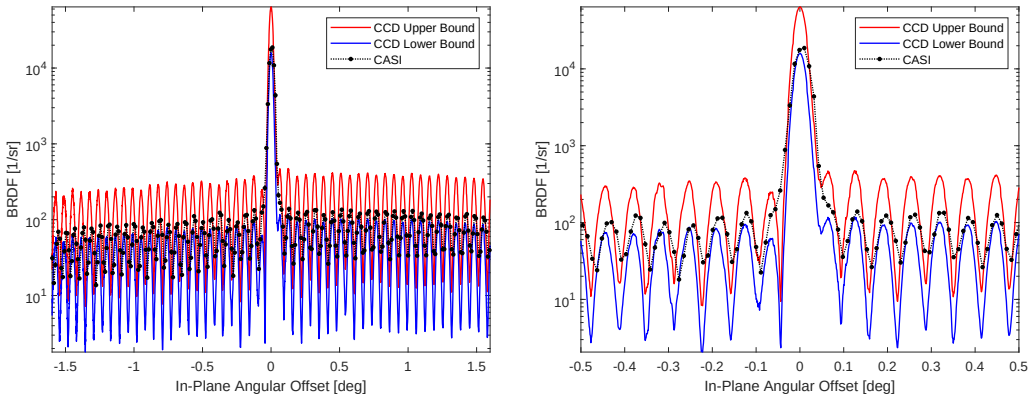

Figure 30. Comparison of CCD-augmented and original CASI® BRDF measurement data with the solar cell diffraction pattern oriented in-plane. The locations and magnitudes of each peak in the CASI® measurements agree well with the CCD-augmented measurements and fall within its uncertainty bounds.

from other authors (Section 2.4) identified solar panels as potential culprits for light curve glint modeling errors. Thus, in Chapter VI, the high-quality out-of-plane solar cell data will be used to inform the creation of a new BRDF model which successfully replicates both measured specular peaks and the diffraction pattern.

VI. Solar Cell BRDF Model

Using the solar cell BRDF measurements from Section 5.4 as the reference point, a closed-form BRDF model can be designed with separate terms for each of the three major observed features. In this work, overall feature shape and location were emphasized, leaving refined fitting choices for future efforts. The formulations for each term are discussed sequentially, and then numeric results are combined using manual parameter estimates.

6.1 Center Specular Peak

The first specular peak, whose center coincides with the center of the diffraction pattern, can be modeled relatively simply by using Equation (70) with the isotropic Beckmann distribution function from Equation (64) to govern peak shape [70, 3]. When substituted into Equation (70), the in-plane specular term can be written

$$f_{r_1} = \rho_{s_1} \frac{Q(n_1, \hat{\boldsymbol{\omega}}_{\boldsymbol{i}}, \hat{\boldsymbol{\omega}}_{\boldsymbol{s}})}{2(\cos\theta_i + \cos\theta_s)^2} \frac{1}{\pi m_1^2 \cos^4\theta_h} \exp\left[-\frac{\tan^2\theta_h}{m_1^2}\right], \tag{111}$$

which uses only one parameter m_1 to adjust Gaussian peak width. The half-angle θ_h can be calculated for any desired incident and scatter direction combination by implementing Equation (52). Specific selections for m_1, the weighting parameter ρ_{s_1}, and the complex index of refraction n_1 – which is embedded within Q – are discussed in Section 6.4.

6.2 Offset Specular Peak

The out-of-plane specular peak can be modeled using the same basic formulation as the in-plane peak with Equation (70). However, the material surface responsible

for this peak has a different overall normal direction, which correspondingly impacts the microfacet orientations atop that surface.

One intuitive way to account for this difference is to begin with incident and scatter directions relative to the first surface normal $\hat{\boldsymbol{n}}$, and then rotate each direction in order to express them relative to the second surface normal $\hat{\boldsymbol{n}}_{\boldsymbol{2}}$. This process is very similar to calculating $\hat{\boldsymbol{\omega}}_{\boldsymbol{d}}$ in Equation (52), and requires finding the rotation that brings $\hat{\boldsymbol{n}}_{\boldsymbol{2}}$ into alignment with $\hat{\boldsymbol{n}}$.

First, the angular offset between $\hat{\boldsymbol{n}}$ and $\hat{\boldsymbol{n}}_{\boldsymbol{2}}$ is described in terms of the parameters $\Delta\theta$ and $\Delta\phi_0$. As shown in Figure 31(a), $\Delta\theta$ is the difference in zenith angle, defined as a positive value when measured from $\hat{\boldsymbol{n}}$ to $\hat{\boldsymbol{n}}_{\boldsymbol{2}}$, and $\Delta\phi_0$ is the difference in azimuthal angle, defined as a positive value when measured from the $+\hat{x}$ (in-plane forward scatter) direction towards the $+\hat{y}$ (out-of-plane) direction. The arbitrary reference direction $\hat{\boldsymbol{\phi}}_{\text{ref}}$ is used to define the solar cell's orientation about $\hat{\boldsymbol{n}}$, referenced to the $-\hat{x}$ in-plane direction. In this work, $\phi_{\text{ref}} = 0$ when the metal bars are aligned in-plane with the diffraction pattern oriented out-of-plane. For other solar cell orientations, as in Figure 31(b), ϕ_{ref} is simply added to $\Delta\phi_0$ as an additional azimuthal offset.

The incident and scatter directions relative to $\hat{\boldsymbol{n}}_{\boldsymbol{2}}$ are then calculated by applying

$$\hat{\boldsymbol{\omega}}_{\boldsymbol{i_2}} = \mathbb{R}_y(-\Delta\theta)\mathbb{R}_z(-\Delta\phi_0 - \phi_{\text{ref}})\hat{\boldsymbol{\omega}}_{\boldsymbol{i}} \tag{112a}$$

$$\hat{\boldsymbol{\omega}}_{\boldsymbol{s_2}} = \mathbb{R}_y(-\Delta\theta)\mathbb{R}_z(-\Delta\phi_0 - \phi_{\text{ref}})\hat{\boldsymbol{\omega}}_{\boldsymbol{s}}, \tag{112b}$$

which in turn can be used in Equation (52) to calculate an updated microfacet angle $\hat{\boldsymbol{\omega}}_{\boldsymbol{h_2}}$. Finally, the offset specular peak term can be written

$$f_{r2} = \rho_{s2}\frac{Q(n_2, \hat{\boldsymbol{\omega}}_{\boldsymbol{i_2}}, \hat{\boldsymbol{\omega}}_{\boldsymbol{s_2}})}{2(\cos\theta_{i_2} + \cos\theta_{s_2})^2}\frac{1}{\pi m_2^2\cos^4\theta_{h_2}}\exp\left[-\frac{\tan^2\theta_{h_2}}{m_2^2}\right], \tag{113}$$

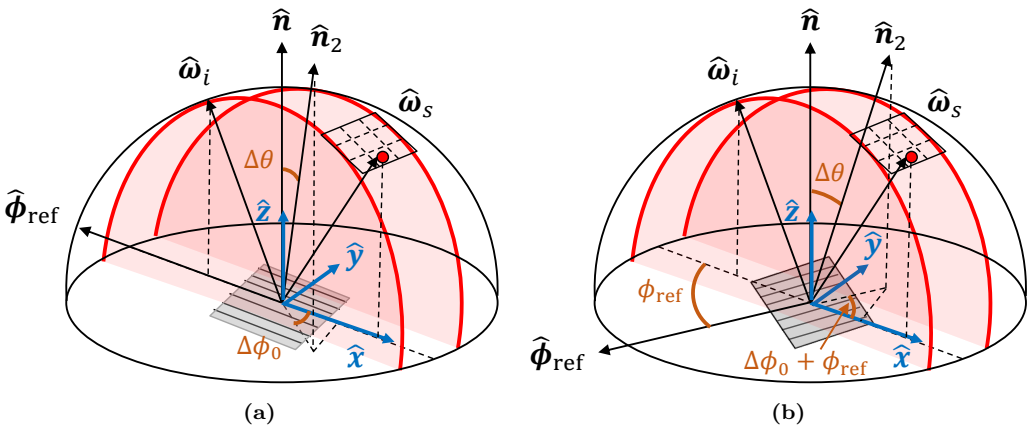

Figure 31. Illustration of the geometry used to model a specular peak from a second material with a different surface normal direction $\hat{n}_2$. The incident and scatter directions $\hat{\omega}_i$ and $\hat{\omega}_s$ are expressed relative to the first surface normal $\hat{n}$, but can be rotated using the parameters $\Delta\theta$, $\Delta\phi_0$, and ϕ_{ref}, which expresses them relative to the second surface normal $\hat{n}_2$ instead. In this graphic, the gray square represents the solar cell surface with metal bar orientation depicted to match $\hat{\phi}_{\text{ref}}$. The red dot within the dashed grid represents an example CCD pixel location, in this case in-plane.

which uses the parameter m_2 to adjust Gaussian peak width. As before, specific selections for m_2 as well as the weighting parameter ρ_{s_2} and the complex index of refraction n_2 – which is embedded within Q – are discussed in Section 6.4.

6.3 Diffraction Pattern

Modeling the diffraction pattern requires a significantly different formulation than the geometric optics-based microfacet terms employed for the in-plane and offset specular peaks. Fortunately, closed-form solutions exist for diffraction through multiple rectangular apertures using Fourier theory with the Fraunhofer approximation [30]. The Fraunhofer conditions apply to the measurements in Chapter V, based on the highly-focused beamwidth (less than 0.15 mm), wavelength of the visible laser source (632.8 nm), and the established distance between sample stage and CCD detector (approximately 0.325 cm).

Fraunhofer diffraction solutions tend to be written in terms of collection plane

coordinates, expressed either as linear offsets or angular offsets from an optical axis about which the pattern is centered [30, 38]. For reflection from the solar cell, the diffraction pattern is centered on the specular direction with the $(\bar{x}, \bar{y}, \bar{z})$ coordinate system as shown in Figure 32. Here, the $\bar{z}$ axis points along the specular direction, and the $\bar{x}$ and $\bar{y}$ axes rotate along with $\hat{\boldsymbol{\phi}}_{\text{ref}}$ to remain aligned with the metal bar orientation. The $\bar{x}$ and $\bar{y}$ directions are chosen so that the projection of $\bar{x}$ aligns longitudinally with the metal bars and the projection of $\bar{y}$ runs transverse to the metal bars.

The best agreement with the measurement results was found by basing the model on the Fraunhofer solution for diffraction through two rectangular stripes with separation a and individual widths b. The pair of stripes can be mathematically represented by a rectangle function convolved with two delta functions. Since the Fourier transform of a rectangle is a sinc, and the Fourier transform of two delta functions is a cosine, the resulting transverse Fraunhofer irradiance pattern can be represented by $\text{sinc}^2(b\bar{y}/\lambda\bar{z})\cos^2(\pi a\bar{y}/\lambda\bar{z})$.

Since the length of each bar extends beyond the effective laser illumination spot, the diffraction pattern is really only a function of the transverse direction $\bar{y}$. However, in practice, the diffraction band does show some tangible width in the $\bar{x}$ direction. The incident laser beam is Gaussian, so simply multiplying by $\exp(-\bar{x}^2/c^2)$ effectively curtails the width of the diffraction band, using c as the Gaussian width parameter.

The Fraunhofer solution so far, however, assumes normal incidence, and when $\bar{y}$ is written in terms of microfacet coordinate angles (shown later in this section), the spacing between simulated diffraction peaks scales with incident angle, contrary to the observations which show consistent spacing for different incident angles. The grating equation, written $\sin\theta_m = m\lambda/a + \sin\theta_i$ [38], demonstrates the potential impact of incident angle on diffraction order spacing. By looking at its derivative,

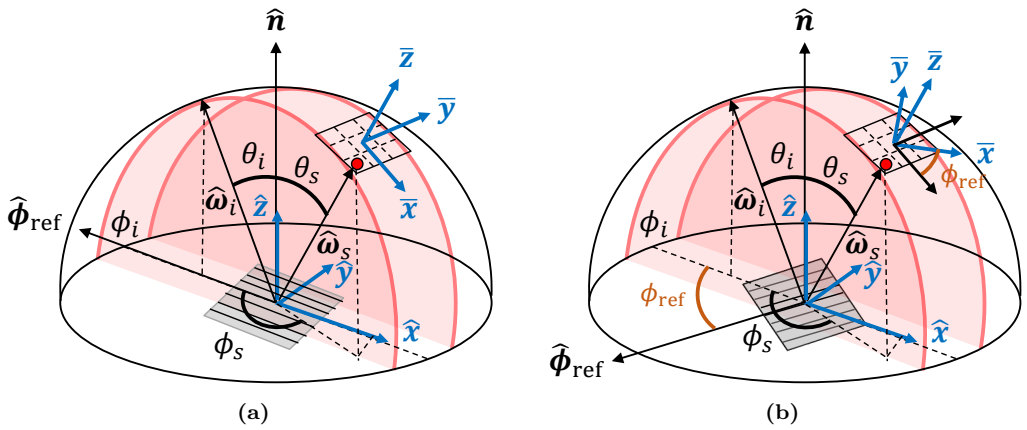

Figure 32. Illustration of the geometry and coordinates used to model the diffraction pattern under Fraunhofer approximations. The gray square represents the solar cell surface with metal bar orientation depicted to match $\hat{\phi}_{\text{ref}}$. The $\bar{z}$ axis points along the specular direction. When the solar cell is rotated about its normal, denoted by a change in $\hat{\phi}_{\text{ref}}$ from (a) to (b), the $\bar{x}$ and $\bar{y}$ axes also rotate by ϕ_{ref} so that their projections remain aligned with the metal bar orientation. The red dot within the dashed grid represents an example CCD pixel location, in this case with an out-of-plane component.

it is possible to see that multiplying the arguments of the sinc^2 and $\cos^2$ functions by $\sqrt{1-\sin^2\theta_i} = \cos(\theta_i)$ should instead preserve consistent spacing as θ_i varies. In practice, an extra factor of two was required, demonstrated by simulations in Section 6.4,

Combining the pieces above, the diffraction model can be written in terms of $\bar{x}$, $\bar{y}$, and $\bar{z}$ as

$$f_{r_3} = \rho_{s_3}\cos^2\left(\frac{2\pi a\bar{y}}{\lambda\bar{z}}\cos(\theta_i)\right)\text{sinc}^2\left(\frac{2b\bar{y}}{\lambda\bar{z}}\cos(\theta_i)\right)\exp\left[-\frac{\bar{x}^2}{c^2}\right]. \tag{114}$$

The leading constant ρ_{s_3} is used to adjust the magnitude of the pattern, which would otherwise be normalized to a peak value of one.

BRDFs are ubiquitously written as functions of incident and scatter angles rather than linear coordinates, and so several different formulations were attempted for expressing $\bar{x}$, $\bar{y}$, and $\bar{z}$ in terms of angles. Rather than writing them directly in terms

of $\hat{\boldsymbol{\omega}}_{\boldsymbol{s}}$ and $\hat{\boldsymbol{\omega}}_{\boldsymbol{i}}$, the most effective method discovered involves writing them in terms of the half-angle direction $\hat{\boldsymbol{\omega}}_{\boldsymbol{h}}$. Favorably, $\theta_h = 0$ naturally occurs at the specular peak for any θ_i, so that $\bar{x}$ and $\bar{y}$ equal zero there. Good agreement with measurement was achieved by writing

$$\bar{x} = R\sin\theta_h\cos(\phi_h - \phi_{\text{ref}} + \pi) \tag{115a}$$

$$\bar{y} = R\sin\theta_h\sin(\phi_h - \phi_{\text{ref}} + \pi) \tag{115b}$$

$$\bar{z} = R. \tag{115c}$$

The extra π accounts for the convention of measuring ϕ_s and ϕ_h from the -$\hat{x}$ direction. Conveniently, the R cancels out inside both the $\cos^2$ and sinc^2 terms in Equation (114). Also, in this format, although the $\bar{x}$ and $\bar{y}$ coordinates tend to compress as θ_i increases (due to changes in θ_h), the added $2\cos\theta_i$ within Equation (114) offsets this impact.

As will be shown in the next section, this choice for the diffraction model and the $(\bar{x}, \bar{y}, \bar{z})$ coordinate conversion sufficiently models the diffraction pattern curvature and orientation changes observed for various θ_i, matching the measurements in Figures 27 and 29.

6.4 Numeric Simulations

This section combines the three BRDF model terms from Sections 6.1–6.3 and compares them to the measurements from Section 5.4. Numeric model parameters are manually selected based largely on physical material characteristics, rather than using any fitting or optimization algorithms. In order to make valid comparisons, the models are used to simulate BRDF results for the same incident and scatter angles which comprise each pixel within the specular CCD measurements. The calculations

for those angles are described Section 3.5.

Parameter Selection.

The in-plane specular peak model contains three parameters: m_1, n_1 and ρ_{s_1}. After some manual parameter adjustment to qualitatively approximate the specular peak width and magnitude, m_1 and ρ_{s_1} are set for this analysis to 2×10^{-4} and 0.015, respectively. For this particular solar cell, the published top photovoltaic layer is InGaP, which is typically responsible for ultraviolet and visible absorption below about 650 nm [52]. The real component of its index of refraction can be approximated as 3.6 at 632.8 nm [61], and so n_1 is set to this value.

The out-of-plane specular peak model contains five parameters: m_2, n_2, ρ_{s_2}, $\Delta\theta$, and $\Delta\phi_0$. By assuming the width of this peak matches the in-plane peak, m_2 is set to 2×10^{-4}. After some manual parameter adjustment to qualitatively approximate peak magnitude, ρ_{s_2} is set to 0.7. The space-grade encapsulant used for the coverglass adhesion has a real-valued index of refraction of 1.4, so n_2 is set to this value. For proof of concept, $\Delta\theta$ and $\Delta\phi_0$ are simply set to 0.5° and 45°, respectively, which should place the location of the offset peak within the CCD detector field of view, but down (in the $+\hat{y}$ out-of-plane direction) and to the right (in the $+\hat{x}$ in-plane direction) of the in-plane peak when $\phi_{\text{ref}} = 0$.

The diffraction pattern model contains four parameters: a, b, c, and ρ_{s_3}. Physically, a represents the spacing between the solar cell's metal bars, which also dictates the separation between high-frequency diffraction peaks according to the quantity $\lambda/a\bar{z}$. Based on the measured vertical pattern spacing from Figure 27(a) and the CCD's nominal distance from the sample, the derived bar spacing is approximately 7.5×10^{-4} m, which corresponds closely to the product specification. Thus, for this section, a is set to the product specification of 8×10^{-4} m. The parameter b physi-

cally represents the width of each metal bar, which is set to 1×10^{-5} m, also based on product specification. Finally, ρ_{s_3} is set to 300 so that the normalized $\cos^2$ and sinc^2 functions approximately match the diffraction peak magnitudes, and c is set to 4×10^{-5} to qualitatively set the diffraction pattern width.

Simulation Results and Comparison to Measurements.

Using the numeric parameter values discussed in Section 6.4, Figure 33 shows the BRDF simulation results for incident angles of 20° and 60° with the solar cell's metal bars oriented in-plane ($\phi_{\text{ref}} = 0$) and using scatter angles to match CCD pixel locations during the specular measurements in Figure 27. Following Figure 27's format, Figure 33(a) and 33(c) display the entire simulated pixel array, while Figures 33(b) and 33(d) extract BRDF values from the pixel columns running vertically (out-of-plane) through the center of each specular peak.

Qualitatively, this model succeeds in reproducing the diffraction pattern and both specular peaks discovered during measurement, and quantitatively, the simulated maximum values of each feature are well within an order of magnitude of the measured values. The simulated center peak is located in the primary specular direction, as desired, with maximum magnitudes of 1.11×10^4 sr^{-1} and 3.91×10^4 sr^{-1} for $\theta_i = 20°$ and 60°, respectively, which compare well to the measured peak values of 9.90×10^3 sr^{-1} and 4.83×10^4 sr^{-1} at those incident angles.

The simulated offset peak has shifted down and to the right, as expected, and includes a slight compression of the down (or out-of-plane) component at the higher incident angles. This peak's simulated maximum values are approximately 4.44×10^4 sr^{-1} and 4.19×10^5 sr^{-1} for $\theta_i = 20°$ and 60°, respectively, which compare well to the measured peak values of 6.03×10^4 sr^{-1} and 4.21×10^5 sr^{-1} at those incident angles.

The simulated diffraction pattern is oriented out-of-plane when $\phi_{\text{ref}} = 0$, as desired,

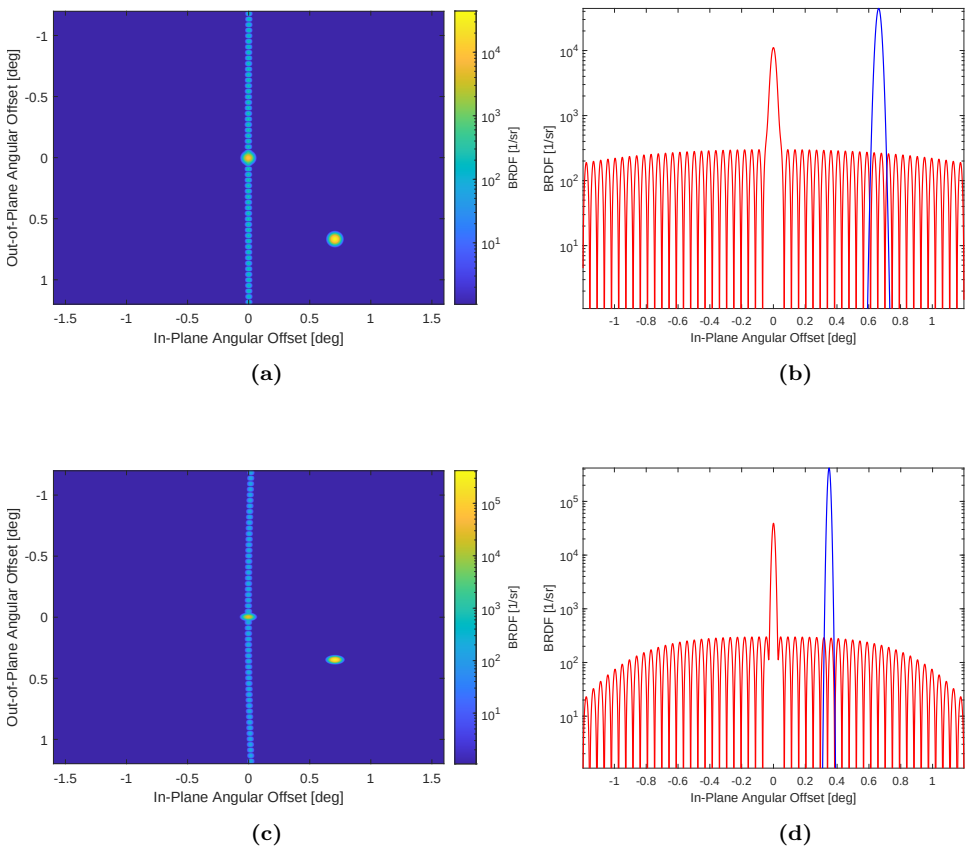

Figure 33. Plots of the combined solar cell BRDF simulation results with in-plane metal bar orientation. The scatter coordinates are the same as the CCD pixel coordinates measured in Fig. 27, with $\theta_i = 20°$ in (a) and (b), and $\theta_i = 60°$ in (c) and (d). The full pixel arrays are simulated in (a) and (c), with vertical pixel columns through the center of each peak plotted in (b) and (d). The simulations successfully replicate each of the three primary measured features (center specular peak, offset specular peak, and diffraction pattern), and the peak values for each simulated feature compare to the measured data well within an order of magnitude.

and at higher incident angles, the curvature noticeable in the measurements is also noticeable in the simulation. The simulated diffraction peak magnitudes range from 300 sr^{-1} nearest the center specular peak to 209 sr^{-1} at each edge of the array. For comparison, when $\theta_i = 20°$, the peak measured diffraction value near the center is 312 sr^{-1} while the peak values nearest each edge average to 145 sr^{-1}. When $\theta_i = 60°$, the peak measured diffraction value near the center is 312 sr^{-1} while the peak values nearest each edge average to 202 sr^{-1}. Particularly at $\theta_i = 60°$, the vertical pixel slice in Figure 33(d) no longer follows the diffraction peaks as closely, due to the diffraction pattern curvature, so the peak values appear artificially reduced near the edges.

Keeping in mind that the metal bar separation is only known to one significant figure based on product specifications (800 μm), the simulated diffraction peak spacing also agrees well with the measured diffraction peak spacing (within 8%). For both incident angles, there are 26 simulated peaks between the CCD center and edges, and 24.5 measured peaks between the center and edges. It is worth noting that if the $2\cos\theta_i$ term within Equation (114) is omitted (whose inclusion was motivated by the grating equation described in Section 6.3), then the simulated diffraction pattern spacing changes so that 14 simulated peaks exist between the CCD center and edge when $\theta_i = 20°$ and 26 simulated peaks exist when $\theta_i = 60°$.

Changing the value of ϕ_{ref} simulates changing the metal bar orientation relative to the plane of incidence. Figures 34(a) and 34(b) show that by setting $\phi_{\text{ref}} = 45°$ and 90°, respectively, the simulated diffraction pattern and offset peak both rotate about the central peak, mimicking the measured behavior in Figure 28. In addition, Figures 35(a) and 35(b) show that for a fixed metal bar orientation – for example $\phi_{\text{ref}} = 45°$ – the apparent orientation of the diffraction pattern changes as θ_i increases, mimicking the measured behavior in Figure 29. Here, it is important to note that without writing $\bar{x}$, $\bar{y}$, and $\bar{z}$ in terms of $\hat{\boldsymbol{\omega}}_{\boldsymbol{h}}$ in Equation (115), the simulation fails to

account for these particular phenomena. For instance, another formulation for $\bar{x}$ and $\bar{y}$ – writing them in terms of $\hat{\boldsymbol{\omega}}_{\boldsymbol{s}}$, and then rotating to align the specular $\bar{z}$ direction and the in-plane -$\bar{x}$ direction with the surface normal $\hat{z}$ direction and the metal bar orientation $\hat{\boldsymbol{\phi}}_{\text{ref}}$, respectively – also maintained consistent diffraction peak spacing, but failed to account for the curvature and apparent orientation changes at higher incidence angles.

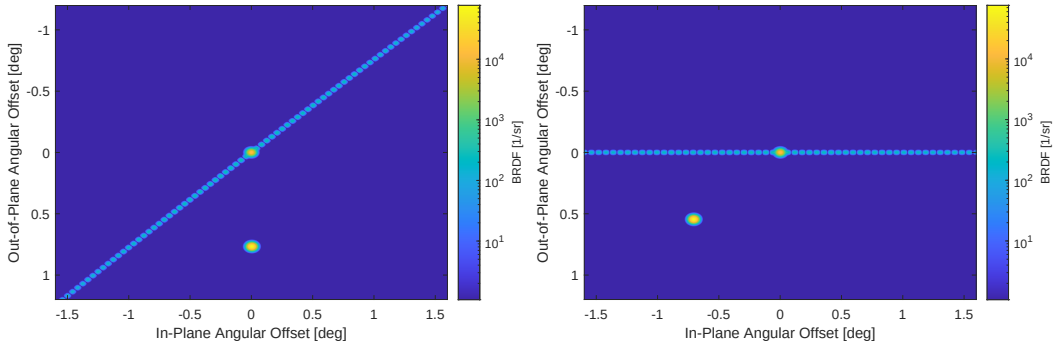

Figure 34. Plots of the combined solar cell BRDF simulation results with metal bars oriented $45°$ out-of-plane in (a) and fully out-of-plane in (b). The scatter coordinates are the same as the CCD pixel coordinates measured in Figure 28 with $\theta_i = 40°$. Similar to the measured results, the offset specular peak and diffraction pattern rotate about the center specular peak as $\phi_{\mathbf{ref}}$ changes.

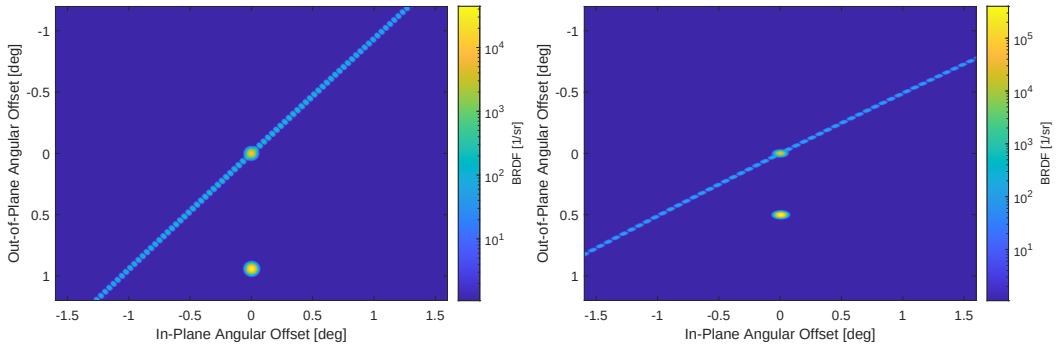

Figure 35. Plots of the combined solar cell BRDF simulation results while varying θ_i from $20°$ to $60°$ in (a) and (b), respectively. The scatter coordinates are the same as the CCD pixel coordinates measured in Figure 29 and $\phi_{\mathbf{ref}} = 45°$. Similar to the measured results, the out-of-plane components compress as θ_i increases, which alters the apparent orientation of the diffraction pattern.

In summary, this chapter proposes a closed-form BRDF model which successfully captures all three major features of the solar cell measurements from Section 5.4, including the center specular peak, the offset specular peak, and the diffraction pattern. In particular, the offset specular peak and diffraction pattern terms contain new BRDF formulations which capture the observed out-of-plane and wavelength-dependent behavior at various incident angles and orientations.

VII. Conclusion

The research hypothesis stated that the disparity between observed and simulated light curve glints may be improved by identifying satellite materials with substantial out-of-plane reflectance contributions, and then subsequently updating those material BRDF models to better match specular out-of-plane measurements. The key findings which arose from answering the research questions provide evidence to support the plausibility of this hypothesis (though still unproven).

7.1 Key Findings

Research Question 1.

By augmenting the CASI® with a scientific-grade CCD camera along with sufficient motion stages for alignment, a new system was successfully created for simultaneously measuring several degrees of both in-plane and out-of-plane specular BRDF data. In fact, due to pixel size, the system achieved an angular resolution better than 0.001°, which is approximately an order of magnitude better than the original CASI®. Although the new system sacrifices up to two-thirds of the original dynamic range, it still captures more than five orders of magnitude simply by stitching together exposure times ranging from 1 ms to 1 s. A robust uncertainty analysis identified that uncertainty in the OD of ND filters provided the largest overall contribution, depending on the difference between filters used for a beam signature and subsequent measurement. However, when OD uncertainty is negligible, the typical total relative uncertainties for nearly any scatter angle are in the vicinity of 4%, compared to minimum values near 2% [13] or 7.5% [11] for the original system. For both a beam signature and solar cell measurement, the augmented system was successfully validated with the original CASI® showing remarkable agreement.

Research Question 2.

The new measurement system successfully identified significant out-of-plane BRDF characteristics. First, a broadband mirror provided an isotropic baseline, which matched the beam signature well. Then, two materials with known anisotropic surface characteristics were chosen: 1) polished aluminum with circular grooves and 2) a solar cell with periodically-spaced metal conducting bars. Both demonstrated visibly identifiable out-of-plane behavior. A third material – the unwrinkled Kapton® – had unknown surface characteristics, but also demonstrated out-of-plane specular reflection.

Of all the material samples, the solar cell produced the most significant out-of-plane results consisting of a diffraction pattern and both central and offset specular peaks. By varying the orientations of the solar cell on the sample stage, several out-of-plane functionalities were discovered. For instance, as incident angle increased, the out-of-plane components seemed to compress, altering the apparent curvature and orientation of the diffraction pattern as well as the apparent location of the offset specular peak. Additionally, when the solar cell was rotated about its normal direction, both the offset specular peak and diffraction pattern rotated in kind about the central specular peak. This behavior indicated that the offset specular peak was caused by reflection from a surface with a slightly different normal direction, and also confirmed that the diffraction patterns were caused by the metal bars. Finally, the measurements showed that diffraction peak spacing was unaffected by incident angle.

Research Question 3.

Despite the solar cell's relatively complicated BRDF features, its out-of-plane components were successfully modeled by combining three major terms. The central specular peak was first modeled using a common specular microfacet formulation.

The offset specular peak was addressed using a term with the same format, except for rotating the incident and scatter directions to account for a different surface normal. Finally, the diffraction pattern model was inspired by a closed-form solution from Fourier optics for diffraction through two stripes. The diffraction solution required two key reformulations. First, the inputs were written in terms of microfacet coordinate angles. Second, the inputs required scaling by the cosine of the incident angle, whose form was inspired by the grating equation's dependence on incident angle. Finally, when based on the physical metal bar spacing and widths, diffraction simulations matched each of the measured behaviors.

7.2 Key Contributions

This work produced two main contributions. First, the CCD-augmented CASI® represents a novel BRDF measurement system producing the first published out-of-plane BRDF data surrounding the specular peak with such high resolution. Not only does it represent a new measurement system, but its validated results agree very well with the industry-standard CASI®. This main contribution contains many sub-contributions, including a formulation for mapping an array of pixels to scatter coordinates, and a robust uncertainty analysis for this type of system. The design, setup, alignment, and calibration processes are documented in a conference paper [66]; pixel scatter angle mapping and initial measurement results for the mirror, polished aluminum, and Kapton® samples are presented in another conference paper [67]; and the uncertainty analysis has been submitted to a peer-reviewed journal [65].

Second, the updated solar cell BRDF model represents the first known version which successfully includes an offset specular peak and a diffraction pattern, both written in closed form in terms of the traditional BRDF inputs $\hat{\boldsymbol{\omega}}_i$, $\hat{\boldsymbol{\omega}}_s$, and λ. A paper describing the updated solar cell measurements and the resulting model have

been submitted to a peer-reviewed journal [64].

7.3 Future Work

This project contains many avenues for continued work. Perhaps the most obvious next step is to incorporate the updated solar cell BRDF model into light curve analysis simulations to test the impact. Particularly due to the wide angular extent of the diffraction pattern across the scatter hemisphere, along with its relatively high magnitudes away from the specular direction, there may be more incident and scatter angle combinations than before which cause an apparent glint. The width of the diffraction pattern is similar to the width of the center specular peak, and the diffraction peak magnitudes are only four orders of magnitude lower than the center peak, even several degrees away from the specular direction. Thus, roughly, as long as the general diffuse reflection is more than four orders of magnitude below the primary glint level, which seems very likely based on the noise floor shown in Figure 27, then glints from transits across the diffraction pattern should also be visible. Of course ultimately, any simulated impacts should be compared against actual observational data as well.

In addition, since photometric observations are often collected across spectral bands rather than specific wavelengths, the solar cell should be measured with laser sources at other wavelengths, including infrared and ultraviolet, in order to either validate or update the model. The current camera is only responsive within the visible wavelength range ($400 - 700$ nm), so new cameras would be needed to explore wavelengths beyond this range. The diffraction model in particular possesses explicit wavelength-dependence. Including it within the rendering equation would require integrating over the applicable wavelength band, and such integration should be expected to blur the distinct diffraction orders in Figures 27–29 into a stripe.

Other solar cells may possess different surface characteristics which lead to differences in out-of-plane behavior. Rather than treat this individual solar cell as representative, other solar cells can be procured, measured, and modeled. Also, there may be other important satellite materials which exhibit significant out-of-plane behavior worth identifying, measuring, and modeling.

The updated solar cell model agreed very well with the measurements, even when basing parameter selection purely on physical material properties. The model could likely be improved by running an optimization algorithm against the data to find the best fits for each parameter.

This work focused entirely on measurements in which the CCD was centered on the specular direction. However, the CASI® detector arm can be slewed away from center. For one, slewing the detector arm allows access to other scatter angles. In addition, when the brightest signals no longer land on the FPA, the measurement OD can be reduced, which can lead to increased dynamic range. Larger scatter angles and greater dynamic ranges allow for measuring more diffuse reflectance signals, as well as exploring the solar cell diffraction pattern beyond the nominal 3.19° by 2.40° specular field of view, and so this capability should be explored.

The largest source of uncertainty for the augmented system with the uncertainty in the disparity between the OD required for the beam signature and the OD required for a measurement. However, the uncertainty levels in this work assumed only the worst-case generic tolerances from ND filter production. In order to reduce measurement uncertainty, the simplest method would be to independently characterize each of the ND filters. Pixel non-linearity represented a significant secondary uncertainty contribution, and so implementing a non-linearity correction algorithm could also be beneficial.

The beam signature and the mirror measurements are strikingly but expectedly

similar. In fact, most of the mirror's measured behavior is really an artifact of the beam's Gaussian nature, rather than the mirror's actual BRDF. In reality, the mirror's BRDF is likely closer to a delta function. The imprint of the source beam on a BRDF measurement always occurs, although more noticeable and impactful for highly specular materials. Since the CCD provides such a high angular resolution, if enough spatial frequency content is present, the measurements could possibly be de-convolved from the Gaussian beam to provide a more accurate BRDF output.

Finally, interrogating the solar cell's BRDF required rotating the sample about its own normal direction. However, the CASI® material sample stage does not possess in automated or controlled way to perform these rotations, and so they were accomplished manually for this work. However, incorporating a motorized rotation stage would allow for more precise control over the sample's orientation, which could improve the quality of measured out-of-plane data.

To conclude, the results from this work pave the way for significant improvements in predicting and interpreting satellite light curve observations, ultimately enhancing overall space domain awareness for the U.S. and the rest of the world. In particular, solar cells commonly represent the predominant surface area on many satellites, which makes the importance of correctly modeling solar cell reflection vitally important for understanding reflection signatures from satellites in general.

Appendix A. Additional Measurement Results

1.1 Broadband Mirror

The broadband mirror BRDF results for $\theta_i = 40°$ and $\theta_i = 60°$ are displayed in Figures 36 and 37, respectively. The peak BRDF values increase as θ_i increases. Qualitatively, any changes in the specular peak shape are very slight.

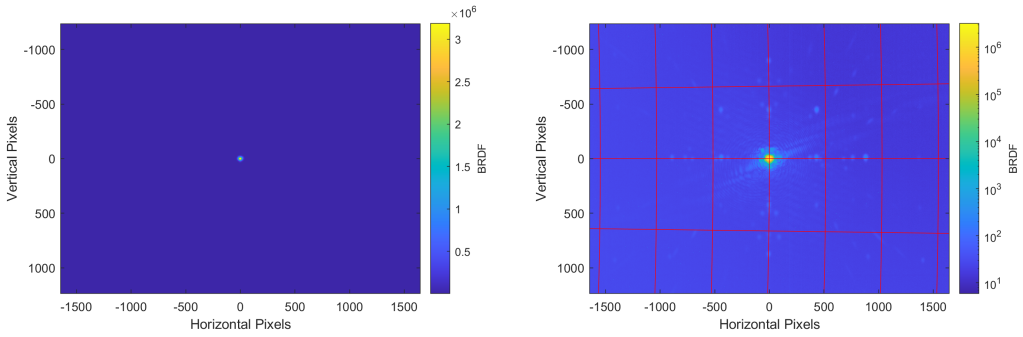

(a) **(b)**

Figure 36. Plots of the broadband mirror BRDF measurement data for $\theta_i = 40°$ using a linear scale (a) and log scale (b), including an overlay with contours of constant θ_s and ϕ_s in $0.5°$ and $1°$ increments, respectively, in (b).

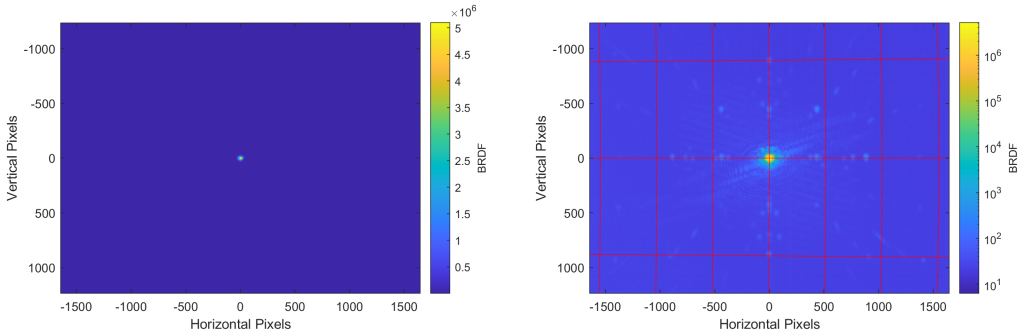

(a) **(b)**

Figure 37. Plots of the broadband mirror BRDF measurement data for $\theta_i = 60°$ using a linear scale (a) and log scale (b), including an overlay with contours of constant θ_s and ϕ_s in $0.5°$ and $1°$ increments, respectively, in (b).

1.2 Polished Aluminum

The polished aluminum BRDF results for $\theta_i = 20°$ and $\theta_i = 60°$ are displayed in Figures 38 and 39, respectively. The peak BRDF values increase as θ_i increases. Qualitatively, the orientation of the specular peak compresses as θ_i increases.

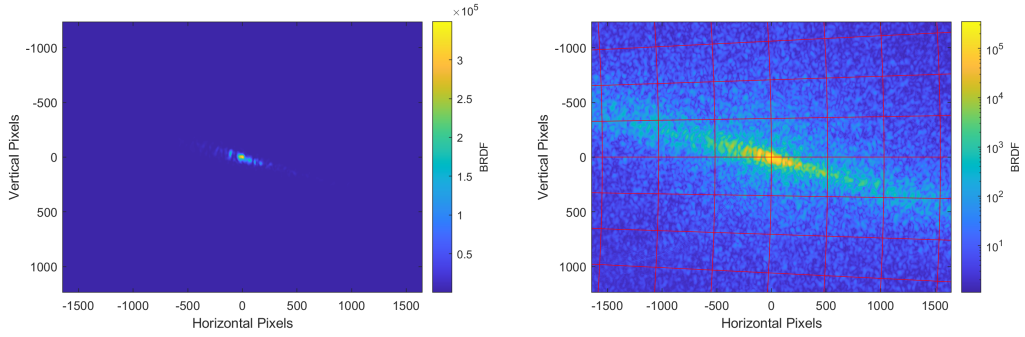

(a) **(b)**

Figure 38. Plots of the polished aluminum BRDF measurement data for $\theta_i = 20°$ using a linear scale (a) and log scale (), including an overlay with contours of constant θ_s and ϕ_s in $0.5°$ and $1°$ increments, respectively, in (b).

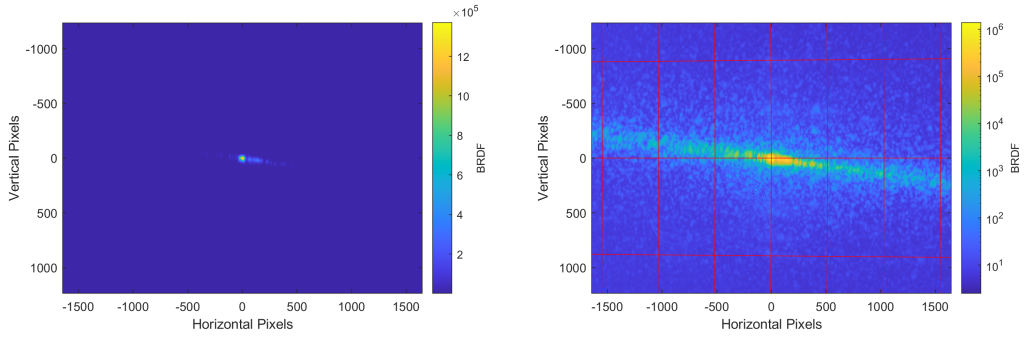

(a) **(b)**

Figure 39. Plots of the polished aluminum BRDF measurement data for $\theta_i = 60°$ using a linear scale (a) and log scale (), including an overlay with contours of constant θ_s and ϕ_s in $0.5°$ and $1°$ increments, respectively, in (b).

1.3 Kapton®

The Kapton® BRDF results for $\theta_i = 20°$ and $\theta_i = 40°$ are displayed in Figures 40 and 41, respectively. The peak BRDF values increase as θ_i increases. Qualitatively, the orientation of the specular peak compresses and the shape becomes more elongated as θ_i increases..

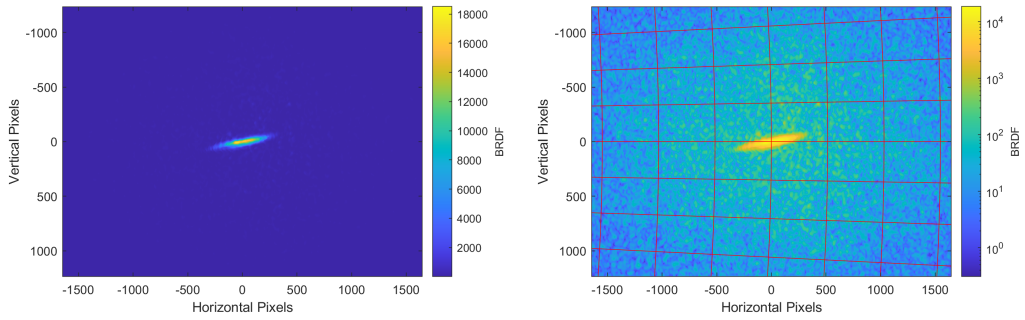

(a) **(b)**

Figure 40. Plots of the Kapton® BRDF measurement data for $\theta_i = 20°$ using a linear scale (a) and log scale (b), including an overlay with contours of constant θ_s and ϕ_s in $0.5°$ and $1°$ increments, respectively, in (b).

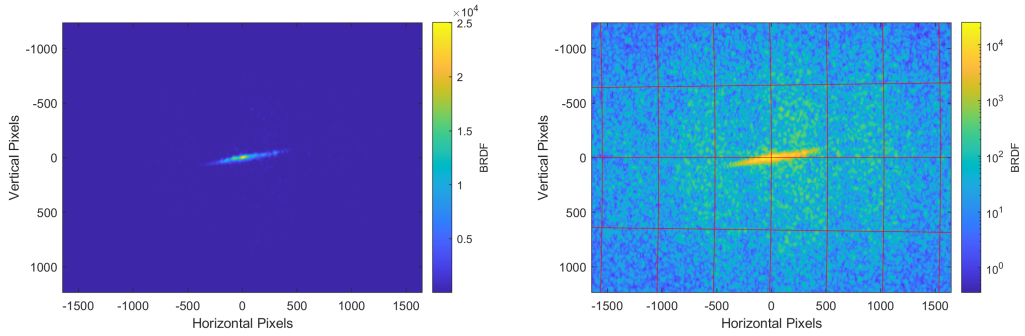

(a) **(b)**

Figure 41. Plots of the Kapton® BRDF measurement data for $\theta_i = 40°$ using a linear scale (a) and log scale (b), including an overlay with contours of constant θ_s and ϕ_s in $0.5°$ and $1°$ increments, respectively, in (b).

Bibliography

1. "Computer Graphic Rendering of Material Surfaces: NEFDS". Website accessed in Jul 2021. Available at https://math.nist.gov/ FHunt/appearance/nefds.html.

2. Air Force Basic Doctrine, Organization, and Command. *Air Force Doctrine Document 1*, 14 October 2014.

3. P. Beckmann and A. Spizzichino. *The Scattering of Electromagnetic Waves from Rough Surfaces*. MacMillan, 1963.

4. D. Bennett, J. Dank, D. Tyler, M. Gartley, and D. Allen. "SSA Modeling and Simluation with DIRSIG". *Advanced Maui Optical and Space Surveillance Technologies Conference*, September 2014.

5. D. Bowers, D. Wellems, M. Duggin, W. Glass, and L. Vaughan. "Broadband Spectral-Polarimetric BRDF Scan System and Data for Spacecraft Materials". In *Advanced Maui Optical and Space Surveillance Technologies Conference*, 2011.

6. R. Boyd. *Radiometry and the Detection of Optical Radiation*. John Wiley & Sons, New York, NY, 1983.

7. W. Brissett. "A Closer Watch on Space". *Air Force Magazine*, August 2017.

8. B. Burley. "Physically-Based Shading at Disney". *ACM SIGGRAPH 2012 Courses*, 2012.

9. S. Butler and M. Marciniak. "Robust Categorization of Microfacet BRDF Models to Enable Flexible Application-Specific BRDF Adaptation". *Proc. SPIE, Publication 920506-1*, September 2014.

10. S. Butler, S. Nauyoks, and M. Marciniak. "Comparison of Microfacet BRDF Model to Modified Beckmann-Kirchhoff BRDF Model for Rough and Smooth Surfaces". *Opt. Express*, 23(22):29100 – 29112, Nov 2015.

11. S Butler, S Nauyoks, and M Marciniak. "Experimental measurement and analysis of wavelength-dependent properties of the BRDF". In *Imaging Spectrometry XX*, volume 9611, pages 78 – 92, 2015.

12. S. Butler, S. Nauyoks, and M. Marciniak. "Comparison of Microfacet BRDF Model Elements to Diffraction BRDF Model Element". *Proc. SPIE, Publication 94720C-1*, August 2015.

13. F. Cady, D. Bjork, J. Rifkin, and J. Stover. "BRDF Error Analysis". *SPIE: Scatter from Optical Components*, Vol 1165:154–164, 1990.

14. F. Cady, D. Bjork, J. Rifkin, and J. Stover. "Linearity In BSDF Measurements". In *Scatter from Optical Components*, volume 1165, pages 192 – 203, 1990.

15. M. Werth, D. Gerwe, S. Griffin, B. Calef and P. Idell. "Imaging GEOs with a Ground-Based Sparse Aperture Telescope Array". *Advanced Maui Optical and Space Surveillance Technologies Conference Proceedings*, 2018.

16. A. Ceniceros, D. Gaylor, J. Anderson, E. Pinon III, P. Dao, and R. Rast. "Comparison of BRDF-Predicted and Observed Light Curves of GEO Satellites". *Advanced Maui Optical and Space Surveillance Technologies Conference*, September 2015.

17. R. Cognion. "Observations and Modeling of GEO Satellites at Large Phase Angles". In *Advanced Maui Optical and Space Surveillance Technologies Conference*, 2013.

18. J. Conant and F. Iannarilli Jr. "Development of a Combined Bidirectional Reflectance and Directional Emittance Model for Polarization Modeling". *Society of Photographic Instrumentation Engineers*, Vol 4481:206–215, 2002.

19. G. Crockett. Laser Range Safety Tool (LRST Physics Reference. AFRL-HE-BR-TR-2003-0119, September 2003.

20. M. Duggin, J. Riker, W. Glass, K. Bush, D. Briscoe, M. Klein, M. Pugh, and B. Engberg. "Multi-Spectral Analysis for Improved Space Object Characterization". *Advanced Maui Optical and Space Surveillance Technologies Conference*, September 2008.

21. DuPont™. "Kapton®: Polyimide Film". Website accessed in Jul 2021. Available at https://www.dupont.com/electronic-materials/polyimide-films.html.

22. A. Ngan, F. Durand and W. Matusik. "Experimental Analysis of BRDF Models". *Eurographics Symposium on Rendering*, 2005.

23. M. Eismann. *Hyperspectral Remote Sensing*. SPIE press, 2012.

24. European Machine Vision Association. EMVA Standard 1288: Standard for Characterization of Image Sensors and Cameras. Website accessed in Jul 2021. (Release 3.1: 30 Dec 2016), Available at https://www.emva.org/wp-content/uploads/EMVA1288-3.1a.pdf.

25. B. Ewing, S. Butler, and M. Marciniak. "Improved Grazing Angle Bidirectional Reflectance Distribution Function Model using Rayleigh–Rice Polarization Factor and Adaptive Microfacet Distribution Function". *Optical Engineering*, 57(10):1 – 9, 2018.

26. J. Filip, R. Vavra, and M. Havlicek. "Effective Acquisition of Dense Anisotropic BRDF". *IEEE 22nd International Conference on Pattern Recognition*, 2014.

27. A. Friedman. "Determination of Specular Reflection from Cylindrical Satellites for Electro-Optical Surveillance and SOI". *Massachusetts Institute of Technology Lincoln Laboratory Technical Report*, October 1976.

28. M. Gartley. *Polarimetric Modeling of Remotely Sensed Scenes in the Thermal Infrared*. PhD thesis, Rochester Institute of Technology, 2007.

29. H. Goldstein, C. Poole, and J. Safko. *Classical Mechanics, 3rd Edition*. Pearson Education, Inc., 2002.

30. J. Goodman. *Introduction to Fourier Optics, 4th Ed.* W.H. Freeman, 2017.

31. D. Griffiths. *Introduction to Electrodynamics*. Cambridge University Press, New York, NY, 2017.

32. V. Gudimetla, E. Reinhart, and C. Hart. "TASAT Simulations of NASA Image Satellite to Predict the Spin Rate". *Advanced Maui Optical and Space Surveillance Technologies Conference*, September 2007.

33. S. Hagerty and H. Ellis. "A High Fidelity Approach to Data Simulation for Spafce Situational Awareness Missions". *Advanced Maui Optical and Space Surveillance Technologies Conference*, September 2016.

34. A. Harms, K. Hamada, C. Wetterer, K. Luu, C. Sabol, and K. Alfriend. "Understanding Satellite Characterization Knowledge Gained from Radiometric Data". *Advanced Maui Optical and Space Surveillance Technologies Conference*, September 2012.

35. J. Harvey, A. Krywonos, and J. Stover. "Unified Scatter Model for Rough Surfaces at Large Incident and Scatter Angles". In *Advanced Characterization Techniques for Optics, Semiconductors, and Nanotechnologies III*, volume 6672, pages 103 – 110, 2007.

36. J. Harvey, A. Krywonos, and C. Vernold. "Modified Beckmann-Kirchhoff scattering model for rough surfaces with large incident and scattering angles". *Optical Engineering*, 46(7):1 – 10, 2007.

37. M. Heald and J. Marion. *Classical Electromagnetic Radiation, 3rd Ed.* Dover Publications, Inc., Mineola, NY, 2017.

38. E. Hecht. *Optics, 5th Ed.* Pearson Education, Inc., New York, NY, 2017.

39. M. Hejduk. "Specular and Diffuse Components in Spherical Satellite Photometric Modeling". In *Advanced Maui Optical and Space Surveillance Technologies Conference*, 2011.

40. J.Coughlin. "Determining Satellite Rotation Rates for Unresolved Targets Using Temporal Variations in Spectral Signatures". *Advanced Maui Optical and Space Surveillance Technologies Conference*, 2014.

41. J. Kajiya. "The Rendering Equation". In *Proceedings of the 13th Annual Conference on Computer Graphics and Interactive Techniques*, volume 20, pages 143 – 150, 1986.

42. T. Kelecy and M. Skinner. "non-Imaging Characterization Assessment of Shedding Events from Derelict Satellites near Geosynchronous Orbit (GEO)". *Advanced Maui Optical and Space Surveillance Technologies Conference*, September 2016.

43. B. Klem and D. Swann. "space Object Radiometric Modeling for Hardbody Optical Signature Database Generation". *Advanced Maui Optical and Space Surveillance Technologies Conference*, September 2009.

44. A. Krywonos, J. Harvey, and N. Choi. "Linear Systems Formulation of Scattering Theory for Rough Surfaces with Arbitrary Incident and Scattering Angles". *J. Opt. Soc. Am. A*, 28(6):1121 – 1138, Jun 2011.

45. Paul LeVan, Jennifer Leute, and Martha Navarro. "Modeling of remotely sensed signatures of spacecraft". In Leonard M. Hanssen, editor, *Reflection, Scattering, and Diffraction from Surfaces VI*, volume 10750, pages 21 – 31. International Society for Optics and Photonics, SPIE, 2018.

46. J. Lowery. "Measuring Light Curve Uncertainty for Surrogate Geostationary Satellite Models". Master's thesis, Air Force Institute of Technology, 2017.

47. W. Matusik, H. Pfister, M. Brand, and L. McMillan. "A Data-Driven Reflectance Model". *ACM Trans. Graph.*, 22(3):759–769, Jul 2003.

48. J. Maxwell and J. Beard. "Bidirectional Reflectance Model Validation and Utilization". *Tech Report*, AFAL-TR-73-303, October 1973.

49. G. McCall and J. Darrah. "Space Situational Awareness: Difficult, Expensive – and Necessary". *Air and Space Power Journal*, November 2014.

50. F. Nicodemus. "Directional Reflectance and Emissivity of an Opaque Surface". *Applied Optics*, 4(7), 1965.

51. F. Nicodemus, J. Richmond, J. Hsia, I. Ginsberg, and T. Limperis. "Geometric Considerations and Nomenclature for Reflectance". *National Bureau of Standards Monograph 160, Department of Commerce*, October 1977.

52. G. Olsen, M. Ettenberg, and R. D'Aiello. "Vapor-Grown InGaP-GaAs Solar Cells". *Appl. Phys. Lett.*, 33(606):606 – 608, Oct 1978.

53. B. Phong. "Illumination for Computer Generated Pictures". *Communications of the ACM*, Vol 18 No 6, June 1975.

54. J. Posdamer. "The Geometry of Orbiting Earth Satellies (GOES)". *Air Force Research Laboratory Technical Report*, RADC-TR-79-357, January 1980.

55. M. Ribardiere, B. Bringier, D. Meneveaux, and L. Simonot. "STD: Student's t-Distribution of Slopes for Microfacet Based BSDFs". *The Eurographics Association: Computer Graphics Forum*, Vol 36 No 2, 2017.

56. J. Rifkin, K. A. Klicker, D. R. Bjork, D. R. Cheever, T. F. Schiff, J. C. Stover, F. M. Cady, D. J. Wilson, P. D. Chausse, and K. H. Kirchner. "Design Review Of A Complete Angle Scatter Instrument". In *Precision Instrument Design*, volume 1036, pages 116 – 124, 1989.

57. S. Rusinkiewicz. "A New Change of Variables for Efficient BRDF Representation". *Rendering Techniques*, 1998.

58. B. Sandford and L. Robertson. "Infrared Reflectance Properties of Aircraft Paint". *Proc. IRIS Targets, Backgrounds, and Discrimination*, 1985.

59. T. Schiff, J. Stover, D. Cheever, and D. Bjork. "Maximum And Minimum Limitations Imposed On Bsdf Measurements". In *Stray Light and Contamination in Optical Systems*, volume 0967, pages 50 – 57, 1989.

60. J. Schott. *Fundamentals of Polarimetric Remote Sensing*, volume 81. SPIE press, 2009.

61. M. Schubert, V. Gottschalch, C. Herzinger, H. Yao, P. Snyder, and J. Woollam. "Optical constants of Ga(x)In(1–x)P lattice matched to GaAs". *Journal of Applied Physics*, 77(7):3416 – 3419, Apr 1995.

62. ON Semiconductor®. KAI-08051: 3296 (H) x 2472 (V) Interline CCD Image Sensor. Website accessed in Jul 2021. Available at https://www.onsemi.com/pdf/datasheet/kai-08051-d.pdf.

63. H. Seo, H. Jin, Y. Song, Y. Lee, and Y. Oh. "The Photometric Brightness Variation of Geostationary Orbit Satellites". *Journal of Astronomy and Space Sciences*, 2013.

64. T. Small, S. Butler, and M. Marciniak. "Solar Cell BRDF Measurement and Modeling with Out-of-Plane Data". *Submitted to Optics Express on 12 Aug 2021.*

65. T. Small, S. Butler, and M. Marciniak. "Uncertainty Analysis for CCD-Augmented CASI® BRDF Measurement System". *Submitted to Optical Engineering on 7 Jun 2021.*

66. T. Small, S. Butler, and M. Marciniak. "Augmenting CASI® BRDF Measurement Device to Measure Out-of-Plane Scatter with CCD Pixel Array". In *Reflection, Scattering, and Diffraction from Surfaces VII*, volume 11485, pages 24 – 37. SPIE, 2020.

67. T. Small, S. Butler, and M. Marciniak. "Scatter Coordinate Mapping and Out-of-Plane BRDF Measurements for Specular Materials using an Augmented CASI® Measurement System". In *Algorithms, Technologies, and Applications for Multispectral and Hyperspectral Imaging XXVII*, volume 11727, pages 175 – 191. SPIE, 2021.

68. The Scatter Works, Inc. The CASI Scatterometer. Website accessed in Jul 2021. Available at https://thescatterworks.com/casi/.

69. Thorlabs®. Digital Scientific Camera 8051M-USB. Website accessed in Jul 2021. Available at https://www.thorlabs.com/drawings/1dfe78119eeda5-479F8761-DB7E-4B44-2B92E3AF4C68E89A/8051M-USB-AutoCADPDF.pdf.

70. K. Torrance and E. Sparrow. "Theory for Off-Specular Reflection from Roughened Surfaces". *Journal of the Optical Society of America*, Vol 75 No 9, Septmeber 1967.

71. T. Trowbridge and K. Reitz. "Average Irregularity Representation of a Rough Surface for Ray Reflection". *Journal of the Optical Society of America*, Vol 65 No 5, May 1975.

72. J Vap, S Nauyoks, and M Marciniak. "Optimization of a dual-rotating-retarder polarimeter as applied to a tunable infrared Mueller-matrix scatterometer". *Measurement Science and Technology*, 24(5):055901, Mar 2013.

73. J. Verdeyen. *Laser Electronics*. Prentice Hall, Upper Saddle River, NJ, 1995.

74. H. Wang, W. Zhang, and A. Dong. "Modeling and Validation of Photometric Characteristics of Space Targets Oriented to Space-Based Observation". *Applied Optics*, Vol 51 No 32, November 2012.

75. G. Ward. "Measuring and Modeling Anisotropic Reflection. *Proceedings of the 19th annual conference on Computer graphics and interactive techniques*, July 1992.

76. D. Wellems, S. Ortega, D. Bowers, J. Boger, and M. Fetrow. "Long Wave Infrared Polarimetric Model: Theory, Measurements, and Parameters". *Journal of Optics A: Pure and Applied Optics*, 8:914–925, 2006.

REPORT DOCUMENTATION PAGE

Form Approved
OMB No. 0704–0188

1. REPORT DATE *(DD–MM–YYYY)*	2. REPORT TYPE	3. DATES COVERED *(From — To)*
16–09–2021	Doctoral Dissertation	Sept 2018 — Sept 2021

4. TITLE AND SUBTITLE

Improved Out-of-Plane Measurement and Modeling for Bidirectional Reflectance Distribution Functions

5a. CONTRACT NUMBER

F4FGA09014J002

5b. GRANT NUMBER

5c. PROGRAM ELEMENT NUMBER

6. AUTHOR(S)

Todd V. Small, Maj, USAF

5d. PROJECT NUMBER

20P503

5e. TASK NUMBER

5f. WORK UNIT NUMBER

7. PERFORMING ORGANIZATION NAME(S) AND ADDRESS(ES)

Air Force Institute of Technology
Graduate School of Engineering and Management (AFIT/EN)
2950 Hobson Way
WPAFB OH 45433-7765

8. PERFORMING ORGANIZATION REPORT NUMBER

AFIT-ENP-DS-21-S-035

9. SPONSORING / MONITORING AGENCY NAME(S) AND ADDRESS(ES)

Air Force Office of Scientific Research
Attn: Dr. Michael Yakes
875 North Randolph Street
Arlington, VA 22203
COMM 703-696-9586 Email: technicalreports@us.af.mil

10. SPONSOR/MONITOR'S ACRONYM(S)

AFOSR

11. SPONSOR/MONITOR'S REPORT NUMBER(S)

12. DISTRIBUTION / AVAILABILITY STATEMENT

DISTRIBUTION STATEMENT A:
APPROVED FOR PUBLIC RELEASE; DISTRIBUTION UNLIMITED.

13. SUPPLEMENTARY NOTES

14. ABSTRACT

Historically, the vast majority of bi-directional reflectance distribution function (BRDF) measurement and modeling research has focused on reflection within the plane-of-incidence (in-plane) and simplified isotropic cases. Remote sensing applications, such as satellite light curve analysis, still struggle with disagreements between observations and simulations, but do not typically model reflection outside the plane-of-incidence (out-of-plane). First, a novel system is designed and constructed to successfully measure out-of-plane material BRDFs near the specular peak with high angular resolution. The system is then used to measure several materials, including a commercially available satellite solar cell. The measurements identify previously unmodeled out-of-plane components, including a significant diffraction pattern. Finally, a novel closed-form BRDF model is created which accurately replicates the solar cell's out-of-plane reflection behavior – including the diffraction pattern – using traditional BRDF inputs. Ultimately, it is expected that this and other out-of-plane BRDF models may improve the accuracy of light curve analysis and other remote sensing applications.

15. SUBJECT TERMS

Optical Scatter, BRDF, Remote Sensing, Scene Generation, Space Domain Awareness

16. SECURITY CLASSIFICATION OF:			17. LIMITATION OF ABSTRACT	18. NUMBER OF PAGES	19a. NAME OF RESPONSIBLE PERSON
a. REPORT	b. ABSTRACT	c. THIS PAGE			Lt Col Samuel D. Butler, AFIT/ENP
U	U	U	UU	186	19b. TELEPHONE NUMBER *(include area code)* (937) 255-3636; samuel.butler@afit.edu